



Multifunctional roles of MoS₂ in persulfate-based advanced oxidation processes for eliminating aqueous organic pollutants: A review

Chunyang Nie ^a, Jinlong Wang ^b, Bihai Cai ^b, Bo Lai ^c, Shaobin Wang ^{d,*}, Zhimin Ao ^{e,*}

^a School of Resources & Environment, Key Laboratory of Poyang Lake Environment and Resource Utilization, Ministry of Education, Nanchang University, Nanchang 330031, China

^b Guangzhou Key Laboratory of Environmental Catalysis and Pollution Control, Guangdong Key Laboratory of Environmental Catalysis and Health Risk Control, Institute of Environmental Health and Pollution Control, School of Environmental Science and Engineering, Guangdong University of Technology, Guangzhou 51006, China

^c State Key Laboratory of Hydraulics and Mountain River Engineering, College of Architecture and Environment, Sichuan University, Chengdu 610065, China

^d School of Chemical Engineering, the University of Adelaide, Adelaide, SA 5005, Australia

^e Advanced Interdisciplinary Institute of Environment and Ecology, Beijing Normal University, Zhuhai 519087, China



ARTICLE INFO

Keywords:

Molybdenum disulfide
Persulfate activation
Organic pollutants
Multifunctionalities
Energy recovery

ABSTRACT

Molybdenum disulfide (MoS₂) has emerged as a versatile activator in persulfate-based advanced oxidation processes (PS-AOPs). As a polymorphic layered material, MoS₂ shows variable physicochemical properties including electrical, optical, catalytic and piezoelectric properties depending on the crystal structure. Accordingly, MoS₂ can serve as a cocatalyst/catalyst to directly activate persulfate and the activation efficiency can be further improved through converting external stimulus (e.g., light and mechanical force) into chemical/thermal energy. This review presents the recent advances of MoS₂-based materials as effective catalysts in various PS-AOPs. We systematically compare the properties of three MoS₂ polytypes (1 T, 2 H and 3 R) and their applications in PS-AOPs. Meanwhile, modifications on MoS₂ and the persulfate activation processes with different functions of MoS₂-based materials are discussed. Moreover, critical issues and research directions in MoS₂ future applications in PS-AOPs are addressed, with prospects towards implementation of self-powered water treatment systems with additional energy recovery.

1. Introduction

Water is the foundation of life, societies and economies. However, the rapid industrialization, urbanization and growth of population in the modern society lead to severe water abuse and water contamination, causing worldwide water shortage crisis. Moreover, the climate change also exacerbates the water stress [1]. At present, around a quarter of the world's population encounter water scarcity and the number will increase in the next few decades [1]. Therefore, it is urgent to improve the water reuse and efficiency to ensure water sustainability. Wastewater can be considered an alternative water resource if proper treatment technologies could be developed. One of the challenges for safe wastewater reuse arises from the presence of organic matters. Particularly, emerging pollutants (also referred as organic micropollutants) including personal care products, pharmaceuticals, steroid hormones with trace levels (< 1 mg L⁻¹) are commonly detected in wastewater, which presents a new global water quality issue with potentially negative impacts

on human health and the ecosystems [2].

Advanced oxidation processes (AOPs) have been widely acknowledged as efficient physicochemical methods for abating a wide range of organic micropollutants because the AOPs exploit highly reactive oxygen species (ROS) to transform the toxic organic matter into nontoxic or low toxic small molecular compounds and even mineralize them into dioxide and water [3,4]. Besides, the ROS can also attack pathogen cells, leading to the pathogen inactivation. Hence, AOPs are also popular approaches for water disinfection [5,6]. Traditional AOPs were exclusively referred to the processes generating hydroxyl radical ($\bullet\text{OH}$) with redox potential of 1.8–2.7 V_{NHE}, among which Fenton processes have the longest history [7]. During the past decade, the solid-state persulfate has been recognized as an important oxidant in AOPs since it is a precursor for generating sulfate radical ($\text{SO}_4^{\bullet-}$). Compared to $\bullet\text{OH}$, $\text{SO}_4^{\bullet-}$ has a comparative redox potential (2.5–3.1 V_{NHE}) but longer life time (30–40 μs , $\bullet\text{OH}$: < 1 μs) and stronger adaptability under a wider pH range [7]. Moreover, nonradical reactive species have also been recently

* Corresponding authors.

E-mail addresses: shaobin.wang@adelaide.edu.au (S. Wang), zhimin.ao@bnu.edu.cn (Z. Ao).

discovered in persulfate-based AOPs (PS-AOPs) systems [8,9]. In this respect, the current recognition as AOPs has also been given to the processes that produce SO_4^{\cdot} and/or nonradical species.

In PS-AOPs, external stimulation is required to activate persulfate for generating ROS. A diversity of physical and chemical agents is found to be capable of effectively activating persulfate involving heat, electricity, light, ultrasonic wave, metal-based materials (homogeneous metal ions and heterogeneous metals), nonmetal materials (carbon, boron, etc.), base, and organic substrates (phenols, quinones), etc. [10–24]. Among them, MoS_2 as a prototypical transition-metal dichalcogenide (TMDC) with layered structure has gained tremendous attention in the field of PS-AOPs due to its unique physicochemical properties [25–27].

MoS_2 has been well-known during the last few decades for its uses in lubricants, batteries, photocatalysis and photovoltaic devices [28–30]. Stimulated by the discovery of graphene, 2D materials have been a hot research field because the quantum confinement of electrons induces distinguished properties from their bulk phases [31]. In recent years, 2D MoS_2 has intrigued the scientific community owing to its facile synthesis and fascinating properties that totally differ from graphene [32,33]. Particularly, the rich polytypism feature of TMDC materials endows MoS_2 variable properties from semiconducting to metallic conducting, and from piezoelectric to nonpiezoelectric behavior, etc. [34–36]. For instance, the semiconducting MoS_2 nanosheets possess a bandgap comparable to traditional GaAs or Si, which renders them as promising candidates for electronic switches, photocatalyst, photovoltaic devices and near-infrared (NIR) photo-thermal agents [28,32,37]. Additionally, the polyvalent nature of Mo (e.g., Mo^{2+} , Mo^{4+} , Mo^{6+}) and unsaturated S sites in MoS_2 endow it higher catalytic activity than graphene because of the valence change and electron transfer [25,38]. The surface S atoms in 2D MoS_2 are Lewis base and show strong affinity to heavy metal ions, which makes it an excellent adsorbent or membrane material for removing heavy metal ions [34]. Moreover, some of the 2D MoS_2 polytypes exhibit comparable or even better piezoelectric property with regard to the traditional piezoceramics [35,36,39]. As a result, 2D MoS_2 shows plentiful applications in water splitting, solar cells, batteries, water treatment, nanogenerators, sensors, and biomedicine, etc. [30,33,34,40,41].

The wide applications of MoS_2 in the PS-AOPs are primarily triggered by Xing's pioneering work in 2018, which reported that the polyvalent Mo in bulk MoS_2 could rapidly accelerate the $\text{Fe}^{3+}/\text{Fe}^{2+}$ redox cycle and thus markedly enhanced the degradation performance of classic Fenton agent ($\text{Fe}^{2+}/\text{H}_2\text{O}_2$) [42]. Following this work, bulk MoS_2 was commonly utilized as the cocatalyst to boost Co^{2+} , Fe^{2+} and Fe^{3+} -based persulfate systems for degrading various organic contaminants [43–46]. When bulk MoS_2 was introduced into the homogeneous persulfate systems, the material itself also shows catalytic activity towards persulfate activation for degrading organic micropollutants [47–49]. Hence, researchers paid attention to the applications of bulk MoS_2 and nanostructured MoS_2 as catalysts in PS-AOPs and investigated the performances of different MoS_2 polytypes [48,50,51]. Furthermore, a lot of efforts on the modifications of MoS_2 have been made to improve its catalytic performance [52–55]. On the other hand, the peculiar optical and piezoelectric features of 2D MoS_2 enable it to convert light energy or mechanical force into photo/piezo-induced electrons and holes or heat energy for persulfate activation [56–58]. From this perspective, the multiple functionalities of MoS_2 offer novel approaches for persulfate activation. Overall, MoS_2 has become a new favorite in the PS-AOPs field arising from its outstanding performance, abundant elemental constituents, low-cost, good biocompatibility and easy availability of mono/few layered 2D materials [30,59–61].

Up to now, there are a considerable amount of reviews summarizing the synthetic methods of 2D MoS_2 nanomaterials and their applications in hydrogen production, energy storage, self-powered systems, sensors and photocatalytic degradation of organic pollutants in the literature [27,38,62–65]. Nevertheless, reviews on the applications of multiphasic MoS_2 (bulk and 2D materials) in PS-AOPs are limited, while a growing

number of relevant research articles have been witnessed in recent years. The current review therefore aims to describe the structures and physicochemical properties of various MoS_2 polytypes and overview the diverse applications of MoS_2 in the PS-AOPs.

First, the structure characteristics of two common MoS_2 polytypes (1 T and 2 H) and another metastable polytype (3 R) are introduced. Then their corresponding physicochemical properties (electronic, optical, piezoelectric, and chemical catalytic properties) are discussed with an emphasis on the structure-property relationship. Noting that, though 3R- MoS_2 has not been applied in PS-AOPs so far, its superior physicochemical properties to 2 H phase endow a great promise in PS-AOPs. Following that, the applications of polymorphic MoS_2 and MoS_2 -based materials as cocatalysts, chemical catalysts, photocatalysts, photo-thermal agents and piezocatalysts in PS-AOPs are summarized and the different activation processes are compared and discussed. Finally, an outlook on major challenges and opportunities facing MoS_2 materials will be proposed.

2. Structure, synthesis and properties of MoS_2 polytypes

2.1. Crystalline structure

The typical structure of a monolayer TMDC is composed of a transition metal atom sheet sandwiched between two sheets of closely packed chalcogenide atoms, in which the metal atoms and chalcogenide atoms are covalently bonded. Because of the specifically atomic assembled manner, TMDC can generally crystallize in several 2D structures [31]. For MoS_2 , it mainly exists in three polytypes, including 1 T (octahedral), 2 H (hexagonal) and 3 R (rhombohedral) [66]. 1 T- MoS_2 is a trigonal antiprismatic structure wherein one Mo atom is coordinated with six S atoms to form an octahedral geometry [67]. Both 2 H and 3 R phases have a trigonal prismatic Mo coordination, while the stacking mode and number of ' MoS_2 ' layers in their unit cells are different, i.e., two layers in the unit cell of 2 H- MoS_2 with an AB-AB stacking order and three layers in the unit cell of 3R- MoS_2 with an ABC-ABC stacking order (A, B, C layers are in the same direction) [66]. Their atomic structures are depicted in Fig. 1. The MoS_2 layers are linked via weak van der Waals (vdW) force with an interlayer distance of 0.62 nm and a free spacing of 0.30 nm [34].

X-ray diffraction (XRD) is a powerful tool to characterize the crystal structures of materials. The XRD pattern of the three MoS_2 polytypes are displayed in Fig. 2a-b. It should be noted that the XRD pattern of 1 T- MoS_2 in Fig. 2a is not collected in the Inorganic Crystal Structure Database (ICSD) because a strict structural refinement is lacking [68]. As seen, the XRD pattern of 3R- MoS_2 quite resembles to that of 2 H phase, except that the regions at $20 \sim 40^\circ$ and $\sim 50^\circ$ show visible difference (Fig. 2b). This usually leads to the mischaracterization of MoS_2 as the 3R- MoS_2 polytype when interpreting the XRD data of samples prepared by hydrothermal as well as other synthetic methods [66]. Because of the different crystal structures of the three polytypes, they possess distinct physicochemical properties, which will be discussed in the following sections.

2.2. Synthesis

Among the three polytypes, 2 H- MoS_2 is the most thermodynamically stable phase. Hence, the natural molybdenite and commercial bulk MoS_2 are primarily composed of 2 H phase. Noting that a low content of 1 T and 3 R phases probably coexist in commercial bulk MoS_2 , while their relative proportions from different sources vary largely [69]. Meanwhile, 2 H- MoS_2 nanostructures can be facilely obtained by top-down (e.g., Scotch tape, micromechanical exfoliation with ball-milling or sonication, chemical exfoliation) and bottom-up (e.g., hydrothermal, solvothermal, chemical vapor deposition (CVD), chemical vapor transport (CVT)) methods [30,32]. Among these methods, hydrothermal and solvothermal methods are popularly employed to

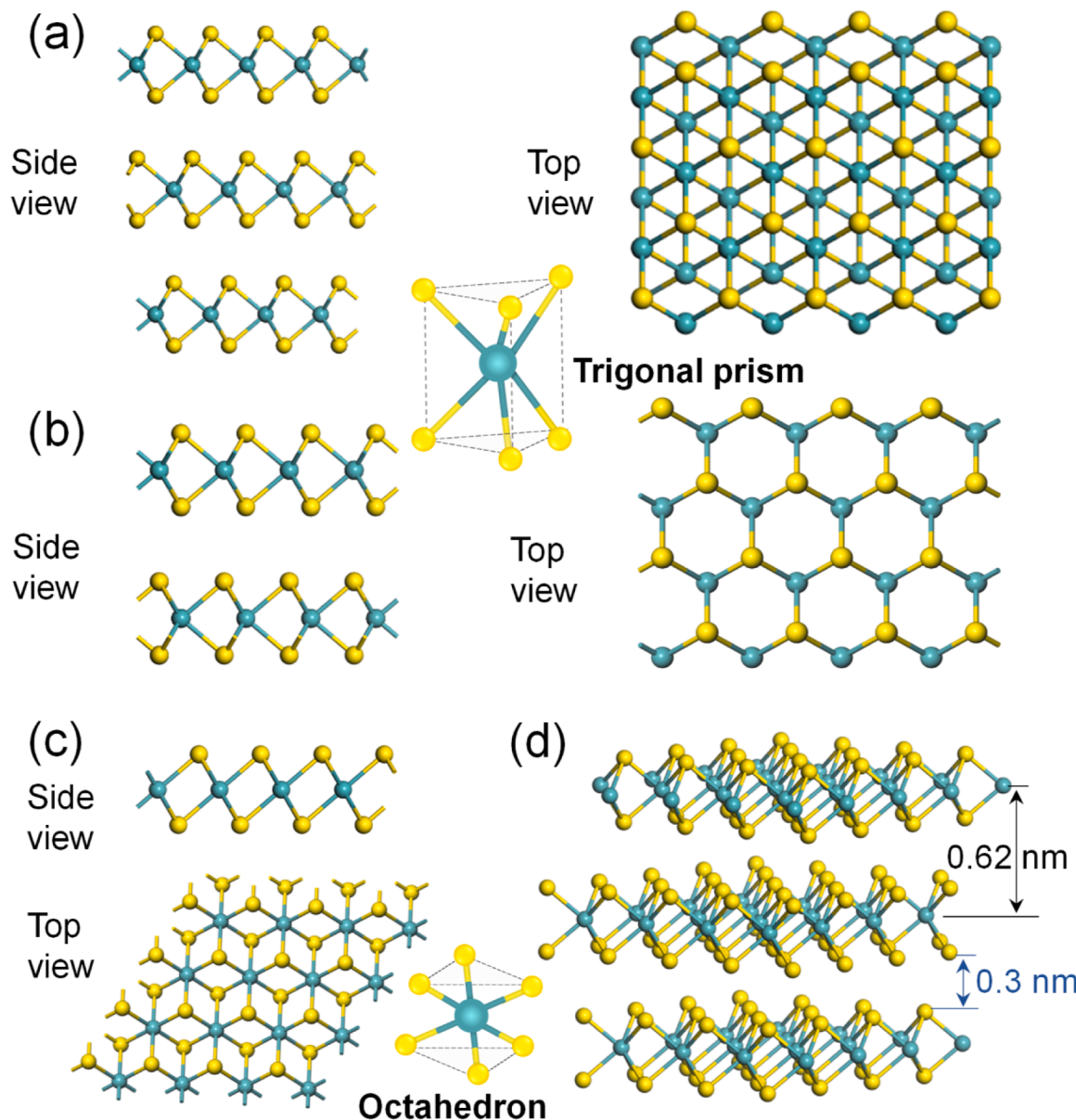


Fig. 1. Side view and top view of crystal structure of (a) 3R-MoS₂ and (b) 2 H-MoS₂; the inset between (a) and (b) shows the trigonal prismatic Mo-S coordination shape in the two phases. (c) Side view and top view of crystal structure, and the octahedral Mo-S coordination shape of 1 T-MoS₂. (d) 3D illustration of MoS₂ structure (taking 3 R phase as the example). Cyan and yellow balls are Mo and S atoms, respectively.

synthesize 2 H-MoS₂ nanostructures and 2 H-MoS₂-based nanocomposites due to the merits of high yield and easy operation. However, a closed-shell inorganic fullerene structure (also called as flower-like structure which is composed of wrinkled nanosheets) is usually formed in the hydrothermal and solvothermal synthesis of 2 H-MoS₂ nanomaterials. This is because the undercoordinated and irregular edges of MoS₂ are not favorable to the formation of 2 H-MoS₂ nanosheet from the view-point of thermodynamics [38].

3R-MoS₂ is the second stable phase and has been found in the natural deposits as well. Large-scale synthesis of bulk 3R-MoS₂ could be achieved using the salt flux and CVT methods [66,70]. However, approaches for fabricating 3R-MoS₂ nanostructures are relatively limited with regard to 2 H-MoS₂ nanostructures, which makes 3R-MoS₂ being overlooked in the past. Scotch tape and CVD methods are also available for obtaining monolayer and few-layered 3R-MoS₂, but the yield is rather low [66]. Sub-micrometer 3R-MoS₂ is possible to be attained by a hydrothermal method, while the resultant product is normally mixed-phase MoS₂ and the relative proportions of different phases (1 T,

2 H and 3 R) could be tuned by controlling the precursors [66].

In contrast, 1 T-MoS₂ is metastable and does not naturally exist, but it can be experimentally prepared from 2 H-MoS₂ via ion-intercalation [64,71]. Typically, monolayer and/or few-layer 1 T-MoS₂ nanosheets are produced from ion-intercalation method. However, the synthetic procedures of ion-intercalation method are quite complicated and dangerous, which is not conducive to the mass production of 1 T-MoS₂ nanosheets. Alternatively, polymorphic 1 T/2 H MoS₂ nanostructures can be obtained by the hydrothermal/solvothermal method and the content of 1 T phase can be improved by selecting proper precursors and synthesis temperature [72,73].

In general, the three phases are interconvertible under specific conditions like electric doping, annealing and controlling strain [59]. As a result, two phase- or three phase-constructed 2D MoS₂ heterojunctions can be attained via delicate experimental manipulation and they manifest distinct properties and performances from the single phase MoS₂ [30,74]. More information on the available synthetic methods for fabricating 1 T and 2 H-MoS₂ nanomaterials could be referred in many

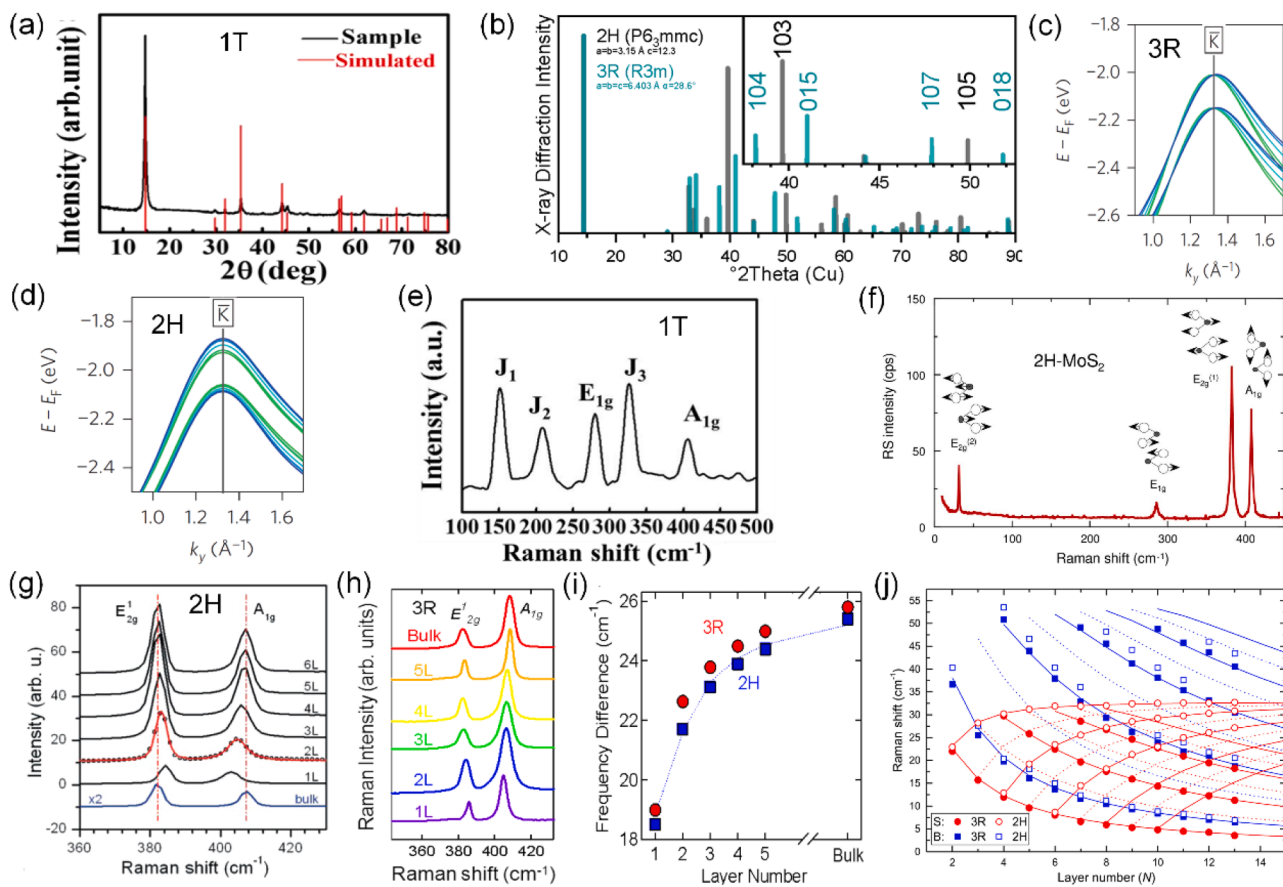


Fig. 2. (a) XRD pattern of 1 T-MoS₂. (b) XRD patterns of 2 H (ICSD, 24000) and 3R-MoS₂ (ISCD, 38401). Inset displays magnified region from 37.5° to 52.5° 2θ. Calculations on the top of the valence band at the \bar{K} point for (c) 3R-MoS₂ and (d) 2 H-MoS₂. (e) Raman spectrum of 1 T-MoS₂. (f) Raman spectrum of 2 H-MoS₂. (g) Raman spectra of bulk and few-layer 2 H-MoS₂ films. (h) and (i) are Raman spectra of 3R-MoS₂ thin films around 400 cm⁻¹ and frequency difference of two modes E_{2g} and A_{1g} as the function of layer number for 3 R and 2 H-MoS₂ crystals. (j) Frequencies of shear modes (S; red) and breathing modes (B; blue) as the function of layer number of 2 H and 3R-MoS₂.

(a) Reproduced with permission from ref. [68]. Copyright 2017, Wiley-VCH Verlag GmbH & Co. KGaA, Weinheim. (b) Reproduced with permission from ref. [66]. Copyright 2021, American Chemical Society (d) Reproduced with permission from ref. [70]. Copyright 2014, Nature Publishing Group. (e) Reproduced with permission from ref. [68]. Copyright 2017, Wiley-VCH Verlag GmbH & Co. KGaA, Weinheim. (f) Reproduced with permission from ref. [79]. Copyright 2008, Chemistry Central Ltd. (g) Reproduced with permission from ref. [80]. Copyright 2010, American Chemical Society. (i) Reproduced with permission from ref. [70]. Copyright 2014, Nature Publishing Group. (j) Reproduced with permission from ref [82]. Copyright 2019, IOP Publishing Ltd.

previous reviews [25,28,30,63,66].

2.3. Electronic property

MoS₂ manifests a range of appealing electronic and optical properties depending on the polytypes and number of layers, which makes it a promising candidate in many applications [33]. The filling of d-bands in a Mo atom near the Fermi level determines the properties of MoS₂ materials, while the filling configuration is directly related to the crystal structure [30]. For 2 H-MoS₂ with a complete filling of d orbitals, it behaves as a semiconductor and the decrease of layer number gives rise to an increase of the bandgap from 0.86 – 1.29 eV for bulk sample to ~1.9 eV for monolayer counterpart; the bandgap nature changes from indirect (bulk) to direct (monolayer) [32,75]. 3R-MoS₂ displays quite analogous overall band structure to that of 2 H-MoS₂ owing to their similar crystalline structures and d-bands filling configuration, but the detailed band structures of two phases are distinct [66]. The energy splitting of the top of valence band of 2 H-MoS₂ is slightly higher than that of 3R-MoS₂ (Fig. 2c and d) and the K exciton electron-hole pair can follow both intralayer and interlayer relaxation pathways for 2 H-MoS₂, while only intralayer relaxation pathway is allowed in 3R-MoS₂ due to its broken inversion symmetry [70]. Additionally, the presence of sulfur vacancies or defects in 2 H/3R-MoS₂ has an influence on the bandgap of

the material, which provides a facile approach to tune the bandgap of MoS₂ via defect engineering [38,66].

As for 1 T-MoS₂, the partial filling of d orbitals endows it metallic behavior [30]. The good electrical conductivity of 1 T-MoS₂ (10–100 S cm⁻¹) that is around 105 times higher than that of 2 H-MoS₂ is favorable to the charge transfer, allowing for uses in electrodes of batteries [76].

Raman spectroscopy is an essential instrument for studying the electronic structures and layer number of 2D materials [77]. Because of the distinct crystal structures, 1 T-MoS₂ and 2 H/3R-MoS₂ exhibit different Raman scattering behavior (Fig. 2e-j). According to both theoretical calculations and experimental results, single crystal 1 T-MoS₂ exhibits two strong Raman active modes located at 280 (E_{1g}) and 405 cm⁻¹ (A_{1g}), corresponding to the in-plane interlayer vibration mode and out-of-plane interlayer vibration mode, respectively (Fig. 2e) [68,78]. In addition, another three peaks located at ~150 (J₁), ~212 (J₂) and ~324 cm⁻¹ (J₃) are also observed in the Raman spectrum of single crystal 1 T-MoS₂, which is explained by the presence of superlattice in the material [68,78]. On the contrary, monolayer 2 H/3R-MoS₂ exhibits four first-order Raman active modes including E_{2g} (32 cm⁻¹), E_{1g}, E_{2g} (383 cm⁻¹) as well as A_{1g} (Fig. 2f) [66,79]. The low-frequency E_{2g}² mode is attributed to the interlayer interaction with

rigid layer motion and the E_{2g}^1 mode is related to the in-plane vibration [32,66]. Particularly, the frequency, line width and intensity of E_{2g}^1 and A_{1g} modes are reported to be sensitive to the thickness of 2 H/3R-MoS₂ crystals, but they exhibit distinct dependences on the layer number (Fig. 2g-i) [70,80]. For instance, the increase of layer number results in a remarkable blue-shift of the A_{1g} peak attributing to the vdW interlayer interactions but a small red-shift for E_{2g}^1 peak which is related to the long-range Coulombic interlayer interactions [70,80]. As a result, the gap between the frequencies of the two modes ($\Delta\omega$) is considered as an important index for determining the layer number of as-prepared MoS₂ samples. Moreover, the discrimination between 2 H-MoS₂ and 3R-MoS₂ can be realized with the help of advanced Raman spectroscopy. Xia et al. demonstrated that the 'a' peak located at $\sim 395\text{ cm}^{-1}$ in the surface-enhanced Raman spectra of MoS₂ bilayers was the primary discrepancy between the two polytypes [81]. Baren and co-workers reported that the appreciable differences in shear mode and breathing mode of the polarization-dependent ultralow-frequency Raman spectra are useful to distinguish 2 H-MoS₂ from 3R-MoS₂ (Fig. 2j) [82].

2.4. Optical property

Due to the different electronic structures, the three MoS₂ polytypes also possess distinct optical properties. 1 T-MoS₂ can harvest the whole solar spectrum (from ultraviolet (UV) to IR region), while its prominent absorption peaks are absent in the absorption spectrum owing to the

metallic nature with zero bandgap (Fig. 3a) [83]. In particular, the good NIR absorbance of 1 T-MoS₂ renders it an excellent photothermal agent. Chou et al. reported that the 1 T-MoS₂ nanosheets exfoliated from bulk materials via lithium-intercalation manifest comparable absorbance in NIR to reduced graphene oxide, which is much higher than those of graphene oxide and gold nanorods [37].

Bulk 2 H-MoS₂ can also harvest the whole solar spectrum due to the narrow bandgap, but its recombination rate of charge carriers is also high, which is undesirable for the photocatalytic applications [28]. Nevertheless, the suitable bandgap of nanostructured 2 H-MoS₂ endows good visible light absorption capability and charge carrier separation efficiency (Fig. 3b), which makes it as a promising visible light-responsive photocatalyst/cocatalyst for various reactions [27,28, 84,85]. Nanostructured 2 H-MoS₂ can also absorb NIR light but their NIR absorbance is reported to be much weaker than 1 T phase, resulting from the semiconducting nature [83]. Bulk 3R-MoS₂ shows similar light absorption behavior to that of bulk 2 H phase as a result of their similar electronic structures. For nanostructured 3R-MoS₂, it is predicted to possess favorable visible light absorption capability and charge carrier separation efficiency based on its theoretical band structures, while relevant experimental proofs are lacking due to the challenge in synthesis of nanostructured 3R-MoS₂.

Additionally, 2 H and 3 R polytypes show distinct photoluminescence resulting from the difference in their detailed band structures. For 2 H-MoS₂, the nanosheets show strong photoluminescence, which is absent in bulk counterpart, originating from the

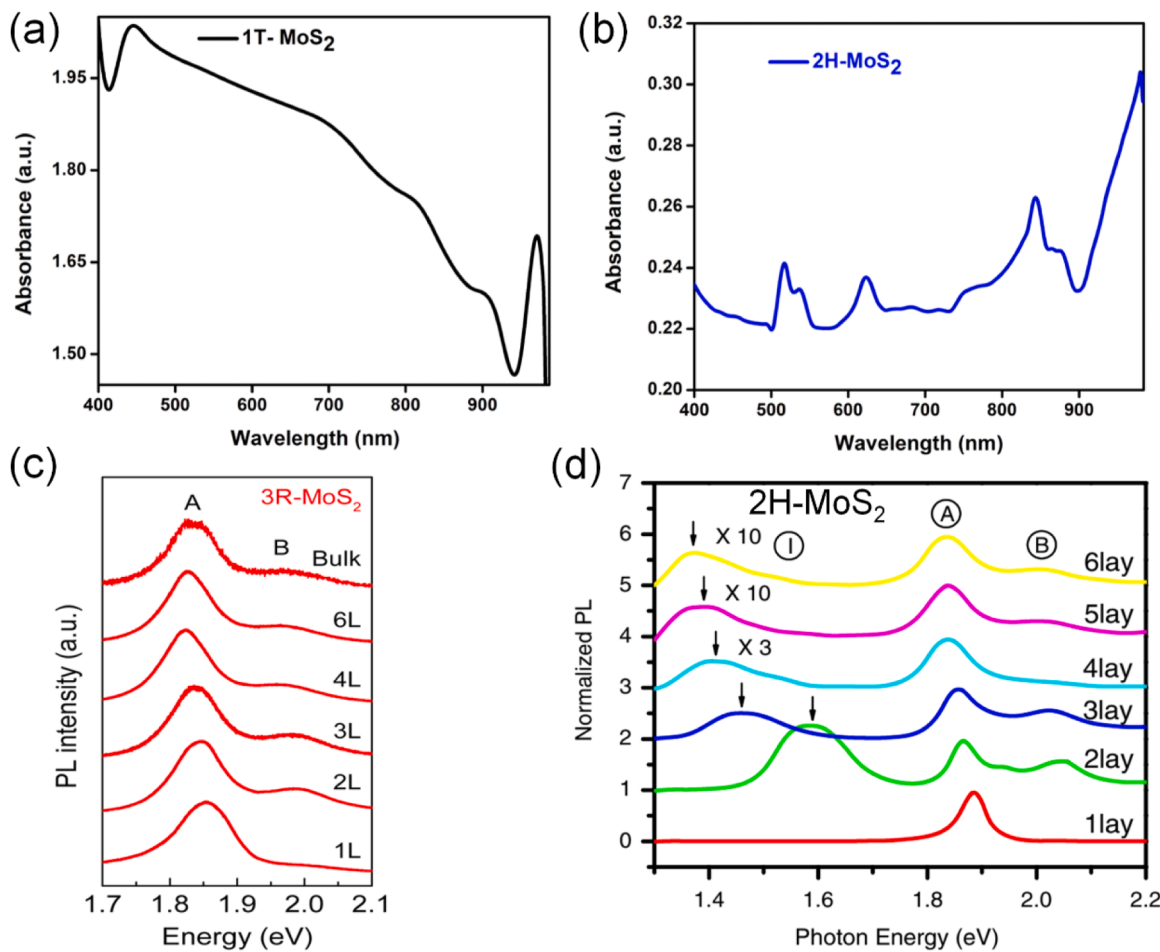


Fig. 3. UV-visible absorption spectra of (a) 1 T nanosheets and (b) 2 H-MoS₂ nanosheets. (c) Normalized PL spectra of 3R-MoS₂ with different number of layers. (d) Normalized PL spectra of 2 H-MoS₂ with different number of layers.

(a) and (b) Reproduced with the permission from ref. [83]. Copyright 2022, American Chemical Society. (c) Reproduced with the permission from ref. [87]. Copyright 2017, American Chemical Society. (d) Reproduced with permission from ref. [88]. Copyright 2010, American Physical Society.

quantum confinement effects [86]. However, 3R-MoS₂ exhibits strong photoluminescence for both nanostructured and bulk materials. Two photoluminescent exciton peaks (A and B) between 1.8 and 2.0 eV can be observed in 2 H/3 R MoS₂, assignable to *d-d* transition excitons split by spin-orbit coupling (Fig. 3c and d) [66,87,88]. Through employing circularly polarized photoluminescence spectroscopy, Suzuki et al. discovered that the intensity difference of photoluminescence spectra declines remarkably with the increase of layer number for 2 H-MoS₂ but almost remains unchanged for 3R-MoS₂ [70].

2.5. Piezoelectric property

For piezoelectric materials, an external mechanical stress can induce the separation of charge carriers and thus formation of a piezopotential, which alters the arrangement of both inside and outside free charges of the material (called as piezoelectric effect) [35]. In some sense, piezoelectricity serves as a bridge between the mechanical domain and electrochemical domain. Piezoelectric materials are essentially semiconductors with non-centrosymmetric structures, such as lead zirconate titanate, zinc oxide, etc. [89]. Intriguingly, a few materials with centrosymmetric structures are not piezoelectric in their bulk form but attain piezoelectricity in the 2D counterparts due to the disappearance of inversion symmetry [90]. One of such examples is TMDC, whose piezoelectric characteristics have been extensively investigated for potential applications in nanogenerators, sensors, piezotronics and photoelectronics [90].

In the case of MoS₂, the extraordinary piezoelectric property of a monolayer has been both theoretically predicted and experimentally proofed (Fig. 4a-e) [35,91,92]. Since MoS₂ layers are preferentially stacked in the common 2 H phase, it was discovered that piezoelectricity only preserves in multilayer structures with an odd number of layers because the even-layered structures are centrosymmetric (Fig. 4e) [92]. Nevertheless, the piezoelectric coefficient of multi-layered 2 H-MoS₂ declines approximately as 1/N with the number (N) of odd layers, which adversely affects its practical application [35].

Opposing to 2 H polytype, the 3R-MoS₂ structure has broken

inversion symmetry for any number of layers and thus shows a better piezoelectric response [66,70]. According to the computational works by Konabe et al. [93] and Tan et al. [36], both the bulk and multilayer 3R-MoS₂ samples possess high piezoelectric coefficients. Especially, due to the complicated surface effects and electronic interactions in 3R-MoS₂, a volcano relationship between the layer number and piezoelectric constant (e_{11}) of 3R-MoS₂ was discovered and the e_{11} reached a peak value of 0.457 C/m² at five layers (Fig. 4f) [36]. This suggested that 3R-MoS₂ is a more promising candidate as piezoelectric material than 2 H-MoS₂.

The metallic 1 T-MoS₂ of tetragonal symmetry is apparently lack of piezoelectricity. Despite of this fact, integration of 1 T-MoS₂ with 2 H/3R-MoS₂ to form a heterojunction can effectively improve the piezoelectricity in MoS₂ because the piezo-potential established at the metal-semiconductor interfacial region is able to regulate the local-contact characteristics and thus promote the charge separation across the interface [74]. In this regard, synthesizing polymorphic MoS₂ nanostructures via phase engineering is a potential strategy to enhance the piezoelectric response of MoS₂. Defect engineering such as creating S vacancies, heteroatom doping with metal and oxygen is another popular approach to enhance the piezoelectric response of MoS₂ due to the increased concentration of free charges and asymmetry of crystal structure [94,95].

2.6. Catalytic active sites of MoS₂

In light of the different crystalline structures and physicochemical properties of various MoS₂ polytypes, they manifest disparate catalytic activity. For semiconducting 2 H-MoS₂, the basal planes are catalytically inert and the active sites primarily lie in the edges of MoS₂ layers owing to the presence of undercoordinated atoms and dangling bonds [38]. For example, the Mo edges are demonstrated to show reactivity towards catalyzing hydrogen evolution reaction (HER) while the S edges are inactive to the HER [38]. Therefore, the dimension reduction is an effective strategy to increase the exposure of active edges in MoS₂, which becomes the impetus for researchers to fabricate various MoS₂

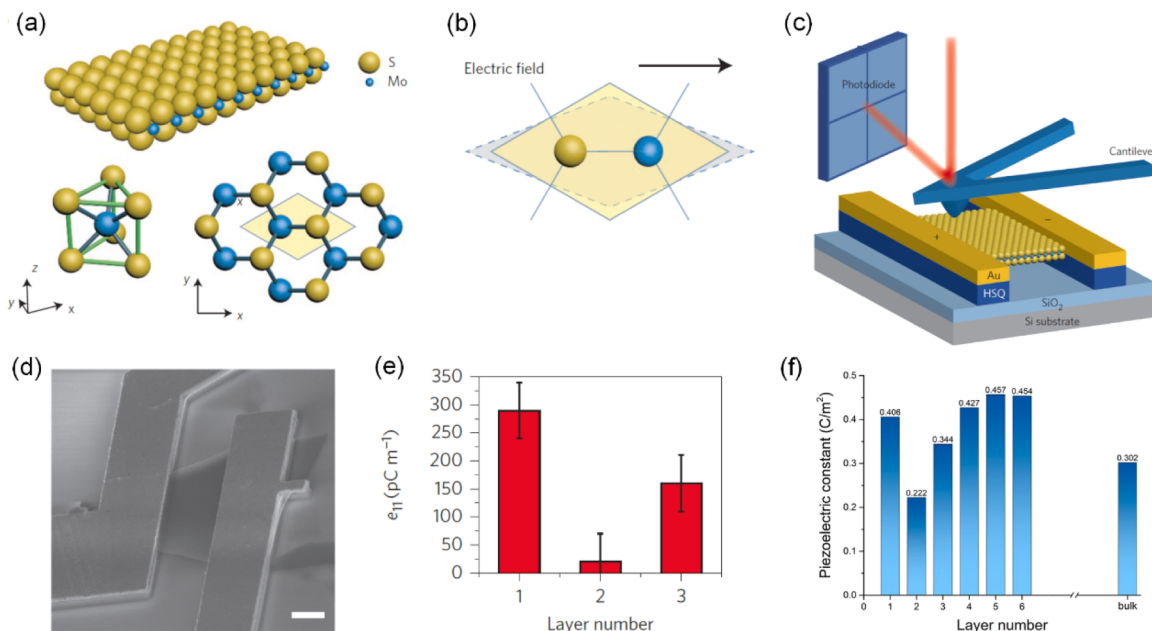


Fig. 4. Piezoelectric property of MoS₂. (a) Structure illustration of a single MoS₂ layer with a thickness of 0.6 nm. (b) Stretch of the Mo-S dipole due to an external electric field applied from the S to the Mo site. (c) Schematic of the in-plane piezoelectric stress measurement set-up. (d) Scanning electron microscopy (SEM) image displaying the free-standing MoS₂ monolayer clamped between the Au electrode and hydrogen silsequioxane posts. Scale bar is 1 μ m. (e) Measured piezoelectric coefficient of mono, bi and tri layers MoS₂; error bars were estimated from the noise level of the force measurement and variations in the device geometry. (f) Calculation results of the piezoelectric constant e_{11} of 3R-MoS₂ as a function of layer number (computed at a fixed strain $\epsilon_{11} = -5\%$). [36]. Copyright 2019, Elsevier. (a-e) Reproduced with permission from ref. [92]. Copyright 2014, Nature Publishing Group. (f) Reproduced with permission from ref. [36]. Copyright 2019, Elsevier.

nanomaterials. On the other hand, S vacancies in MoS_2 are also consolidated to serve as catalytic active centers in many reactions including HER and persulfate activation [96,97]. As a result, fine modulation of the amount of S-vacancy is also a facile approach to boost the catalytic activity of MoS_2 [38].

Unlike 2 H- MoS_2 , the inherent metallic feature of 1 T- MoS_2 endows both the basal planes and edge sites excellent catalytic activity [98]. In addition, the good electric conductivity of 1 T- MoS_2 also facilitates the transport of electrons and ions, which is desirable to catalytic reactions [30,98]. Consequently, the larger number of active sites and better charge transfer of 1 T- MoS_2 allow it more promising in catalysis field than 2 H- MoS_2 . Many theoretical and experimental studies also reported the better catalytic performance of 1 T- MoS_2 in HER and persulfate activation reactions [73,98].

As for 3R- MoS_2 , its catalytic property has been paid less attention thus far, while the different crystal structure and electrical property of 3R- MoS_2 from 2 H- MoS_2 might cause distinct catalytic performance. Several studies reported that bulk 3R- MoS_2 is catalytic reactive towards HER and nitrogen reduction reactions due to the presence of active MoS_2 edges and its catalytic activity is higher than that of bulk 2 H- MoS_2 and even comparable to the exfoliated 1 T phase [69,99–101]. Interestingly, the bulk 3R- MoS_2 was also found to be a better precursor than bulk 2 H phase for preparing 1 T- MoS_2 catalyst showing excellent HER performance via exfoliation [99]. Apparently, 3R- MoS_2 is also supposed to be catalytically reactive towards persulfate activation, while relevant examples have not been reported yet.

2.7. Summary

To summarize, MoS_2 possesses mutable electrical, optical, piezoelectric and catalytic properties which are strongly dependent on the crystal structure of MoS_2 . Among the three polytypes, 1 T- MoS_2 shows metallic behavior while the other two are semiconducting materials. As a result, the charge transfer and NIR absorbance is enhanced in 1 T- MoS_2 compared to 2 H- and 3R- MoS_2 , which renders 1 T- MoS_2 as a better chemical catalyst and photothermal agent. On the other side, the semiconducting nature of 2 H- and 3R- MoS_2 polytypes endows them more intriguing optical and piezoelectric properties than 1 T phase. Between 2 H- and 3R- MoS_2 , their electronic and optical properties are quite

similar, while the piezoelectric property is distinct. Due to the difference in the symmetry of crystal structure, the piezoelectricity in 2 H- MoS_2 is more sensitive to the layer number compared to 3R- MoS_2 , which makes 3R- MoS_2 more attractive as the piezoelectric material. In addition, the physicochemical properties of 2 H/3R- MoS_2 also vary with the layer number, and the nanostructured 2 H/3R- MoS_2 possesses better properties than the bulk material. Therefore, through engineering the dimension and phase of MoS_2 , it is foreseen to act as a versatile persulfate activator, which will be described in detail in the following section.

3. Applications of MoS_2 -based materials in PS-AOPs

In PS-AOPs, the critical factor is the activation of persulfate. The persulfate activation is primarily targeted at the peroxide O-O bond. Principally, with the supply of external thermal, light, electrical, mechanical, and chemical energy, the electron configuration of the O-O bond would change, or the O-O is directly cleaved, giving rise to the production of reactive intermediate complexes and/or free radicals [13]. Due to the variable properties of MoS_2 polytypes, they can not only directly supply chemical energy to activate persulfate (cocatalyst/catalyst), but also convert the light energy (photocatalyst and photothermal agent) and mechanical energy (piezocatalyst) into chemical energy for persulfate activation. Therefore, MoS_2 can serve as a cocatalyst, catalyst, photocatalyst, photothermal agent and piezocatalyst in PS-AOPs (Fig. 5).

Since the three MoS_2 polytypes possess distinct physicochemical properties, they can activate persulfate by different means. Currently, the metallic 1 T- MoS_2 nanosheets with excellent chemical activity are primarily used as catalysts for persulfate activation, while semiconducting 2 H- MoS_2 including both bulk and nanostructured materials with lower catalytic activity than 1 T- MoS_2 is more widely used as a cocatalyst than a catalyst for persulfate activation. Regarding the applications as photocatalyst, photothermal agent and piezocatalyst in PS-AOPs, researchers are focused on the nanostructured 2 H- MoS_2 due to its better optical and piezoelectric properties than the bulk counterpart. In addition, the catalytic, optical and piezoelectric properties of nanostructured 2 H- MoS_2 can be improved via various modification strategies such as phase engineering, defect engineering, doping and compositing with other materials, which further enhance the persulfate

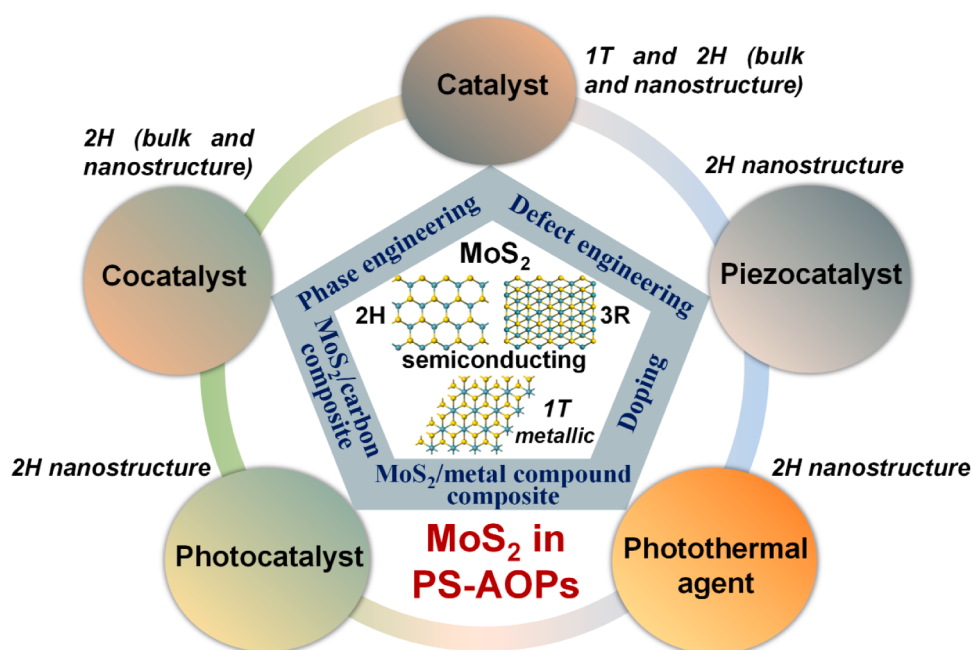


Fig. 5. A schematic summary of chemical modifications on MoS_2 and their applications in PS-AOPs.

activation efficiency and organic pollutant removal [60]. The appealing optical, piezoelectric and catalytic properties of 3R-MoS₂ make it a good candidate as persulfate activator, but applications of both bulk and nanostructured materials in PS-AOPs are rarely reported arising from the limitation of material synthesis.

In this section, the roles that 1 T-MoS₂, 2 H-MoS₂ and 2 H-MoS₂-based nanomaterials can play in PS-AOPs are classified. It should be pointed out that in some cases MoS₂-based materials are able to play a dual role or triple role in PS-AOPs when an external stimulus like light irradiation and mechanical disturbance is present. Therefore, multiple persulfate activation processes probably simultaneously occur when a versatile MoS₂-based material functions in PS-AOPs, and the involved activation mechanisms are also discussed.

3.1. Catalytic activation of persulfate with MoS₂

When MoS₂ is used for catalytic activation of persulfate, its intrinsic surface free charges primarily participate in the redox reactions to initiate persulfate activation. With the presence of active sites in MoS₂, it can directly react with persulfate (as a catalyst) or with other catalyst to boost the persulfate activation (as a cocatalyst) [43,49]. Moreover, modifications like heteroatom doping and compositing with other materials have been performed on MoS₂ (primarily on 2 H-MoS₂ nanomaterial) in order to further enhance the persulfate activation efficiency. Especially, when MoS₂ is modified with a metallic persulfate activator, the resulted composites can play a dual role as both catalyst and cocatalyst in persulfate activation, which is conducive to the elimination of organic pollutants [55,102]. In the sub-sections below, the different roles of MoS₂ and 2 H-MoS₂-based nanomaterials in catalytic persulfate activation processes are discussed.

3.1.1. 2 H-MoS₂ as a cocatalyst for boosting persulfate activation over metal ions

3.1.1.1. Cocatalytic mechanism. Homogeneous metal ions are well-known catalysts for activating H₂O₂ as well as persulfate to produce free radicals [103,104]. The catalytic activity of metal ions originates from their polyvalent nature, which allows them to donate electrons to persulfate and thus induce the cleavage of peroxide O-O bond [104]. Peroxymonosulfate (PMS, HSO₅⁻) and peroxydisulfate (PDS, S₂O₈²⁻) are two typical parent oxides used in PS-AOPs, while metal ions show different activation efficiency towards them [105]. In general, Co²⁺ is the most efficient one for PMS activation while Ag⁺ and Fe²⁺ are the most efficient two for PDS activation [106]. The homogeneous activation processes can be described by Eqs. 1–3:



where Mⁿ⁺ refers to a metal ion. However, one of the drawbacks in such homogeneous persulfate system is the low conversion from M⁽ⁿ⁺¹⁾⁺ to Mⁿ⁺, which results in a high consumption of metal ions [105]. To overcome this problem, introducing a cocatalyst is a feasible option. Xing et al. firstly utilized bulk MoS₂ as an inorganic cocatalyst for Fenton reaction and discovered that the reductive Mo(IV) active sites could quickly transform Fe³⁺ into Fe²⁺, giving rise to largely improved degradation of organic micropollutants [42]. Inspired by this pioneering work, bulk MoS₂ has been widely used as a cocatalyst to promote the Fe³⁺/Fe²⁺ and Co³⁺/Co²⁺ cycles in homogeneous PMS or PDS systems (Eq. 4) [44–46,107–113].

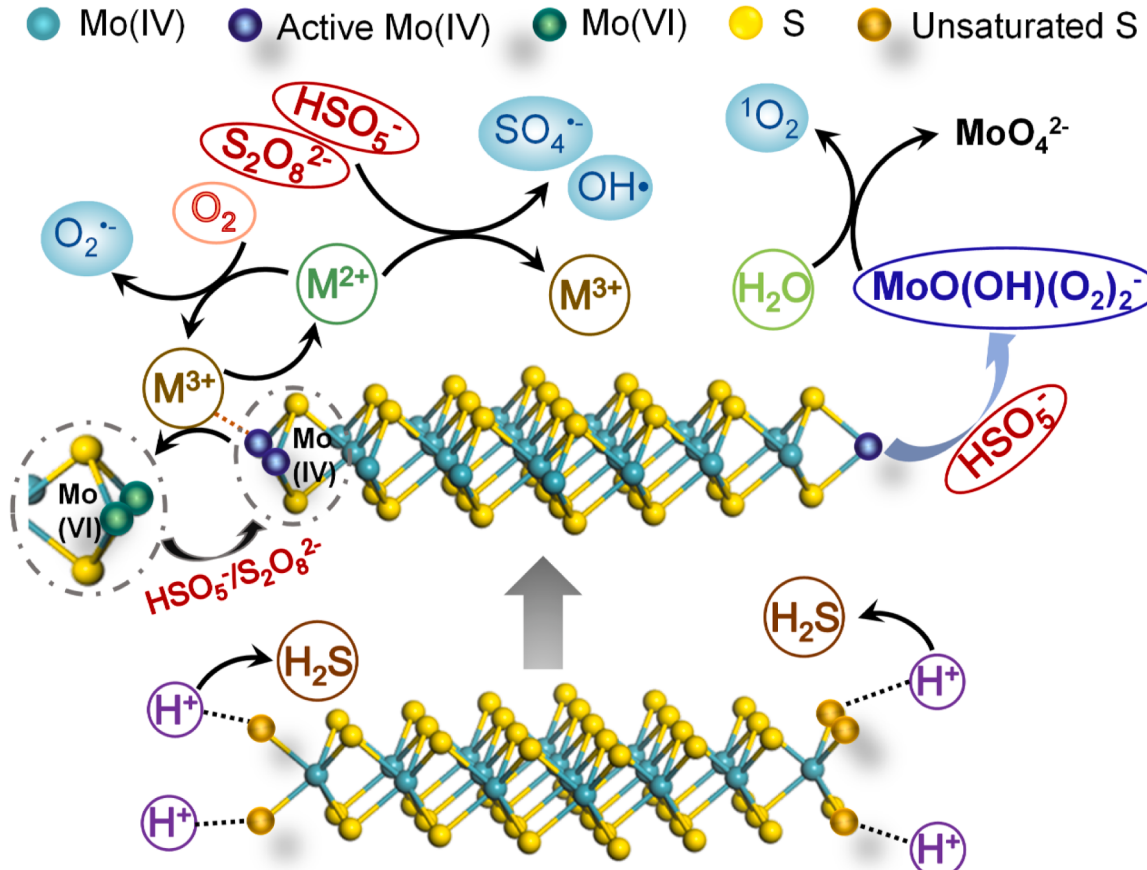
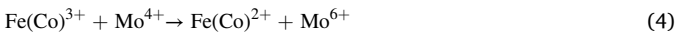


Fig. 6. Schematic illustration of the co-catalytic mechanism of MoS₂ in persulfate activation.



The role of MoS₂ playing in the homogeneous persulfate system is described in Fig. 6. Firstly, Fe²⁺/Co²⁺ ions react with HSO₅⁻/S₂O₈²⁻ ions to produce free radicals (SO₄[•] and •OH, noting that SO₄[•] can be converted into •OH via hydrolysis) and Fe³⁺/Co³⁺. Then the surface exposed Mo(IV) atoms serve as the active sites to reduce Fe³⁺/Co³⁺ into Fe²⁺/Co²⁺ along with the generation of Mo(VI) species in MoS₂. At the meantime, the unsaturated S atoms at the edges of MoS₂ are able to capture protons in the solution to form H₂S, resulting in the formation of sulfur vacancies and more exposure of active Mo(IV) atoms. This can further boost the redox cycle of metal ion catalysts. Afterwards, Mo(VI) is reduced back to Mo(IV) through the reaction with HSO₅⁻/S₂O₈²⁻ ion. With the dynamic Fe³⁺(Co³⁺⁾/Fe²⁺(Co²⁺) and Mo(VI)/Mo(IV) cycles, free radicals are continuously replenished and rapidly degrade the organic pollutants.

According to the Raman spectroscopic results, the redox reaction between MoS₂ and Fe³⁺/Co³⁺ occurs via the formation of Mo-O-Fe(Co) bond [42]. Overall, the reducing Mo(IV) sites in MoS₂ directly participated in the Fe³⁺(Co³⁺⁾/Fe²⁺(Co²⁺) redox cycles and the reducing sulfur sites served as electron donors to regenerate the reducing metal sites. The vital role of Mo(IV) active sites in MoS₂ cocatalyst is further supported by the results that MoO₂ is also capable of accelerating persulfate activation over metal ions [114].

3.1.1.2. Application of 2 H-MoS₂ as a cocatalyst in PS-AOPs. The promising potential of MoS₂ in boosting homogeneous persulfate-based oxidative systems towards practical wastewater treatment and gaseous volatile organic compounds (VOCs) has been widely demonstrated in the literature (Table 1) [43,44,46,107–113,115–124]. Overall, the MoS₂ cocatalyst is primarily in the bulk 2 H phase because bulk material is commercially available and shows good effectiveness. Notably, most of the homogeneous persulfate-based systems are focused on the Fe ion because Fe ion is less toxic than Co ion. Moreover, a considerable number of studies reported the comparable removal performances of MoS₂-cocatalyzed Fe³⁺/persulfate systems to the MoS₂-cocatalyzed Fe²⁺/persulfate systems although Fe³⁺ has much lower catalytic activity than Fe²⁺, which further consolidated the efficiency of MoS₂ in accelerating Fe³⁺/Fe²⁺ redox cycle. The advantage of Fe³⁺ over Fe²⁺ is that the former is more stable and ubiquitous in natural water bodies than the latter, which is beneficial to the practical water treatment [107]. Especially, with the cocatalytic effect of MoS₂, the homogenous persulfate system could achieve excellent degradation performance even at a trace amount of Fe ion (e.g., 1 mg L⁻¹), which reduces the production of sludge and waste of Fe resources [125].

For instance, Luo and co-workers reported that the Fe³⁺/PMS/MoS₂ (bulk) system exhibited much improved degradation efficiency of Rhodamine B (RhB) than the Fe³⁺/PMS system (Fig. 7) [46]. Particularly, with the optimized experimental parameters, above 90% RhB was removed by Fe³⁺/PMS/MoS₂ system within 10 min over a wide range of pH (3–11). The co-catalytic system also manifested good removal performance for a variety of organic contaminants like antibiotics, bisphenol A (BPA), etc. In addition, MoS₂ could be repeatedly used for 8 cycles of RhB degradation without a significant decline of degradation efficiency, suggesting its good stability. Furthermore, a RhB removal efficiency of 58.6% in the synthetic wastewater was still attained by the Fe³⁺/PMS/MoS₂ system.

Since the exposure of Mo(IV) site is essential to attain the fast Mⁿ⁺¹/Mⁿ redox cycles during persulfate activation process, the particle size of MoS₂ can significantly affect its cocatalytic effect. Apparently, MoS₂ with a smaller particle size has a larger number of surface exposed Mo(IV) atoms and edge S atoms, which are beneficial to the catalytic activity of MoS₂. For instance, the commercial bulk MoS₂ with a smaller particle size was observed to be more efficient for improving the sulfamethoxazole (SMX) degradation performance of a Fe²⁺/PMS system [42,109]. The Fe³⁺/PMS system cocatalyzed by 2 H-MoS₂ nanoflowers

(NFs) achieved a higher tetracycline (TC) removal efficiency compared to the Fe³⁺/PMS system cocatalyzed by bulk MoS₂, especially the initial concentration of TC was higher and dosage of cocatalyst was much lower in the Fe³⁺/PMS/MoS₂ NFs system [46,120]. Especially, a cocatalytic Fe²⁺/PMS system with 3D-MoS₂ sponge loaded with 2 H-MoS₂ NFs and graphene oxide (SMG) synthesized by Xing et al. was reported to manifest high efficacy on treating simulated sulfadiazine (SDZ)-contained wastewater in the pilot-scale experiment (Fig. 8a-c) [26].

Defects in MoS₂ (e.g., sulfur vacancies, Mo vacancies) can not only increase the number of exposed active sites but also change the electronic structure of MoS₂ and thus facilitate the electron transfer in redox reactions [38]. Consequently, adoption of defect engineering is a feasible approach to enhance the cocatalytic performance of MoS₂. For example, Zhang's group employed an annealing treatment in H₂ atmosphere on bulk MoS₂ to create sulfur vacancies and reported the enhanced cocatalytic effect of defective bulk MoS₂ (MoS₂-D) samples on a Fe³⁺/PDS system towards p-chloroaniline (PCA) degradation (Fig. 8d-f) [45]. By performing density functional theory (DFT) calculations, it was revealed that the presence of sulfur vacancies not only reduces the valence state of the neighboring Mo atom (i.e., makes the Mo atom more reducing) but also increases the adsorption energy between Fe³⁺ and MoS₂. As a consequence, the improved defective level is conducive to the cocatalytic activity of MoS₂ towards Fe³⁺-catalyzed PDS activation and the degradation of the organic pollutant. However, the authors also found that the PDS activation efficiency was not continuously increased with the defective level of MoS₂. It seems that the sulfur vacancies could only improve the cocatalytic activity of MoS₂ to some extent.

Despite of the good cocatalytic activity of MoS₂, several critical issues remaining to be addressed before the practical application. For instance, the long-term performance of MoS₂ is not satisfactory [120, 121]. According to the cocatalytic mechanism in Section 3.1.1.1, the protonation of sulfur atoms and exposure of Mo(IV) active sites in MoS₂ are crucial, which in return results in the leaching of Mo in water especially under acid condition and instability of MoS₂ [117,121]. In addition, the reduction of Mo(VI) into Mo(IV) would be gradually suppressed during the catalytic persulfate activation process, which also deteriorates the stability of MoS₂ cocatalyst [121]. Meanwhile, most of the reported MoS₂ cocatalysts are in the powdery form, which is not conducive to their recovery and the practical operation. Immobilizing the cocatalyst onto suitable support might be a feasible solution to overcome these problems and further efforts should be made.

3.1.1.3. Activation mechanism in Mⁿ⁺¹/MoS₂/persulfate system. Regarding the persulfate activation pathway in the MoS₂-cocatalyzed homogeneous persulfate systems, it is commonly reported that free radicals were produced and accounted for the organics degradation. However, several studies discovered that O₂[•] and ¹O₂ as nonradical species can also be produced from persulfate activation besides free radicals [108,111]. The formation of O₂[•] and ¹O₂ is attributed to several reasons. Zhang et al. proposed that the interaction between MoS₂ and HSO₅ could result in the formation of a Mo(VI) peroxy-complex intermediate in the cocatalytic Fe²⁺/PMS/MoS₂ system and this complex intermediate was further converted into ¹O₂ via hydrolysis (Fig. 6) [108]. In addition, the accelerated reduction of Fe³⁺ into Fe²⁺ in the cocatalytic Fe³⁺/PMS/MoS₂ system could facilitate the activation of dissolved oxygen into O₂[•] by Fe²⁺ and the reaction between O₂[•] and •OH produces ¹O₂ [115]. These phenomena suggested that the introduction of a solid cocatalyst into a homogeneous catalytic persulfate system might affect the catalytic mechanism since the involved reactions primarily occurred at the solid/liquid interface rather than in the aqueous solution, while the interface property has a great influence on the catalytic reaction [126]. Especially, the reducing Mo(IV) site on MoS₂ could also react with persulfate, which might also affect the activation processes between metal ions and persulfate.

In summary, both the nanostructured and bulk 2 H-MoS₂ are good

Table 1
MoS₂ as a cocatalyst in PS-AOPs.

Cocatalytic system	Contaminant	Removal Efficiency	Conditions	Mechanism	Reference
Fe ²⁺ /PMS/MoS ₂	2,4,6-trichlorophenol (TCP)	> 95% in 30 min	Fe ²⁺ = 0.2 mM MoS ₂ = 1 g L ⁻¹ PMS = 0.5 mM TCP = 100 μM	SO ₄ ^{·-} and •OH accounted for TCP oxidation	[43]
Fe ²⁺ /PMS/MoS ₂	RhB	94.7% in 60 min	Fe ²⁺ = 54 μM PMS = 0.5 mM MoS ₂ = 0.3 g L ⁻¹ RhB = 10 mg L ⁻¹	SO ₄ ^{·-} and •OH were generated while SO ₄ ^{·-} dominated RhB oxidation	[44]
Fe ²⁺ /PDS/MoS ₂	RhB	87.6% in 60 min	Fe ²⁺ = 54 μM PDS = 0.25 mM MoS ₂ = 0.3 g L ⁻¹ RhB = 10 mg L ⁻¹	SO ₄ ^{·-} and •OH were generated while SO ₄ ^{·-} dominated RhB oxidation	[44]
Fe ²⁺ /PMS/MoS ₂	SMX	88.5% in 6 min	Fe ²⁺ = 70 μM PMS = 0.075 mM MoS ₂ = 0.3 g L ⁻¹ SMX = 25 μM	SO ₄ ^{·-} and •OH accounted for SMX oxidation	[109]
Fe ²⁺ /PDS/MoS ₂	Sulfisoxazole (SIX)	97.1% in 40 min	Fe ²⁺ = 30 μM PDS = 0.4 mM MoS ₂ = 0.02 g L ⁻¹ SIX = 40 μM	SO ₄ ^{·-} and •OH accounted for SIX oxidation	[112]
Fe ²⁺ /PDS/MoS ₂	2,4,4'-trichlorobiphenyl (PCB28)	79.5% in 20 min	Fe ²⁺ = 20 μM PDS = 1 mM MoS ₂ = 0.1 g L ⁻¹ PCB28 = 1 mg L ⁻¹	Surface-bound SO ₄ ^{·-} and •OH accounted for PCB28 oxidation	[110]
Fe ²⁺ /PDS/MoS ₂	SDZ	97.1% in 60 min	Fe ²⁺ = 30 μM PDS = 0.05 mM MoS ₂ = 0.1 g L ⁻¹ SDZ = 10 mg L ⁻¹ Visible light	SO ₄ ^{·-} , ¹ O ₂ and h ⁺ accounted for SDZ oxidation	[116]
Fe ²⁺ /PMS/MoS ₂	Phenacetin (PNT)	94.3% in 15 min	Fe ²⁺ = 25 μM PMS = 0.125 mM MoS ₂ = 0.1 g L ⁻¹ PNT = 25 μM	SO ₄ ^{·-} , •OH, O ₂ [·] and ¹ O ₂ accounted for PNT oxidation	[111]
Fe ²⁺ /PMS/MoS ₂	Acetaminophen (ACT)	94.5% in 30 min	Fe ²⁺ = 64.5 μM PMS = 0.5 mM MoS ₂ = 0.1 g L ⁻¹ ACT = 20 mg L ⁻¹	SO ₄ ^{·-} , •OH and ¹ O ₂ were generated while ¹ O ₂ dominated ACT oxidation	[108]
Fe ²⁺ /PMS/3D-MoS ₂ sponge	SDZ	97.87% after 16 days	Fe ²⁺ = 0.01 M PMS = 16.2 mM per day Sponge area = 45 * 45 cm ² SD = 120 mg L ⁻¹	SO ₄ ^{·-} and •OH accounted for SDZ oxidation	[26]
Fe ²⁺ /PMS/MoS ₂ NFs coated on polyaniline nanotubes	Thiamphenicol (TAP)	99% in 15 min	Fe ²⁺ = 2 μM PMS = 0.5 mM MoS ₂ @PANI = 0.02 g L ⁻¹ TAP = 5 mg L ⁻¹	SO ₄ ^{·-} , •OH, O ₂ [·] and ¹ O ₂ accounted for TAP oxidation	[117]
Fe ³⁺ /PMS/MoS ₂	SDZ	94.3% in 30 min	Fe ³⁺ = 17.9 μM PMS = 0.5 mM MoS ₂ = 0.5 g L ⁻¹ SDZ = 5 mg L ⁻¹	SO ₄ ^{·-} , •OH and ¹ O ₂ were generated while SO ₄ ^{·-} and ¹ O ₂ dominated SDZ oxidation	[107]
Fe ³⁺ /PMS/MoS ₂	RhB	92.5% in 10 min	Fe ³⁺ = 0.1 mM PMS = 1.5 mM MoS ₂ = 0.3 g L ⁻¹ RhB = 10 mg L ⁻¹	SO ₄ ^{·-} and •OH were generated while SO ₄ ^{·-} dominated RhB oxidation	[46]
Fe ³⁺ /PDS/MoS ₂	Phenol	99.6% in 60 min	Fe ³⁺ = 0.125 mM PDS = 5 mM MoS ₂ = 0.4 g L ⁻¹ Phenol = 50 mM	Surface-bound SO ₄ ^{·-} and •OH accounted for phenol oxidation	[121]
Fe ³⁺ /PMS/MoS ₂ NFs	TC	93.2% in 20 min	Fe ³⁺ = 0.1 mM PMS = 1 mM MoS ₂ = 0.05 g L ⁻¹ TC = 30 mg L ⁻¹	SO ₄ ^{·-} , •OH, Fe ^{IV} =O and ¹ O ₂ accounted for TC oxidation	[120]
Fe ³⁺ /PDS/MoS ₂	PCA	100% in 30 min	Fe ³⁺ = 0.604 mM PDS = 2.5 mM MoS ₂ = 0.3 g L ⁻¹ PCA = 100 μM	SO ₄ ^{·-} and •OH accounted for PCA oxidation	[45]
Fe ³⁺ /PMS/MoS ₂	Styrene	97% (flow mode)	Fe ³⁺ = 0.5 mM PMS = 1.6 mM MoS ₂ = 0.015 g L ⁻¹ Styrene = 30 ppmv	SO ₄ ^{·-} , •OH and O ₂ [·] accounted for styrene oxidation	[115]

(continued on next page)

Table 1 (continued)

Cocatalytic system	Contaminant	Removal Efficiency	Conditions	Mechanism	Reference
nZVI/PDS/MoS ₂	SMX	98.6% in 30 min	nZVI = 0.1 g L ⁻¹ PDS = 1.2 mM MoS ₂ = 0.1 g L ⁻¹ SMX = 20 μM	SO ₄ ²⁻ and •OH accounted for SMX oxidation	
Co ²⁺ /PMS/MoS ₂	RhB	100% in 5 min	Co ²⁺ = 2 μM PMS = 0.2 mM MoS ₂ = 0.5 g L ⁻¹ RhB = 30 μM	SO ₄ ²⁻ and •OH accounted for RhB oxidation	[113]

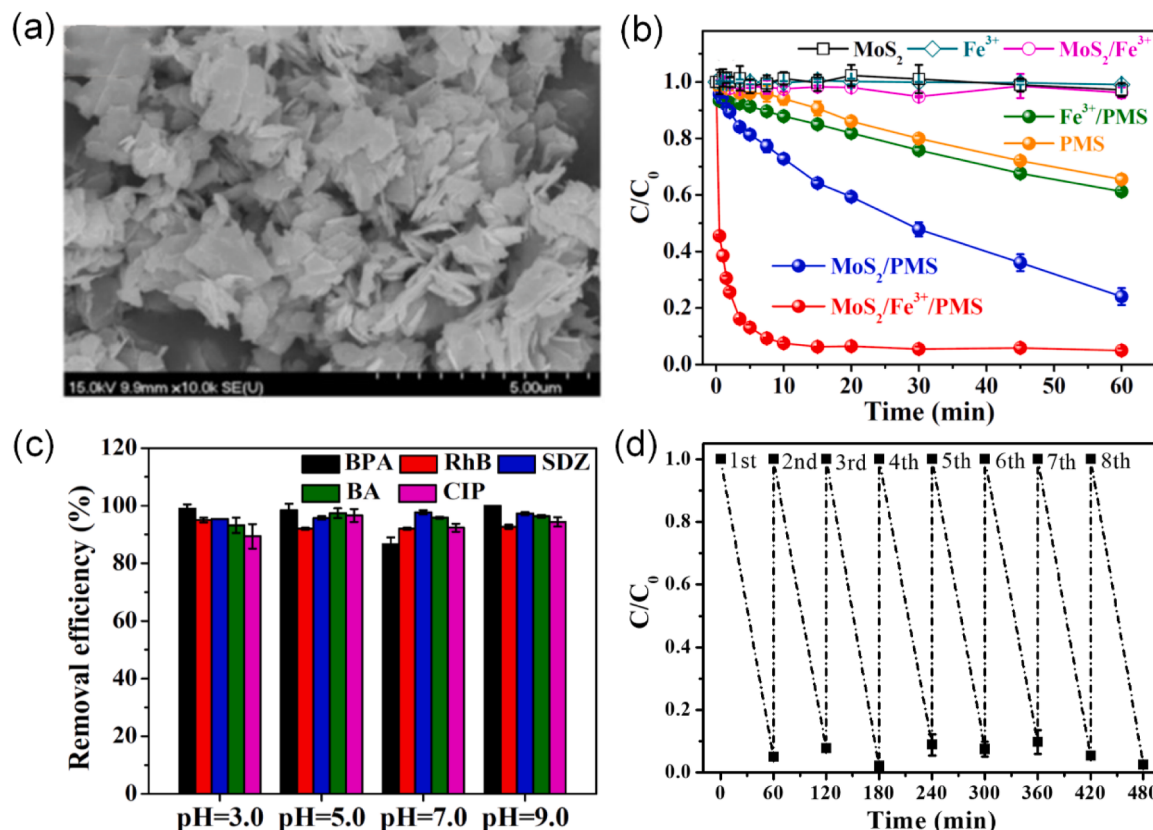


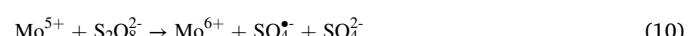
Fig. 7. (a) SEM image of bulk 2 H-MoS₂ cocatalyst. (b) RhB degradation by MoS₂/PMS and MoS₂/Fe³⁺/PMS systems. (c) Comparison of removal efficiencies of various organic pollutants in MoS₂/Fe³⁺/PMS system under different initial pH values. (d) Cycling test of bulk 2 H-MoS₂ cocatalyst for RhB degradation. Reproduced with permission from ref. [46]. Copyright 2020, Elsevier

cocatalysts for metal ion/persulfate systems, while the former is more efficient than the latter due to the better exposure of active sites in the nanostructure than in the bulk structure. Meanwhile, the reported MoS₂ cocatalysts are the 2 H phase (the bulk MoS₂ possibly contains different phases but 2 H is the major phase), while the cocatalytic performances of 3 R and 1 T phases for persulfate activation are not investigated. Therefore, the phase effect on the MoS₂ cocatalytic activity in metal ion/persulfate system is unclear yet. Moreover, the long-term performance and recycling of MoS₂-based cocatalyst are critical challenges that should be overcome in future work.

3.1.2. MoS₂ as a catalyst for persulfate activation

Because of the strong reducing ability of Mo(IV) atoms and efficient charge transfer induced by S-Mo-S bonds, redox reactions can also occur between MoS₂ and persulfate molecules, causing the cleavage of the O-O bond [47,48]. However, an unambiguous understanding of the catalytic sites on MoS₂ for persulfate activation and the intrinsic catalytic mechanisms are still not achieved. Generally speaking, during the persulfate activation process, the Mo(IV) in MoS₂ was first oxidized into Mo

(V) and further into Mo(VI) by persulfate ions, accompanying with the production of free radicals (Eqs. 5–10).



Previous studies have demonstrated that several factors including the phase, dimension (bulk or nanostructured) and sulfur vacancies affect the catalytic activity of MoS₂ in HER [38]. However, in the case of persulfate activation, the factors of phase and sulfur vacancies exert a significant influence while the dimension factor has little influence on the catalytic activity of MoS₂.

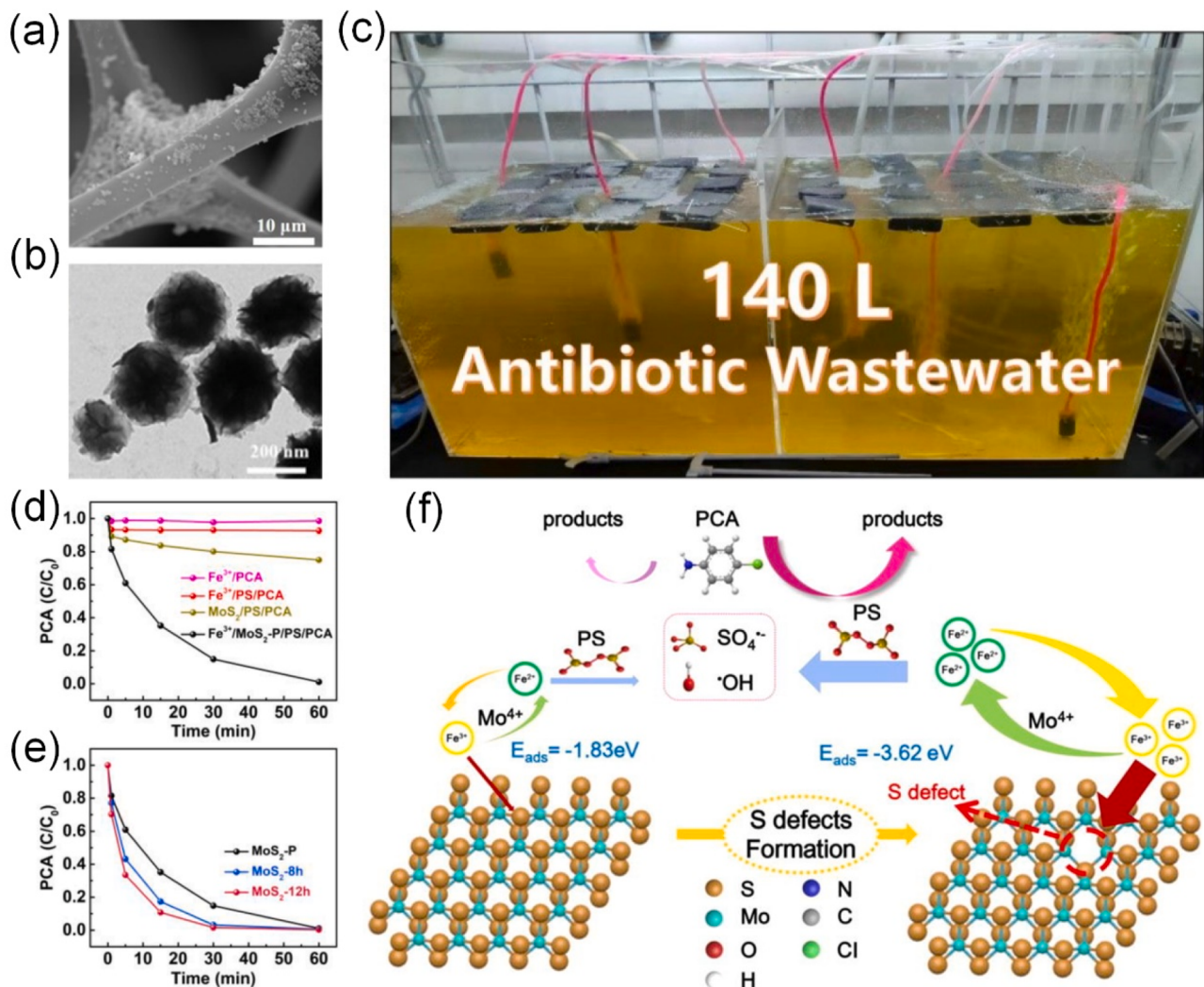


Fig. 8. (a) SEM image of SMG. (b) High resolution transmission electron microscopy (HRTEM) image of the as-prepared MoS₂ nanospheres. (c) The photo of 140 L SD (totally 120 mg L⁻¹) degradation device based on the Fe²⁺/PMS/SMG system. (d) PCA degradation by different PDS activation systems. (e) PCA degradation in a Fe³⁺/PDS system with different MoS₂-D cocatalysts. (f) Schematic illustration of the co-catalytic mechanism of MoS₂-D in the Fe³⁺/PDS system. (a-c) Reproduced with permission from ref. [26]. Copyright 2020, Wiley-VCH Verlag GmbH & Co. KGaA, Weinheim. (d-f) Reproduced with permission from ref. [45]. Copyright 2021, Elsevier.

3.1.2.1. Comparison of catalytic activity between 1 T- and 2 H-MoS₂. The effect of phase on the catalytic activity of MoS₂ towards persulfate activation is similar to that in the case of HER. 1 T-MoS₂ outperforms 2 H-MoS₂ in persulfate activation because of the larger number of active sites and more efficient charge transfer kinetics in 1 T phase. The DFT calculations by Chen et al. suggest that the (001) edges and (100) surfaces are the main catalytic sites in 1 T-MoS₂ for PMS activation because the (001) edges and (100) surfaces exhibit large adsorption energies (E_{ads}) towards PMS and the O-O bond ($\text{I}_{\text{O-O}}$) in the adsorbed PMS molecule was stretched from 1.346 Å (free PMS) to 1.403 Å (Fig. 9a) [48,73]. However, the theoretical works by Ao's group suggest that both the edge Mo and S atoms in 2 H-MoS₂ are inactive to persulfate activation because the decomposition of O-O bond in PMS/PDS molecules over the edge Mo or S atoms was endothermic with a certain amount of formation energy (Fig. 9b) [56,57]. This is somehow contradictory to the previous findings that the edge Mo atoms are active for HER reaction [38]. It seems that 2 H-MoS₂ probably exhibits different catalytic activity in different reactions, which deserves further investigation to obtain an insightful understanding on the catalytic sites of 2 H-MoS₂ in various reactions.

The higher catalytic activity of 1 T-MoS₂ than 2 H-MoS₂ is also

experimentally confirmed. For instance, Wang et al. reported that the 1 T-MoS₂ NFs prepared via a two-stage solvothermal method could remove 71.6% imidacloprid (IMI) within 180 min, while the 2 H-MoS₂ NFs and bulk MoS₂ only attained the IMI removal efficiency of 17.4% and 11.7%, respectively [50]. Especially, the catalytic activity of 1 T-MoS₂ towards persulfate activation is also much higher than some 2 H-MoS₂-based composite catalysts like MoS₂/CuFe₂O₄ and Co-doped MoS₂ NFs [127]. However, the metastable 1 T phase would be transformed into 2 H phase and the active edges and basal plane surfaces of 1 T-MoS₂ could be oxidized during the persulfate activation process, resulting in the low chemical stability of the catalyst [127]. Interestingly, through assembling the powdery 1 T-MoS₂ into stacked nanosheets (membrane), the easily oxidized surface and edges can be significantly preserved, thus improving the durability of the catalyst [127]. Moreover, it was reported that the diffusion distance of aqueous organic molecules was decreased and the mass transfer between as-activated ROS and targeted organic pollutant within 1 T-MoS₂ membrane was greatly promoted due to the confinement of fluids between nanolayers (Fig. 10), which boosted the removal of organic pollutant [48]. The outstanding removal performance of 1 T-MoS₂ membrane offer a novel nanofluid reactor of AOPs for water

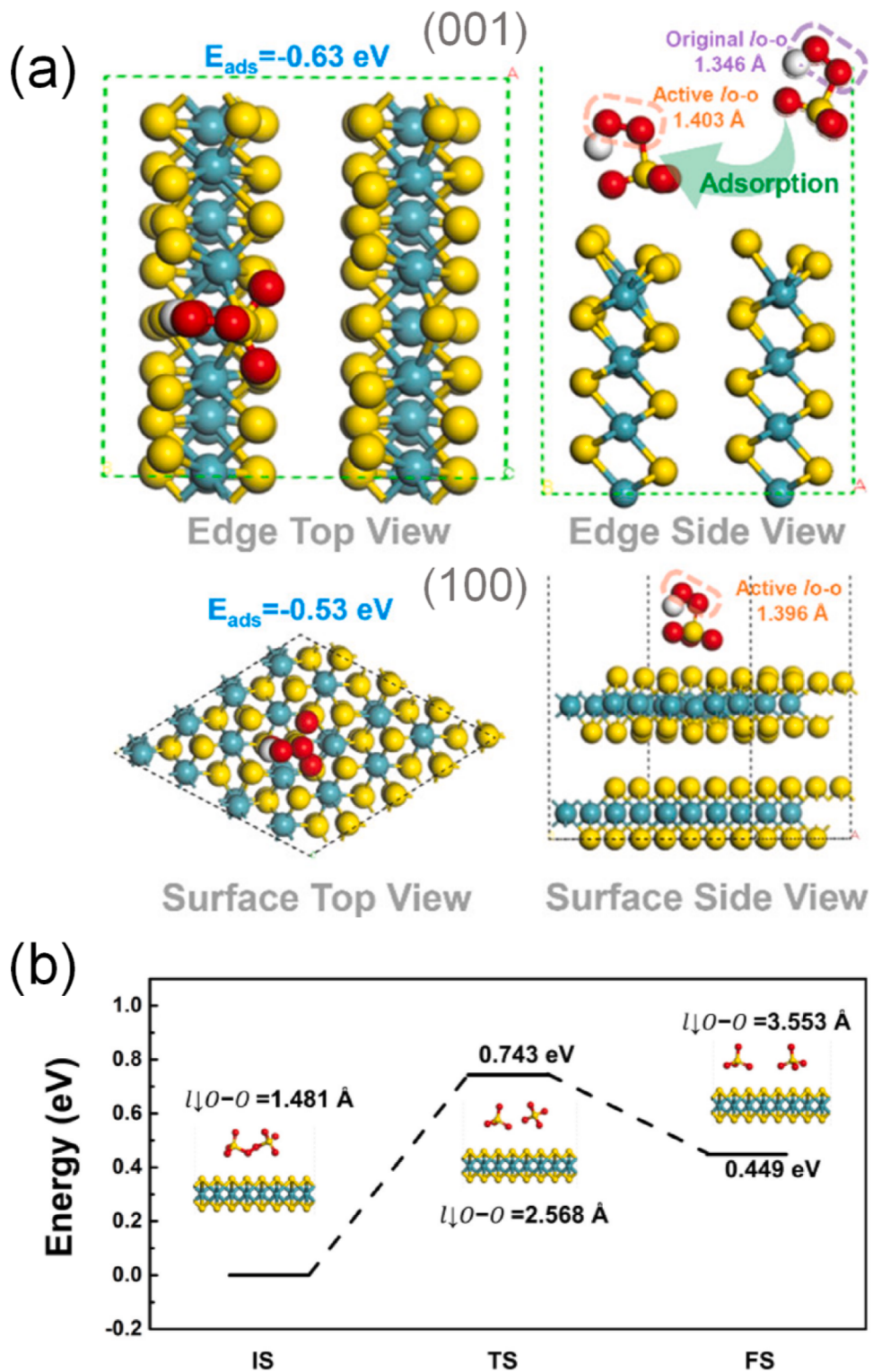


Fig. 9. (a) PMS adsorption free energy on edge and surface sulfur vacancies of the 1 T MoS₂ nanosheets. Red, yellow, white and blue ball are O, S, H and Mo atoms, respectively. (b) Activation pathway of PDS on a 2 H-MoS₂ monolayer to evolve two SO₄²⁻ groups.
 (a) Reproduced with permission from ref. [73]. Copyright 2019, American Chemical Society. (b) Reproduced with permission from ref. [56]. Copyright 2021, Elsevier.

purification, which might be an emerging research direction in the field of environmental remediation.

Although 1 T-MoS₂ nanomaterials possess higher catalytic activity towards persulfate activation compared to 2 H-MoS₂ nanomaterials, while the synthetic procedures of the former are more complex than

those of the latter, which limits the wide application of 1 T-MoS₂. In this regard, preparing multiphasic 1 T/2 H MoS₂ nanostructures with a high level of 1 T phase via the facile hydrothermal method is an alternative way to obtain high-performance MoS₂ catalysts. Several studies demonstrated that the persulfate activation efficiency was increased

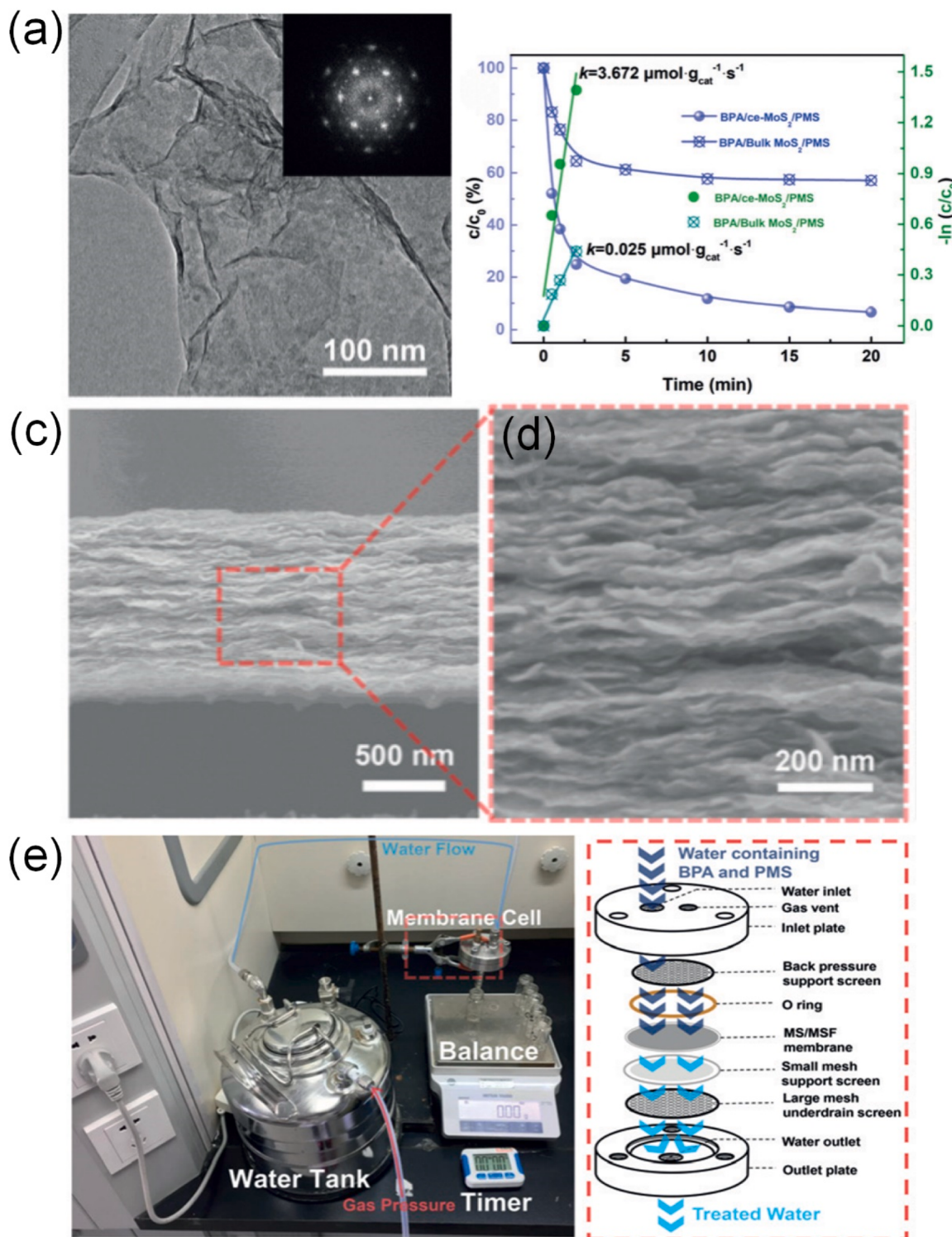


Fig. 10. (a) HRTEM image of ce-MoS₂. (b) Degradation and first-order reaction kinetics of BPA removal by catalytic PMS using bulk MoS₂/ce-MoS₂. (c, d) High-magnification SEM images of the cross-sectional view of MSF-0.5 membrane. (e) Picture of the experimental set-up, with a schematic illustration of the configuration of the flow-through device (right).

Reproduced with permission from ref. [48]. Copyright 2019, Wiley-VCH Verlag GmbH & Co. KGaA, Weinheim.

with the 1 T content in the multiphasic 1 T/2 H MoS₂ nanostructures, suggesting the vital role of 1 T phase in MoS₂-catalyzed persulfate activation [72,73].

For 2 H-MoS₂, it is found that the dimension reduction from bulk to few-layered structure has little promotion effect on its catalytic activity towards persulfate activation. This is because both the Mo and S edges in

2 H-MoS₂ are inactive to persulfate activation, and the exposure of edges is not a critical factor determining the catalytic activity of 2 H-MoS₂. As a matter of fact, the results documented in the literature suggest the higher persulfate activation efficiency of bulk MoS₂ than the nanostructured counterparts. It can be seen from Table 2 that 2 H-MoS₂ nanosheets/NFs commonly show poor catalytic activity towards

Table 2MoS₂ and 2 H-MoS₂-based nanomaterials as catalysts in PS-AOPs.

Sample	Synthesis method	Contaminant	Removal Efficiency	Conditions	Mechanism	Reference
1 T-MoS ₂	Chemical lithium intercalation	BPA	100% in 20 min	Catalyst = 1.5 mg L ⁻¹ PMS = 0.081 mM BPA = 2 mg L ⁻¹	SO ₄ ^{•-} and •OH were generated while SO ₄ ^{•-} dominated BPA oxidation	[48]
1 T-MoS ₂	Chemical lithium intercalation	Orange II (OII)	100% in 120 min	Catalyst = 8.33 mg L ⁻¹ PMS = 0.65 mM OII = 50 μM	SO ₄ ^{•-} and •OH accounted for OII oxidation	[127]
1 T-MoS ₂	Two-stage solvothermal	IMI	87.1% in 180 min	Catalyst = 0.5 g L ⁻¹ PMS = 6 mM IMI = 10 ppm	SO ₄ ^{•-} and •OH accounted for IMI oxidation	[50]
1 T/2 H MoS ₂ NFs	Hydrothermal	2,4-dichlorophenoxyacetic acid (2,4-D)	~95% in 60 min	Catalyst = 0.1 g L ⁻¹ PMS = 0.5 mM 2,4-D = 25 μM	SO ₄ ^{•-} and •OH accounted for 2,4-D oxidation	[73]
2 H MoS ₂ NFs	Hydrothermal	Phenol	17% in 180 min	Catalyst = 0.3 g L ⁻¹ PMS = 3.25 mM Phenol = 10 mg L ⁻¹	SO ₄ ^{•-} and •OH accounted for phenol oxidation	[57]
2 H MoS ₂ nanosheets	Hydrothermal	Fluoxetine	38.6% in 20 min	Catalyst = 0.1 g L ⁻¹ PMS = 1 mM Fluoxetine = 20 mg L ⁻¹	Not investigated	[102]
2 H MoS ₂ nanosheets	Hydrothermal	Sulfonamides (SA)	19.8% in 15 min	Catalyst = 0.4 g L ⁻¹ PMS = 1 mM SA = 0.116 mM	Not investigated	[53]
2 H MoS ₂ single crystal	Chemical vapor transport	ATZ	~61.5% in 20 min	Catalyst = 0.1 g L ⁻¹ PMS = 0.5 mM ATZ = 40 μM	SO ₄ ^{•-} and •OH accounted for ATZ oxidation	[138]
Bulk MoS ₂	Natural molybdenite	Orange G (OG)	100% in 60 min	Catalyst = 3 g L ⁻¹ PMS = 5 mM OG = 0.1 mM	SO ₄ ^{•-} , •OH, O ₂ ^{•-} and ¹ O ₂ accounted for OG oxidation	[47]
Bulk MoS ₂	Commercial	Carbamazepine (CBZ)	100% in 30 min	Catalyst = 0.4 g L ⁻¹ PMS = 0.6 mM CBZ = 21.2 μM	Free SO ₄ ^{•-} accounted for CBZ oxidation	[49]
Bulk MoS ₂	Commercial	CBZ	100% in 30 min	Catalyst = 0.4 g L ⁻¹ PDS = 0.6 mM CBZ = 21.2 μM	Free and surface-bound SO ₄ ^{•-} accounted for CBZ oxidation	[49]
Bulk MoS ₂	Commercial	Phenol	80% in 25 min	Catalyst = 0.8 g L ⁻¹ PMS = 0.5 mM Phenol = 10 mg L ⁻¹	SO ₄ ^{•-} , •OH and ¹ O ₂ accounted for phenol oxidation	[128]
Bulk MoS ₂	Commercial	BPB	100% in 180 min	Catalyst = 1 g L ⁻¹ PMS = 5 mM BPB = 2.5 mg L ⁻¹	SO ₄ ^{•-} , •OH and ¹ O ₂ were generated while •OH and SO ₄ ^{•-} dominated BPB oxidation	[51]
Bulk MoS ₂	Commercial	BPB	100% in 180 min	Catalyst = 1 g L ⁻¹ PDS = 5 mM BPB = 2.5 mg L ⁻¹	• OH, ¹ O ₂ and O ₂ ^{•-} were generated while •OH dominated BPB oxidation	[51]
Bulk MoS ₂	Commercial	ATZ	100% in 20 min	Catalyst = 0.1 g L ⁻¹ PMS = 100 μM ATZ = 40 μM	surface≡Mo-OOSO ₃ complex accounted for ATZ oxidation	[129]
Defective bulk MoS ₂	Ball milling	TC	77.2%–83.6% in 60 min	Catalyst = 0.3 g L ⁻¹ PMS = 1 mM TC = 20 mg L ⁻¹	SO ₄ ^{•-} , •OH, O ₂ ^{•-} and ¹ O ₂ were generated while ¹ O ₂ dominated TC oxidation	[97]
Biochar-MoS ₂ nanosheets	Hydrothermal	TC	78% in 120 min	Catalyst = 0.05 g L ⁻¹ PMS = 1 mM TC = 20 mg L ⁻¹	SO ₄ ^{•-} , •OH, O ₂ ^{•-} and ¹ O ₂ were generated while •OH and ¹ O ₂ dominated TC oxidation	[55]

(continued on next page)

Table 2 (continued)

Sample	Synthesis method	Contaminant	Removal Efficiency	Conditions	Mechanism	Reference
MoS ₂ decorated hollow carbon microtubes	Hydrothermal	PFOA	79.6% in 6 h	Catalyst = 0.5 g L ⁻¹ PMS = 8.14 mM PFOA = 50 mg L ⁻¹	SO ₄ [•] , •OH, and ¹ O ₂ were generated while SO ₄ [•] dominated PFOA oxidation	[135]
MoS ₂ /CuS	Hydrothermal	Ni-EDTA	97.5% in 40 min	Catalyst = 2 g L ⁻¹ PMS = 48 mM Ni-EDTA = 50 mg L ⁻¹	SO ₄ [•] and •OH accounted for Ni-EDTA oxidation	[142]
Fe _{0.36} Mo _{0.64} S ₂	Biomolecule-assisted hydrothermal	Aniline	100% in 20 min	Catalyst = 0.1 g L ⁻¹ PDS = 1 mM Aniline = 10 μM	SO ₄ [•] and •OH were generated while SO ₄ [•] dominated aniline oxidation	[139]
Fe-MoS ₂	Hydrothermal followed by wet chemical	2,4-D	99% in 20 min	Catalyst = 0.2 g L ⁻¹ PDS = 0.5 mM 2,4-D = 0.1 mM	SO ₄ [•] , •OH, O ₂ [•] and ¹ O ₂ were generated while SO ₄ [•] and ¹ O ₂ dominated 2,4-D oxidation	[52]
Fe@MoS ₂	Chemical vapor transport	ATZ	100% in 10 min	Catalyst = 0.1 g L ⁻¹ PMS = 0.5 mM ATZ = 40 μM	SO ₄ [•] and •OH accounted for ATZ oxidation	[138]
FeOOH@MoS ₂	Hydrothermal	TC	85% in 30 min	Catalyst = 0.4 g L ⁻¹ PMS = 0.35 mM TC = 50 mg L ⁻¹	SO ₄ [•] and •OH were generated while •OH dominated TC oxidation	[136]
Fe ₃ O ₄ @MoS ₂	Hydrothermal	SA	99.83% in 5 min	Catalyst = 0.4 g L ⁻¹ PMS = 1 mM SA = 0.116 mM	SO ₄ [•] and ¹ O ₂ accounted for SA oxidation	[53]
Goethite-MoS ₂	Two-step hydrothermal	TC	79.6% in 30 min	Catalyst = 0.05 g L ⁻¹ PMS = 1 mM TC = 30 mg L ⁻¹	SO ₄ [•] , •OH, and ¹ O ₂ were generated while •OH and ¹ O ₂ dominated TC oxidation	[140]
Carbon intercalated Fe-doped MoS ₂	Hydrothermal	SMX	100% in 6 min	Catalyst = 0.05 g L ⁻¹ PMS = 0.25 mM SMX = 10 μM	SO ₄ [•] and •OH accounted for SMX oxidation	[54]
N-doped carbon intercalated Fe-doped MoS ₂	Hydrothermal	TC	90% in 30 min	Catalyst = 0.2 g L ⁻¹ PMS = 2 mM TC = 50 mg L ⁻¹	¹ O ₂ and surface-bound radical accounted for TC oxidation	[146]
N @ Fe _x O _y @MoS ₂	Cross-linking followed by pyrolysis	Norfloxacin (NX)	100% in 25 min	Catalyst = 0.01 g L ⁻¹ PMS = 0.325 mM NX = 30 mg L ⁻¹	SO ₄ [•] , •OH, O ₂ [•] and ¹ O ₂ were generated while ¹ O ₂ dominated NX oxidation	[137]
Fe ₃ O ₄ and MoS ₂ modified spongy wood	Two-step hydrothermal	TC	100% in 120 min	Catalyst = 0.6 g L ⁻¹ PDS = 7.6 mM TC = 20 mg L ⁻¹	Free radicals and nonradical species accounted for TC oxidation	[147]
α-FeOOH@MoS ₂ /rGO	In situ hydrothermal	RhB	99.9% in 20 min	Catalyst = 0.2 g L ⁻¹ PMS = 2 mM RhB = 20 mg L ⁻¹	SO ₄ [•] , O ₂ [•] and ¹ O ₂ accounted for RhB oxidation	[149]
3D-MoS ₂ / FeCo ₂ O ₄ GO sponge	Impregnation pyrolysis	RhB	100% in 10 min	Catalyst = one piece PMS = 0.15 mM RhB = 20 mg L ⁻¹	SO ₄ [•] , •OH, and ¹ O ₂ were generated while ¹ O ₂ dominated RhB oxidation	[150]
MoS ₂ /CoFe ₂ O ₄	Hydrothermal	TC	93.5% in 30 min	Catalyst = 0.2 g L ⁻¹ PDS = 0.5 mM TC = 10 mg L ⁻¹	SO ₄ [•] , •OH, O ₂ [•] and ¹ O ₂ were generated while ¹ O ₂ dominated TC oxidation	[141]
Co/3D-MoS ₂ graphene sponge	Impregnation pyrolysis	RhB	100% in 2 min	Catalyst = one piece PMS = 0.15 mM RhB = 20 mg L ⁻¹	SO ₄ [•] and ¹ O ₂ accounted for RhB oxidation	[148]
MoS ₂ /CuFe ₂ O ₄	Hydrothermal	Fluoxetine	97.7% in 20 min	Catalyst = 0.1 g L ⁻¹ PMS = 1 mM Fluoxetine = 20 mg L ⁻¹	SO ₄ [•] and •OH were generated while •OH dominated fluoxetine oxidation	[102]
MoS ₂ /ZnFe ₂ O ₄	Hydrothermal	TC	~75% in 30 min	Catalyst = 0.2 g L ⁻¹ PMS = 1.5 mM TC = 30 mg L ⁻¹	Not investigated	[143]

(continued on next page)

Table 2 (continued)

Sample	Synthesis method	Contaminant	Removal Efficiency	Conditions	Mechanism	Reference
SrFeO ₃ @MoS ₂	Sol-gel followed by hydrothermal	Levofloxacin (LVF)	96.06% in 20 min	Catalyst = 0.2 g L ⁻¹ PMS = 0.81 mM LVF = 10 mg L ⁻¹	SO ₄ ^{•-} , •OH, and ¹ O ₂ were generated while SO ₄ ^{•-} and •OH dominated LVF oxidation	[144]
SrCoO ₃ /MnFe ₂ O ₄ /MoS ₂	Co-precipitation followed by hydrothermal	LVF	82% in 20 min	Catalyst = 0.1 g L ⁻¹ PMS = 0.81 mM LVF = 10 mg L ⁻¹	SO ₄ ^{•-} , •OH, and ¹ O ₂ were generated while SO ₄ ^{•-} and •OH dominated LVF oxidation	[175]

persulfate activation [53,57,102]. For instance, Liu et al. found that the 2 H-MoS₂ NFs/PMS system could only remove less than 20% phenol within 180 min [57]. In contrast, the bulk MoS₂ has been demonstrated to be efficient for persulfate activation though its catalytic activity is lower than 1 T-MoS₂ [47,49,51,97,128,129]. For example, Du et al. reported that bulk MoS₂ attained a phenol removal efficiency of 80% within 25 min via activating PMS [128]. Apparently, the bulk MoS₂ in

this work possesses higher catalytic activity for PMS than the aforementioned 2 H-MoS₂ NFs synthesized by Liu et al. (the operation parameters including catalyst dosage, PMS concentration and initial phenol concentration are quite similar in the two studies). One possible reason for the higher persulfate activation efficiency of bulk MoS₂ than the 2 H-MoS₂ nanomaterials is that 1 T-2 H heterojunctions are present in the bulk MoS₂ despite of the low content of 1 T phase while the

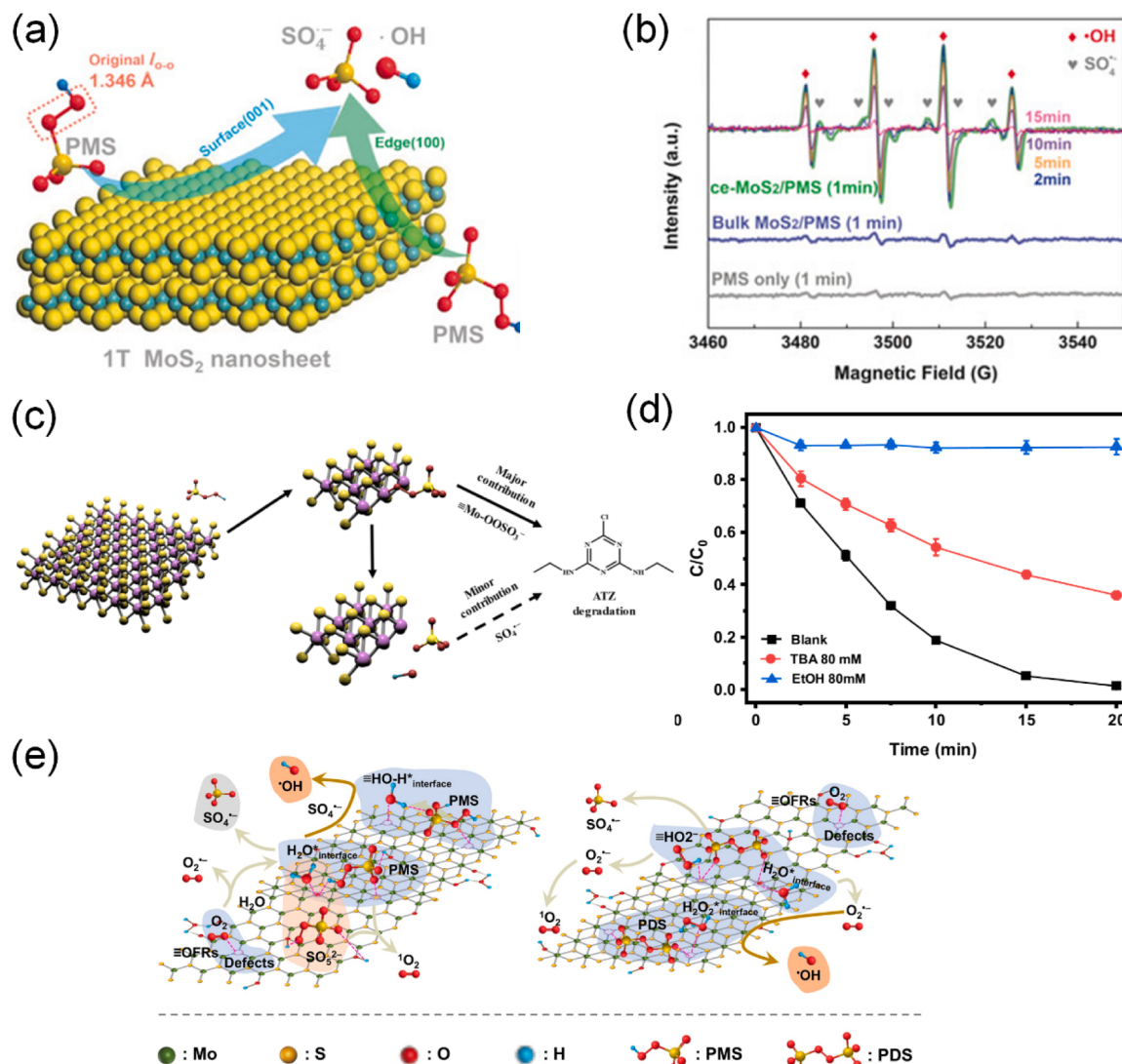


Fig. 11. (a) Schematic illustration of free radical-based activation pathway over 1 T-MoS₂ nanosheets. (b) EPR spectra showing the detection of SO₄^{•-} and •OH in 1 T-MoS₂/PMS system. (c) Schematic illustration of nonradical activation pathway based on surface Mo-OOSO₃ complex over bulk 2 H-MoS₂. (d) Influence of the presence of TBA and EtOH as radical scavengers on removal of ATZ in bulk 2 H-MoS₂/PMS system. (e) Schematic illustration of radical and nonradical co-existed activation pathways over bulk 2 H-MoS₂.

(a-b) Reproduced with permission from ref. [48]. Copyright 2019, Wiley-VCH Verlag GmbH & Co. KGaA, Weinheim. (c-d) Reproduced with permission from ref. [129]. Copyright 2022, American Chemical Society. (e) Reproduced with permission from ref. [51]. Copyright 2021, Elsevier.

heterojunctions are absent in 2 H-MoS₂ nanomaterials. As mentioned earlier, the 1 T-2 H heterojunction possesses active sites and good electrical conductivity, which significantly enhance the catalytic activity of bulk MoS₂ in persulfate activation. Yang et al. also pointed out that the 1 T phase in bulk MoS₂ dominates the intrinsic electric conductivity and favors the charge transport between PMS/PDS and MoS₂ based on the integrated computational and experimental results [51].

Although edges are not the active sites in 2 H-MoS₂ for persulfate activation, sulfur vacancies possess good catalytic activity in activating persulfate. According to the literature, the sulfur vacancies serve as the n-type dopants in 2 H-MoS₂, resulting in the increase of density of state of Fermi level [38]. Thereby, with the presence of sulfur vacancies, the charge transfer in 2 H-MoS₂ is facilitated, promoting the catalytic activation of persulfate. For instance, Li et al. conducted a ball milling treatment on bulk MoS₂ to increase the amount of sulfur vacancies and found that the ball-milled MoS₂ exhibited remarkably higher removal efficiency of TC via activating PMS [97]. Of a particular note, it is found that the sulfur vacancies play a critical role in the production of ¹O₂ from PMS activation.

3.1.2.2. Comparison of persulfate activation mechanism over 1 T-MoS₂ and 2 H-MoS₂. The persulfate activation mechanism over 2 H-MoS₂ especially bulk material is also different from that over 1 T-MoS₂ (Fig. 11). The persulfate activation over 1 T-MoS₂ mainly produces free radicals as described in Eqs. (5)-(10), while both radical-based and nonradical oxidation pathway are induced from the bulk MoS₂/persulfate system (Table 2). This suggests that the interactions between persulfate and bulk MoS₂ are more complicated than those described in Eqs. (5)-(10). First of all, it can be seen from Table 2 that the PMS and PDS activation pathways over the same bulk MoS₂ are distinct. This is attributed to the distinct molecular structures and physicochemical properties of PMS and PDS [130]. The different activation mechanisms between PMS and PDS over other types of heterogeneous catalysts (e.g., metallic oxides, carbocatalysts) have also been observed [130,131]. Moreover, the PMS/PDS activation pathway over bulk MoS₂ in different studies was also distinct.

For a heterogeneous persulfate activation system, the adsorption of persulfate molecules onto a catalyst is the first crucial step. In the MoS₂/persulfate system, the adsorption of persulfate molecules onto MoS₂ induces the formation of a transient MoS₂-persulfate complex. For 1 T-MoS₂, due to its excellent electrical conductivity, the transient complex would be quickly evolved into free radicals via the efficient electron transfer between 1 T-MoS₂ and adsorbed persulfate, which makes free radicals as the primary ROS responsible for organic pollutant oxidation (Fig. 11a). For instance, generation of •OH and SO₄^{•-} from 1 T-MoS₂/PMS system was verified by the electron paramagnetic resonance (EPR) analysis via using 5,5-dimethyl-1-pyrroline N-oxide (DMPO) as the spin trapping agent in Chen's work (Fig. 11b) [48]. DMPO can react with free radicals (•OH, SO₄^{•-} and O₂^{•-}) to form the sustained spin adducts (DMPO-•OH, DMPO-SO₄^{•-} and DMPO-•OOH, respectively) which are able to be monitored by EPR [132,133]. In addition, EPR is also employed to examine the generation of ¹O₂ from persulfate activation by using 2,2,6,6-Tetramethyl-4-piperidone (TEMP) as the spin trapping agent because TEMP can react with ¹O₂ to form a stable TEMP-¹O₂ adduct [8]. However, in the case of bulk MoS₂ as a semiconducting material with lower electrical conductivity, the electron transfer between the catalyst and adsorbed persulfate mainly relies on the 1 T-2 H heterojunction and the transient complex would not be quickly evolved into free radicals. Instead, the complex might be able to directly oxidize organic pollutants depending on the property of the organics. Sun et al. discovered that the surface ≡Mo-OOSO₃ complex was the principal ROS for the degradation of atrazine (ATZ) in a bulk MoS₂/PMS system and this complex evolved SO₄^{•-} as the secondary ROS (Fig. 11 c) [129]. The evolved SO₄^{•-} can be further transformed into •OH via hydrolysis or the reactions at the catalyst/solution interface. Especially, the ≡Mo-OOSO₃

complex shows a different target-dependent reactivity from the free radicals and other nonradical species like ¹O₂ and carbon/persulfate complexes because it oxidizes organics via the oxygen-atom-transfer pathway. Notably, Sun's work revealed that the addition of ethanol (EtOH) as a typical scavenger of both SO₄^{•-} and •OH and tert-butanol (TBA) as a typical scavenger of •OH [134] could also significantly suppress the ATZ degradation by surface ≡Mo-OOSO₃ complex (Fig. 11d), which is very likely to cause the misinterpretation that free radicals are primary ROS for organic pollutant oxidation. Therefore, it should be prudent to discriminate the contribution between surface complex and free radicals to organic pollutant oxidation in bulk MoS₂/persulfate system.

Apart from surface complexes and free radicals, O₂^{•-} and ¹O₂ can also be generated from the bulk MoS₂/persulfate system (Fig. 11e). Unfortunately, the evolution processes of O₂^{•-} and ¹O₂ in PS-AOPs systems are not clearly understood. The production of O₂^{•-} and ¹O₂ from persulfate activation over bulk MoS₂ are attributed to several possible reasons: (i) the surface MoS₂-persulfate complex is evolved into ¹O₂ through a cascade of reactions; (ii) the persulfate self-decomposition could generate ¹O₂ and the catalyst accelerates the self-decomposition and production of ¹O₂ [51]; (iii) the interactions among surface defects of bulk MoS₂ (e.g., sulfur vacancies), persulfate and dissolved oxygen induces the generation of O₂^{•-} while O₂^{•-} is further converted into ¹O₂ through the surface reactions on the catalyst or O₂^{•-} reacts with •OH to evolve ¹O₂. As it is well known, SO₄^{•-}, •OH, O₂^{•-} and ¹O₂ possess different oxidation potential and selectivity towards organic compounds. Therefore, their contributions to the oxidation of different pollutants by bulk MoS₂/persulfate system are disparate. For instance, Yang et al. found that SO₄^{•-}, •OH and ¹O₂ were generated in bulk MoS₂/PMS system according to the EPR spectra. However, the results of quenching tests using scavengers including EtOH, TBA and L-histidine which is a common scavenger of ¹O₂ [51], and background solvent exchange (replacing H₂O with D₂O) experiments indicated that •OH and SO₄^{•-} dominated butyl paraben (BPB) oxidation [51]. Another work demonstrated that SO₄^{•-}, •OH and ¹O₂ were produced from PMS activation and they all contributed to the oxidation of TC [97]. Additionally, the variation in chemical composition (1 T, 2 H and 3 R) of commercial bulk MoS₂ from different sources [69] might also affect the persulfate activation processes, inducing distinct activation pathways.

3.1.2.3. Stability of 1 T- and 2 H-MoS₂ catalysts. Despite of the good catalytic performance of MoS₂ in PS-AOPs, it (both 1 T phase and bulk material) possesses the inherit demerit of low stability, which is detrimental to the practical application. The deactivation mechanism of MoS₂ catalyst is similar to the case that MoS₂ serves as a cocatalyst in PS-AOPs, i.e., leaching of Mo ions and suppressed redox cycle of Mo(IV)/Mo(V) or Mo(IV)/Mo(VI) [49,51,73]. Especially, the redox cycle of Mo(IV)/Mo(V) or Mo(IV)/Mo(VI) was more thermodynamically infeasible in MoS₂/persulfate system compared to the MoS₂-cocatalyzed metal ion/persulfate system. This is possibly attributed to a heavier oxidation of Mo(IV) sites in the heterogeneous MoS₂/persulfate system than the MoS₂-cocatalyzed homogeneous persulfate system. In addition, the coverage of degradation intermediates onto the surface of MoS₂ catalysts would also hinder the reduction of Mo(V)/Mo(VI) by persulfate ions, especially when the organic pollutant oxidation occurs at the surface of MoS₂, giving rise to the catalyst deactivation.

Several attempts have been made to regenerate the catalytic activity of MoS₂ towards persulfate activation. Du and co-authors reported that, through treating the bulk MoS₂ catalyst with H₂O₂ after the degradation reaction, its catalytic performance barely declined in five consecutive cycles of PMS activation and phenol degradation, while the catalytic activity of control MoS₂ catalyst without any post-treatment dramatically reduced [128]. The regeneration of bulk MoS₂ catalyst via H₂O₂ post-treatment is ascribed to the fact that the stronger reducing capacity of H₂O₂ than PMS facilitates the conversion of Mo(V)/Mo(VI) into Mo

(IV) to improve the durability of MoS₂ catalyst. In addition, Chen et al. utilized photo-induced electrons to attain the reduction of Mo(V)/Mo(VI) in the 1 T/2 H heterostructured MoS₂ catalyst through light irradiation on the catalyst [73].

3.1.2.4. Summary. To summarize, 1 T phase and sulfur vacancies in MoS₂ are catalytically active for persulfate activation while 2 H phase is catalytically inert. Therefore, 1 T-MoS₂ nanosheet and bulk MoS₂ (containing a certain content of 1 T phase and sulfur vacancies) materials are reported to be effective persulfate activators, and the efficiency of former is higher than the latter. Meanwhile, the persulfate activation mechanism over 1 T-MoS₂ nanomaterials is also different from that over bulk MoS₂. The interactions occurring between persulfate and bulk MoS₂ are more complicated than those in 1 T-MoS₂/persulfate system, and both free radicals and nonradical specie are generated. However, the chemistry of MoS₂ in both homogeneous and heterogeneous persulfate systems is still poorly understood, which requires more efforts to be devoted.

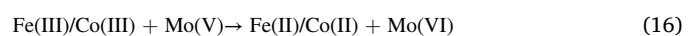
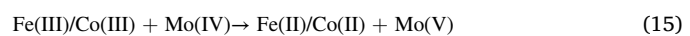
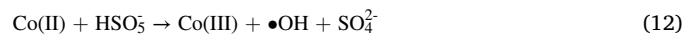
3.1.3. 2 H-MoS₂-based nanocomposites as catalysts for persulfate activation

Since 2 H-MoS₂ nanomaterials manifest poor catalytic activity towards persulfate activation, various modifications have been attempted to address this issue. Meanwhile, owing to the good stability and simple synthetic procedure of 2 H-MoS₂ nanostructures, the synthesis of modified 2 H-MoS₂-based nanomaterials can be facilely attained. In contrast, chemical modifications on 1 T-MoS₂ nanosheets are relatively difficult to conduct because of their complicated synthetic procedure. In particular, 1 T-MoS₂ is not stable and is very likely to be transformed into 2 H phase when chemical modifications are conducted. Hence, few applications of 1 T-MoS₂-based nanocomposites are reported. Currently, the modification strategies for improving catalyst activity of nanostructured 2 H-MoS₂ in PS-AOPs primarily involve phase engineering, metal doping, binarily or ternarily compositing with carbon/metal compound.

3.1.3.1. Applications of 1 T/2 H heterojunctions and 2 H-MoS₂/carbon nanocomposite catalysts in PS-AOPs. As we mentioned earlier, the catalytic activity of 2 H-MoS₂ nanomaterials is mainly limited by their low electrical conductivity which impedes charge transfer kinetics. To overcome this problem, manipulating the transformation of 2 H phase into metallic 1 T phase (i.e., fabricating 1 T/2 H heterojunctions) via phase engineering is a feasible solution. Additionally, compounding MoS₂ with conductive carbonaceous materials is also an effective strategy to improve the catalytic activity of 2 H-MoS₂ nanomaterials [55,135]. Moreover, the large specific surface area of carbonaceous materials is beneficial to the adsorption of organic pollutants and the active sites on carbonaceous materials probably also contribute to the persulfate activation, which can enhance the removal of organic pollutants. For instance, biochar-MoS₂ NFs composites were reported to exhibit higher TC and perfluorooctanoic acid (PFOA) removal efficiency via activating PMS compared to MoS₂ and biochar counterparts (Fig. 11a-c) [55,135]. Noting that the promotion effect exerted by carbon-incorporation on persulfate activation is related to the physico-chemical properties of carbons and the chemical composition of the hybrid catalyst [55,135]. Hence, it is necessary to disclose the property-composition-reactivity relationship of MoS₂/carbon composites in order to rationally design high-performance MoS₂/carbon composites towards persulfate activation and contaminant elimination.

3.1.3.2. Applications of Fe compound/MoS₂ and Fe-doped MoS₂ nanocomposite catalysts in PS-AOPs. Another effective strategy to improve persulfate activation efficiency of 2 H-MoS₂ nanomaterial is to combine it with a metal element or metal compound. In this context, MoS₂ primarily serves as the cocatalyst to accelerate the redox cycle of metal

species because the catalytic activity of MoS₂ towards persulfate activation is lower than the metal species. Additionally, if a strong interaction occurring between MoS₂ and metallic species, the amount of active sites in MoS₂ would be increased, further boosting the catalytic activity of the composite. Moreover, the stability of composite catalyst is improved with respect to the corresponding unitary material. So far, modifications of 2 H-MoS₂ nanomaterials with CuS, Fe element and oxides have been performed and the modified MoS₂ has been widely applied in PS-AOPs for eliminating a diversity of organic pollutants [53, 102,136–144]. It can be seen from Table 2 that most of the composite catalysts are Fe-based materials because Fe is of relatively low-cost and low toxicity with regard to other metal catalysts. The heterogeneous Fe-based/MoS₂ nanocomposite catalysts offer an additional advantage of easy recovery (they are magnetic) and less secondary contamination over the homogenous Fe catalysts. Currently, a wide range of Fe-based/MoS₂ nanocomposite activators have been developed involving Fe@MoS₂ single-atom catalysts (SACs), FeOOH@MoS₂, Fe_xO_y@MoS₂, CoFe₂O₄/MoS₂, CuFe₂O₄/MoS₂, ZnFe₂O₄/MoS₂ and SrFeO₃/MoS₂. Taking PMS activation over CoFe₂O₄/MoS₂ as an example, the involved catalytic mechanism is briefly described in Eqs. 11–16:



For the iron oxide@MoS₂ nanocomposites, chemical bonds between MoS₂ and iron oxide like Mo-O-Fe and Mo-S-Fe can be formed, which is conducive to charge transfer between MoS₂ and Fe active sites. Additionally, the 2D planar structure of MoS₂ can also reduce the agglomeration of iron oxide particles in the nanocomposite, increasing the exposure of Fe active sites. Meanwhile, the amount of sulfur vacancies in the composite catalyst is observed to be higher than that in the pure MoS₂. The above factors also contribute to the enhanced catalytic activity of composite catalyst towards persulfate activation. It should be noted that the molar ratio of Mo to Fe (n(Mo/Fe)) in iron oxide@MoS₂ nanocomposite catalyst has a remarkable influence on persulfate activation efficiency. Apparently, with the excessive loading of an iron oxide on MoS₂, the exposure of Mo(IV) would diminish and thus deteriorate the Fe(III)/Fe(II) redox cycle. Several studies reported that the catalytic activity of geothite-MoS₂, Fe₃O₄@MoS₂ and CoFe₂O₄@MoS₂ increased with the n(Mo/Fe) and a linear correlation between n(Mo/Fe) and organic pollutant degradation kinetic rates was derived when the value of n(Mo/Fe) was within a certain range (Fig. 12d-i) [53,140,141]. This suggests that the cocatalytic effect of MoS₂ plays a key role in promoting the catalytic activity of iron oxide@MoS₂ nanocomposite. However, whether a further increase of n(Mo/Fe) would promote the catalytic activity of iron oxide@MoS₂ is unclear and further investigation is of necessity to find the optimal n(Mo/Fe) for obtaining high-performance iron oxide@MoS₂ nanocomposite catalyst for PS-AOPs.

As for Fe@MoS₂ SACs, stronger metal-support interactions occur between Fe single atomic sites and MoS₂ substrate compared to those in iron oxide@MoS₂ nanocomposites, which even can activate the inert basal plane of 2 H-MoS₂ and dramatically elevate its inherent catalytic activity [145]. When Fe atoms are incorporated into the MoS₂ lattice, they can exist in three configurations: (i) Fe atoms substitute Mo atoms in basal plane (Fig. 13a); (ii) Fe atoms are bonded as adatoms on the top of S atoms (Fe₁-MoS₂, Fig. 13b); (iii) Fe atoms are anchored to the edge Mo vacancies when MoS₂ is defect-rich to form Fe-S-Mo interfacial sites (Fig. 13c). DFT calculations demonstrate the occurrence of a large amount of charge transfer between the foreign Fe atoms and MoS₂

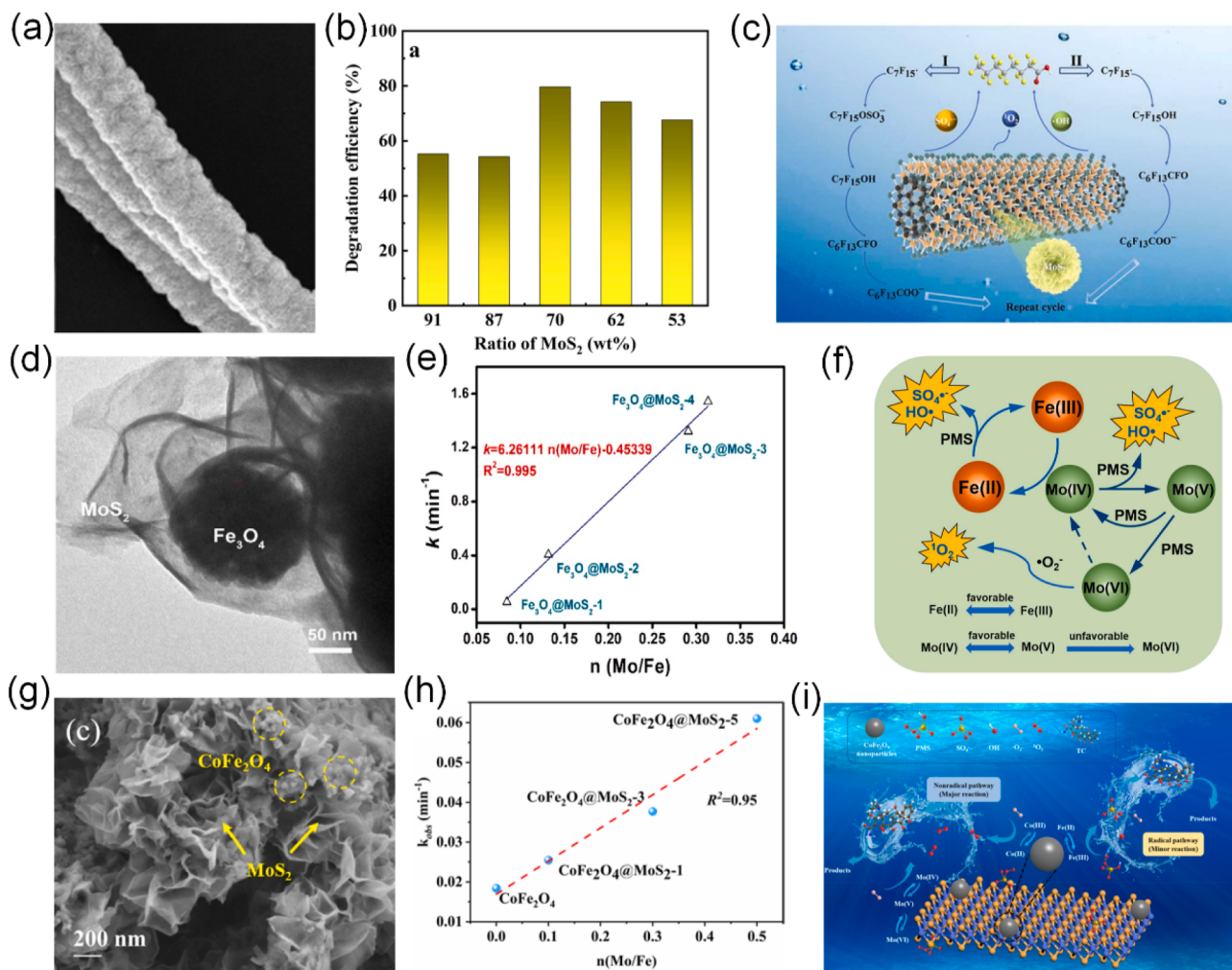


Fig. 12. (a) SEM image of MoS₂/hollow carbon microtube composite. (b) Effect of MoS₂ content in a MoS₂/hollow carbon microtube composite on PFOA removal. (c) Proposed mechanism of PFOA degradation in the MoS₂/hollow carbon microtube composite/PMS system. (d) HRTEM image of Fe₃O₄ @MoS₂. (e) The relationship between n(Mo/Fe) and kinetic rates k of different Fe₃O₄ @MoS₂ composites. (f) Activation mechanism of a Fe₃O₄ @MoS₂/PMS system. (g) HRTEM image of CoFe₂O₄ @MoS₂. (h) The relationship between n(Mo/Fe) and kinetic rates k_{obs} of different CoFe₂O₄ @MoS₂ composites. (i) Activation mechanism of a CoFe₂O₄ @MoS₂/PMS system.

(a-c) Reproduced with permission from ref. [135]. Copyright 2022, Elsevier. (d-f) Reproduced with permission from ref. [53]. Copyright 2021, Elsevier. (g-i) Reproduced with permission from ref. [141]. Copyright 2022, Elsevier.

monolayer in the above three cases (Fig. 13 a-c), which not only favors the catalytic reactions but also helps hinder the aggregation of single Fe atoms [139].

Notably, the catalytic activity of the above three types of Fe@MoS₂ SACs varies with the bonding configuration of Fe atomic sites. The doped Fe atom in defective MoS₂ can gain more charge from the support (i.e., from two Mo atoms and the four neighboring S atoms to Fe) compared to the cases of Fe@defect-free MoS₂, thus further accelerating the Fe³⁺/Fe²⁺ redox cycle during persulfate activation process [52]. Regarding the Fe@MoS₂ with substitutional Fe doping in the basal plane, the changes of free energies after PMS adsorption onto two different Mo sites in the basal plane (one is adjacent to Fe atom and the other is away from Fe atom) were both calculated to be larger than that for pristine MoS₂, and the O-O bond length of PMS adsorbed onto the two sites was remarkably enlarged with respect to free PMS [138]. These results implied that Fe doping not only leads to the enhanced adsorption of PMS onto the basal plane but also turns the inert basal plane of pristine MoS₂ into an active site for persulfate activation [52,138,139]. Interestingly, in comparison to the Fe@MoS₂ with substitutional Fe doping in the basal plane, the Fe@MoS₂ catalyst containing Fe-S-Mo edge sites shows better stability and induces different PMS activation

pathways (Fig. 13 d-h). This suggests that engineering the defective structure of a MoS₂ support is a feasible method to tune the catalytic activity of metal@MoS₂ SACs and persulfate activation pathway.

3.1.3.3. Applications of ternary carbon/Fe-based/MoS₂ nanocomposite catalysts in PS-AOPs. To further improve the catalytic activity of a Fe-based/MoS₂ composite, integrating it with a carbonaceous material to fabricate a ternary compound can be a potential solution because the introduction of a carbon support can further promote the electron transfer and increase the exposure of adsorption/active sites in the hybrid catalyst by reducing the agglomeration of Fe-based material and MoS₂. In addition, the incorporation of carbon support is able to alleviate metal ion leaching and thus elevate catalyst stability. Carbon/N-doped carbon intercalated Fe-doped MoS₂ nanosheets [54,146], foam-sponge construction wood supported Fe₃O₄ @MoS₂ [147], N-doped Fe_xO_y @MoS₂ (N @ Fe_xO_y @MoS₂) carbonaceous beads [137], graphene oxide-supported 3D-MoS₂/FeCo₂O₄ and 3D-MoS₂/Co sponges [148–150] have been fabricated to activate persulfate for removing organic pollutants. These catalysts manifested better removal performance of antibiotics and stability than their corresponding binary counterparts.

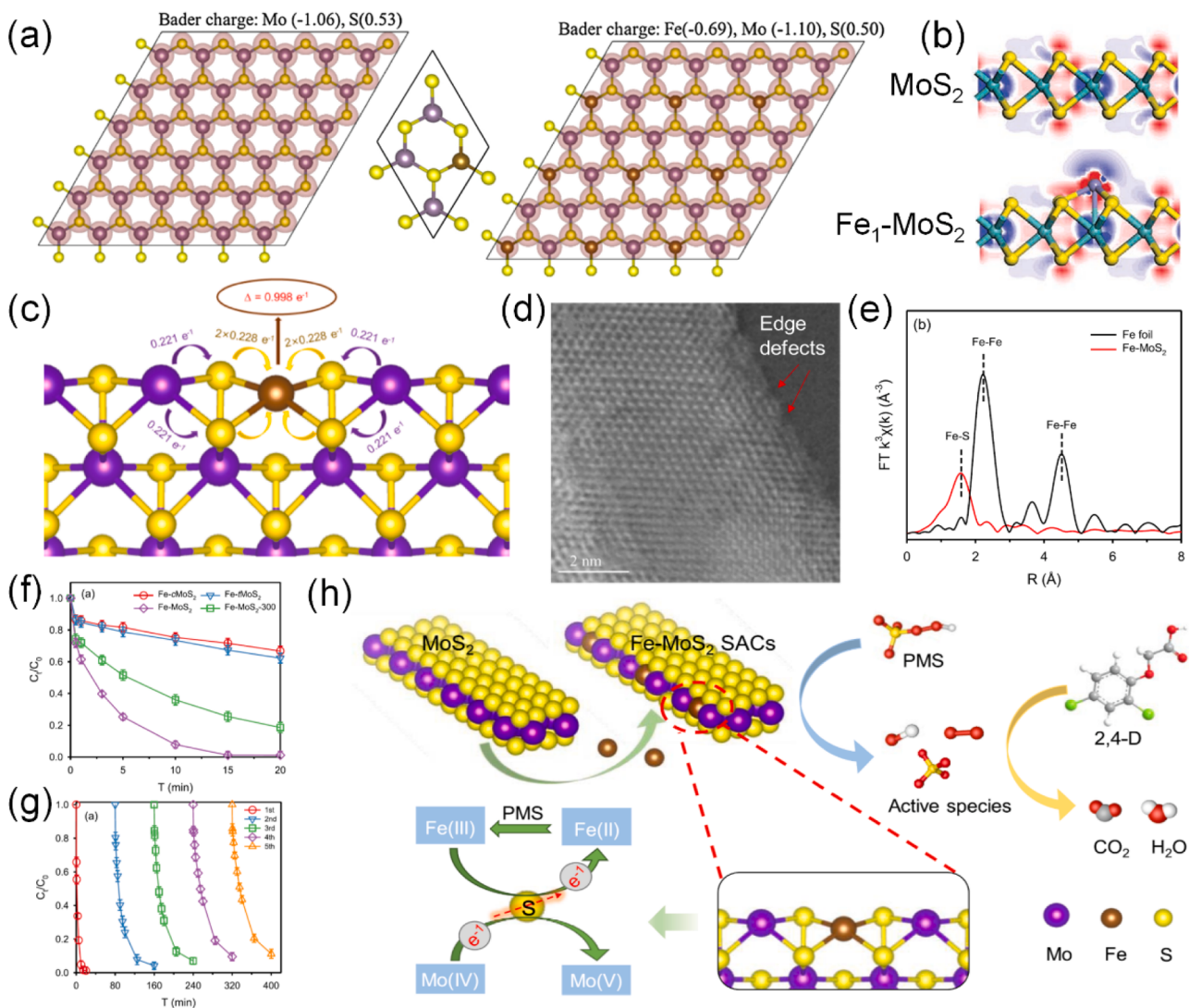


Fig. 13. (a) Charge density and Bader charge transfer of atoms in pristine MoS_2 and $\text{Fe}_{0.36}\text{Mo}_{0.64}\text{S}_2$ SAC. Purple, yellow, and bronze balls are Mo, S and Fe atoms, respectively. (b) Deformation charge densities in pristine MoS_2 and $\text{Fe}_1\text{-MoS}_2$ from the side view. Cyan, yellow and purple balls are Mo, S and Fe atoms, respectively. (c) DFT simulated charge distributions and schematic edge structures of the $\text{Fe}\text{-MoS}_2$ catalyst. Purple, yellow and brown balls are Mo, S and Fe atoms, respectively. (d) High angle annular dark field-scanning TEM (HAADF-STEM) image of $\text{Fe}\text{-MoS}_2$. (e) Fourier transform extended X-ray absorption fine structure spectra of $\text{Fe}\text{-MoS}_2$ and Fe foil. (f) Effects of $\text{Fe}\text{-MoS}_2$ featuring different edge defect structures on the removal efficiency of 2,4-D. (g) Reusability experiments of $\text{Fe}\text{-MoS}_2$. (h) Schematic illustration of degradation mechanism of 2,4-D in the $\text{Fe}\text{-MoS}_2/\text{PMS}$ system.

(a) Reproduced with permission from ref. [139]. Copyright 2020, Elsevier. (b) Reproduced with permission from ref. [58]. Copyright 2021, Wiley-VCH Verlag GmbH & Co. KGaA, Weinheim. (c-h) Reproduced with permission from ref. [52] [52]. Copyright 2022, Elsevier.

Interestingly, in the case of carbon-intercalated Fe-doped MoS_2 nanosheets ($\text{C-MoS}_2 @\text{Fe}$), the carbon intercalation even affects the phase composition of MoS_2 substrate [54]. Wu et al. added ascorbic acid into the precursor solution of MoS_2 and Fe to prepare $\text{C-MoS}_2 @\text{Fe}$ via a facile one-step hydrothermal method. It was found that the contents of 1 T- MoS_2 and sulfur vacancies in $\text{C-MoS}_2 @\text{Fe}$ were significantly increased than the control sample of $\text{MoS}_2 @\text{Fe}$. As mentioned earlier, the presence of 1 T phase and sulfur vacancies can significantly improve the catalytic/co-catalytic activity of 2 H- MoS_2 . Accordingly, the $\text{C-MoS}_2 @\text{Fe}$ achieved 100% removal of SMX within 6 min via activating PMS and the corresponding modified kinetics model value was much higher than many reported metallic catalysts [54]. Moreover, a removal rate of chemical oxygen demand at 79.6% within 8 h was attained by $\text{C-MoS}_2 @\text{Fe}$ when it was used to treat actual industrial wastewater, implying its great application prospect.

3.1.3.4. Persulfate activation mechanism over 2 H- MoS_2 -based nanostructured catalyst. Regarding the persulfate activation mechanism over 2 H- MoS_2 -based nanocomposites, both radical and nonradical oxidation pathways can occur. In the case of carbon/ MoS_2 nanocomposite, free radicals, O_2^\bullet and ${}^1\text{O}_2$ are observed to be produced from persulfate activation. The production of O_2^\bullet and ${}^1\text{O}_2$ possibly originates from the interaction between the active sites on carbon material and persulfate [151]. For the Fe-doped MoS_2 nanosheets, the persulfate activation processes are similar to those in the MoS_2 -cocatalyzed Fe^{2+} /persulfate systems and the generated ROS are typically free radicals. Notably, when a considerable amount of sulfur vacancies is present in Fe-doped MoS_2 , O_2^\bullet and ${}^1\text{O}_2$ could also be produced from persulfate activation. In the case of iron oxide/ MoS_2 and ternary carbon/iron oxide/ MoS_2 composites, free radicals, O_2^\bullet and ${}^1\text{O}_2$ co-exist in the persulfate system. This is because multiple active sites (e.g., Fe species, oxygen/sulfur vacancies, lattice oxygens, oxygenated group, and carbon defects) are present in the composite catalyst, and the reactions between those active

sites and persulfate can result in the formation of different types of ROS.

Overall, various modification strategies can be utilized to improve the persulfate activation efficiency of 2 H-MoS₂ nanomaterial including phase engineering, carbon compositing, Fe doping, metal compound compositing, Fe oxide/Fe and carbon compositing (Fig. 14). In comparison to the modification with a carbonaceous material, Fe doping and combination with a metal compound are more efficient because the metal species are active sites for persulfate activation and MoS₂ serves as the cocatalyst to regenerate the active sites. Meanwhile, the catalytic performance of a ternary composite containing Fe oxide/Fe, carbon and MoS₂ is superior to that of binary MoS₂ composite though the synthetic procedure of the former is probably more complex than the latter. On one side, the number of active sites and electron transport in the ternary compound are increased compared to the binary composite. On the other side, the carbon incorporation can diminish the leaching of metal ions, which is conducive to avoiding the risk of secondary pollution. Especially, through proper phase engineering and defect engineering strategies to optimize the phase composition and defective structure of ternary MoS₂ composite, a high-performance persulfate activator can be obtained for practical water treatment.

3.1.4. Summary

Owing to the presence of reducing Mo(IV) sites, MoS₂ shows good cocatalytic activity and catalytic activity towards persulfate activation. For MoS₂ cocatalyst, the current studies concentrated on bulk and nanostructured 2 H phase, and the nanostructured material is superior to the bulk counterpart arising from the more exposure of active sites. For MoS₂ catalyst, 1 T phase outperforms 2 H phase, and the bulk 2 H-MoS₂ is superior to nanostructured 2 H-MoS₂. Fortunately, various modification strategies have been developed to improve the persulfate activation efficiency of 2 H-MoS₂ nanomaterial, and the resulted 2 H-MoS₂-based nanocomposite serves as both catalyst and cocatalyst in PS-AOPs. Nevertheless, due to the encumbered reduction of Mo(VI) to Mo(IV) during persulfate activation process, the stability of MoS₂ cocatalyst/catalyst is not good, which needs further amelioration.

3.2. 2 H-MoS₂-based nanomaterials as photocatalysts for persulfate activation

3.2.1. Principle of photocatalysis

For the semiconducting 2 H MoS₂ polytype, light irradiation is an efficient physical approach to improve the amount of free charge carriers for participating in chemical reactions. Upon light irradiation, a semiconductor photocatalyst can absorb photons and the surface electrons at the valence band (VB) of the photocatalyst are excited to the conduction band (CB), creating positively charged holes (h⁺) in the VB

[28,152–154]. Depending on the positions of band-edge of the photocatalyst, the photogenerated electrons (e[−]) and h⁺ possess different redox potentials and can take part in different redox reactions. According to the literature, the photo-induced e[−] and h⁺ on the photocatalyst are able to effectively decompose persulfate to generate ROS for attacking organic compounds [155]. Therefore, light-driven PS-AOPs with heterogeneous photocatalysts especially visible light-responsive photocatalysts has attracted a lot of attention from researchers [155–158].

3.2.2. Photocatalytic activity of 2 H-MoS₂ and modification strategies for nanostructured 2 H-MoS₂ photocatalyst

As described in Section 2, the electronic and optical properties of 2 H-MoS₂ vary with the layer number and the nanostructured MoS₂ semiconductor has superior properties to the bulk material. Fig. 15a depicts the band positions of bulk, multilayer and monolayer 2 H-MoS₂ as well as another two popular photocatalysts (TiO₂ and g-C₃N₄) for comparison. Among them, the suitable bandgap and edge potentials of multilayer and monolayer MoS₂ endow them both high light absorption efficiency and good ability to generate ROS through photocatalysis. These leads monolayer, few-layer and other nanostructured 2 H-MoS₂ (e.g., holey MoS₂ nanosheets, MoS₂ quantum dots (QDs)) with more accessible active sites to be desirable visible light-responsive photocatalysts [25,28,159,160]. In addition, modifications on 2 H-MoS₂ nanomaterial have been conducted to improve its photocatalytic activity towards persulfate activation and the pollutant degradation efficiency.

Similar to the case of 2 H-MoS₂ as a chemical catalyst for persulfate activation (Section 3.1.3), incorporation with the conductor and doping with a metal element are also common approaches to boost the photocatalytic activity of nanostructured 2 H-MoS₂ because they can improve the charge carrier mobility and separation efficiency of photo-induced e[−]/h⁺ pairs of photocatalysts [60,155]. Besides, coupling with other semiconductors to form nanoheterojunction is also an efficient approach to elevate the photocatalytic activity of nanostructured 2 H-MoS₂ due to the reduced electron-hole recombination rate [28,161,162]. Especially, the combination with the semiconductor possessing suitable VB edge potential to trigger the H₂O•OH redox reaction can improve the yield of ROS during the photocatalytic persulfate activation process since the VB edge potential of nanostructured 2 H-MoS₂ is lower than the potential of H₂O•OH reaction [63]. Up to date, a wide range of MoS₂-based photocatalysts including 2 H/1 T MoS₂ nanoheterostructure, Co/Cu-doped MoS₂ NFs, binary composites (e.g., C/MoS₂, BiOBr/MoS₂, MOF/MoS₂) and ternary composites (e.g., WO₃ @MoS₂/Ag, gCN/Cu-Fe₂O₄/MoS₂) have been developed for photocatalytic and photo-electrocatalytic activation of persulfate to eliminate pollutants, which are summarized in Table 3 [73,143,159,163–181].

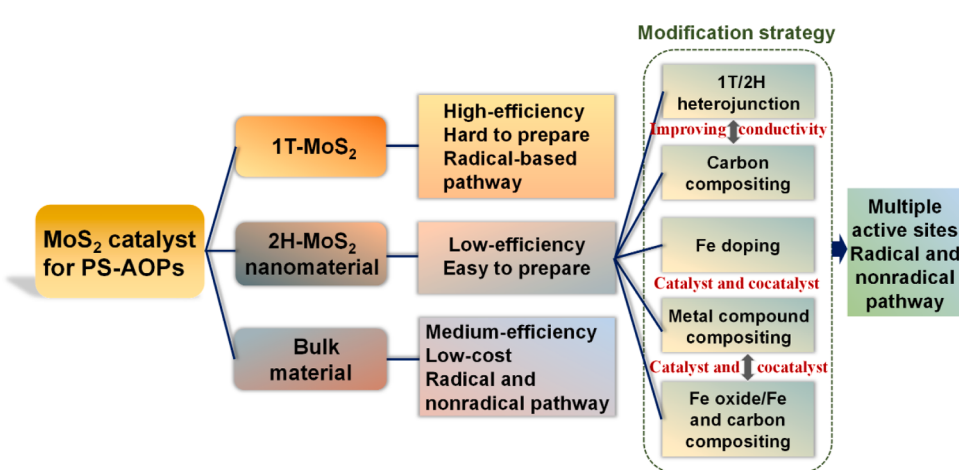


Fig. 14. Summary of MoS₂ as a catalyst for persulfate activation.

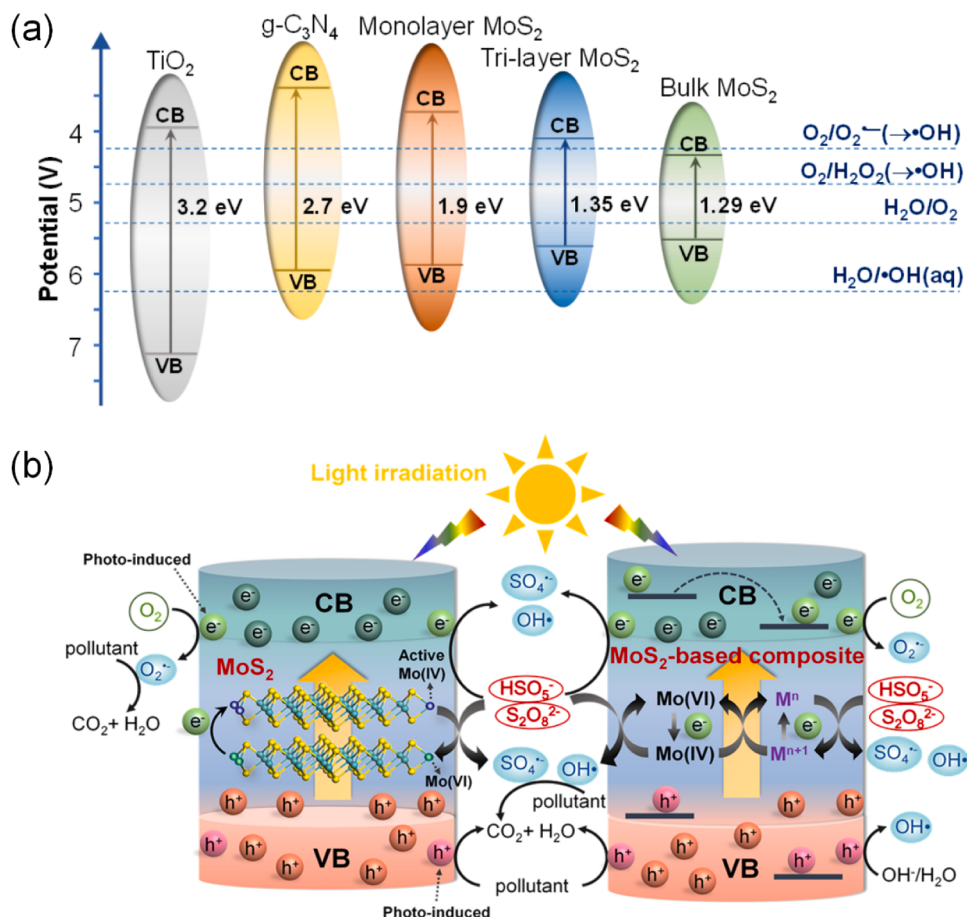


Fig. 15. (a) ROS formation potential and the band positions of monolayer, multilayer and bulk MoS₂, and two reference photocatalysts (g-C₃N₄ and TiO₂). (b) Conceptual illustration of mechanisms in a photo-activated PS-AOP system mediated by MoS₂ and MoS₂-based composite photocatalysts. (a) (Data were from ref. [25,160]).

3.2.3. Mechanism of photocatalytic activation of persulfate over 2 H-MoS₂-based nanomaterials

2 H-MoS₂-based nanomaterials play multiple roles including cocatalyst/catalyst and photocatalyst in the photocatalytic persulfate activation processes. Hence, the reactions occurring in the photo-activated PS-AOP system mediated by nanostructured 2 H-MoS₂-based photocatalyst are more complicated than those in catalytic activation process, involving (Fig. 15b): (i) the intrinsic free charges of MoS₂/MoS₂-based composite reacts with persulfate to produce ROS for oxidizing organic pollutant; (ii) the bombardment of photons can induce the decomposition of persulfate molecules and generation of ROS (UV light is more efficient for persulfate activation than the visible light) [103,105]; (iii) photo-induced e⁻ reacts with persulfate to evolve reactive species for oxidizing organic pollutant; (iv) photo-induced e⁻ reacts with oxygen molecules and photo-induced h⁺ reacts with water molecules (depending on the band alignment of composite photocatalyst) to evolve reactive species; (v) photo-induced h⁺ directly oxides the organics; (vi) photo-induced e⁻ and/or MoS₂ as the cocatalyst facilitate the regeneration of metallic active site in MoS₂/MoS₂-based composite, improving persulfate activation efficiency and reusability of the catalyst.

For example, in a 2 H/1 T MoS₂/PMS/visible light system, around 95% 2,4-dichlorophenoxyacetic acid (2,4-D) was degraded within 60 min with the optimized heterojunction photocatalyst, much higher than the 2 H/1 T MoS₂/PMS and 2 H MoS₂/PMS/visible light systems (Fig. 16a) [73]. With the help of operando solid EPR, X-ray photoelectron spectroscopy (XPS) and X-ray absorption near edge spectroscopy techniques (Fig. 16 b and c), it was revealed that the photo-generated electrons partially reduced the Mo(IV) atoms near the

1 T/2 H heterojunction into Mo(III), and Mo(III) is more efficient than Mo(IV) to initiate the decomposition of PMS along with the formation of Mo(V). Subsequently, Mo(V) was transformed into Mo(IV) through the efficient electron transfer at the heterojunction interface. Due to the continuous regeneration of Mo(III), the MoS₂-based photo-activated PMS system exhibited good stability in 2,4-D removal (Fig. 16d).

Additionally, Neogi's work reported the enhanced removal of ciprofloxacin (CIP) by photo-activated PMS system based on a dual Z-scheme gCN/CuFe₂O₄/MoS₂ photocatalyst under visible light irradiation (Fig. 16e) [169]. As mentioned in Section 3.1.3, CuFe₂O₄/MoS₂ itself was a good persulfate activator due to the synergy between catalytic activity of CuFe₂O₄ and co-catalytic activity of MoS₂. Under light illumination, the Cu²⁺ and Fe²⁺ catalytic sites on the surface of gCN/CuFe₂O₄/MoS₂ photocatalyst firstly react with PMS to produce free radicals and MoS₂ serves as the cocatalyst to accelerate Cu³⁺/Cu²⁺ and Fe³⁺/Fe²⁺ cycles, which was verified by the XPS analysis (Fig. 16 f and g). Meanwhile, a significant amount of photo-induced e⁻/h⁺ in the ternary composite react with PMS, O₂ and H₂O molecules to evolve •OH, SO₄²⁻ and O₂^{•-} due to the efficient charge carrier separation enabled by the dual Z-scheme heterojunction. Finally, the CIP molecules are attacked by the generated radicals (•OH, SO₄²⁻ and O₂^{•-}) and photo-induced h⁺ to achieve the remediation of organic pollutant. The surface bound redox cycles on CuFe₂O₄/MoS₂ involving Cu²⁺/Cu⁺, Fe³⁺/Fe²⁺ and Mo⁴⁺/Mo⁶⁺ could be accelerated by the photo-induced electrons.

Notably, in some cases the chemical modification can also improve the chemical activity of 2 H-MoS₂ towards persulfate activation due to the introduction of more active sites, while there might be a trade-off between the photocatalytic activity and the intrinsic chemical activity

Table 32 H-MoS₂-based nanomaterials as photocatalysts, photothermal agents and piezocatalysts in PS-AOPs.

Sample	Synthesis method	Contaminant	Removal Efficiency	Conditions	Mechanism	Reference
1 T/2 H MoS ₂ NFs	Hydrothermal	2,4-D	~100% in 60 min	Catalyst = 0.1 g L ⁻¹ PMS = 0.5 mM 2,4-D = 25 μM λ > 420 nm	SO ₄ ^{•-} and •OH accounted for 2,4-D oxidation	[73]
Co-doped MoS ₂	Hydrothermal	Oflloxacin (OFX)	91.1% in 30 min	Catalyst = 0.1 g L ⁻¹ PMS = 0.81 mM OFX = 20 mg L ⁻¹ λ > 420 nm	SO ₄ ^{•-} and ¹ O ₂ accounted for OFX oxidation	[168]
Cu-doped MoS ₂	Hydrothermal	CBZ	92% in 60 min	Catalyst = 0.2 g L ⁻¹ PMS = 1 mM CBZ = 10 mg L ⁻¹ λ > 400 nm	SO ₄ ^{•-} , ¹ O ₂ and h ⁺ accounted for CBZ oxidation	[180]
3D urchin-like MoS ₂ /C nanoparticles	Template-assisted hydrothermal	LVF	100% in 80 min	Catalyst = 0.1 g L ⁻¹ PMS = 1.46 mM LVF = 70 mg L ⁻¹ Ultrasonication (US) power = 70 W λ > 420 nm	SO ₄ ^{•-} and •OH accounted for LVF oxidation	[174]
BiOBr/MoS ₂	Precipitation	RhB	100% in 20 min	Catalyst = 0.5 g L ⁻¹ PMS = 1 mM RhB = 20 mg L ⁻¹ λ > 420 nm	SO ₄ ^{•-} , •OH, O ₂ ^{•-} and h ⁺ accounted for RhB oxidation	[164]
MoS ₂ /NH ₂ -MIL-101(Cr)	Hydrothermal	Indole	98.6% in 120 min	Catalyst = 1 g L ⁻¹ PDS = 10 mM Indole = 50 mg L ⁻¹ λ > 420 nm	SO ₄ ^{•-} , •OH and h ⁺ accounted for Indole oxidation	[171]
MIL-88A(Fe)/ MoS ₂	Hydrothermal	BPA	98.2% in 60 min	Catalyst = 0.1 g L ⁻¹ PMS = 0.81 mM BPA = 25 mg L ⁻¹ λ > 420 nm	SO ₄ ^{•-} , •OH, O ₂ ^{•-} and ¹ O ₂ accounted for BPA oxidation	[172]
Prussian blue @MoS ₂	Hydrothermal	BPA	95.7% in 40 min	Catalyst = 0.3 g L ⁻¹ PMS = 0.49 mM BPA = 20 mg L ⁻¹ λ < 420 nm	SO ₄ ^{•-} , •OH, O ₂ ^{•-} and h ⁺ accounted for BPA oxidation	[176]
Fe ₇ S ₈ @MoS ₂ -O core-shell	Hydrothermal	LVF	92.5% in 80 min	Catalyst = 0.4 g L ⁻¹ PMS = 1 mM LVF = 10 mg L ⁻¹ λ > 420 nm	SO ₄ ^{•-} , •OH, O ₂ ^{•-} and h ⁺ accounted for BPA oxidation	[163]
MoS ₂ -ZnFe ₂ O ₄	Hydrothermal	TC	90% in 30 min	Catalyst = 0.2 g L ⁻¹ PMS = 1.5 mM TC = 30 mg L ⁻¹ λ > 420 nm	SO ₄ ^{•-} , •OH, and O ₂ ^{•-} accounted for TC oxidation	[143]
CoFe ₂ O ₄ /MoS ₂	Hydrothermal	Chloroquine (CQ)	98.6% in 12 min	Catalyst = 0.3 g L ⁻¹ PMS = 1 mM CQ = 60 mg L ⁻¹ Simulated sunlight	SO ₄ ^{•-} , •OH, O ₂ ^{•-} , ¹ O ₂ and h ⁺ accounted for CQ oxidation	[178]
MoS ₂ /BiVO ₄	Hydrothermal	BPA	97.5% in 20 min	Catalyst = 0.2 g L ⁻¹ PMS = 0.16 mM BPA = 30 mg L ⁻¹ λ > 420 nm	SO ₄ ^{•-} , •OH, ¹ O ₂ and h ⁺ accounted for BPA oxidation	[167]
Granular MoS ₂ /rGO/BiVO ₄	Hydrothermal followed by polymerization	CBZ	79.67% in 20 min	Catalyst = 5 g L ⁻¹ PDS = 0.125 mM CBZ = 10 μM λ > 420 nm	SO ₄ ^{•-} and •OH accounted for CBZ oxidation	[165]
WO ₃ @MoS ₂ /Ag	Hydrothermal	BPA	92.51% in 140 min	Catalyst = 0.2 g L ⁻¹ PMS = 1.6 mM BPA = 10 mg L ⁻¹ λ > 420 nm	SO ₄ ^{•-} , •OH and O ₂ ^{•-} accounted for BPA oxidation	[166]
MoS ₂ /Ag/g-C ₃ N ₄	Hydrothermal followed by ultrasonication	TC	98.9% in 50 min	Catalyst = 0.8 g L ⁻¹ PMS = 0.1 mM TC = 20 mg L ⁻¹ λ > 420 nm	• OH, O ₂ ^{•-} and SO ₄ ^{•-} accounted for TC oxidation	[170]
Cu ⁰ -MoS ₂ /C ₃ N ₄ expanded graphite	Hydrothermal followed by chemical reduction	TC	99% in 60 min	Catalyst = 0.33 g L ⁻¹ PMS = 1.6 mM TC = 50 mg L ⁻¹ λ > 420 nm	SO ₄ ^{•-} , •OH, O ₂ ^{•-} and ¹ O ₂ accounted for TC oxidation	[179]
g-CN/CuFe ₂ O ₄ /MoS ₂	In-situ solid combustion followed by hydrothermal	CIP	97% in 60 min	Catalyst = 0.2 g L ⁻¹ PMS = 1.6 mM CIP = 10 mg L ⁻¹ λ > 420 nm	Surface-bound SO ₄ ^{•-} and •OH, O ₂ ^{•-} and h ⁺ accounted for CIP oxidation	[169]
SrCoO ₃ / MnFe ₂ O ₄ /MoS ₂	Co-precipitation followed by hydrothermal	LVF	95.1% in 20 min	Catalyst = 0.1 g L ⁻¹ PMS = 0.81 mM LVF = 10 mg L ⁻¹	SO ₄ ^{•-} , •OH, O ₂ ^{•-} and ¹ O ₂ were generated while SO ₄ ^{•-} and •OH dominated LVF oxidation	[175]

(continued on next page)

Table 3 (continued)

Sample	Synthesis method	Contaminant	Removal Efficiency	Conditions	Mechanism	Reference
MoS ₂ quantum dots/N-doped carbon dots/TiO ₂	Hydrothermal followed by ultrasonication	BPB	100% in 180 min	$\lambda > 420 \text{ nm}$ Catalyst = 1 g L ⁻¹ PDS = 5 mM BPB = 2.5 mg L ⁻¹ $\lambda > 400 \text{ nm}$	• OH, ¹ O ₂ and O ₂ • were generated while •OH dominated BPB oxidation	[159]
Pt@CeO ₂ @ MoS ₂	Hydrothermal	CBZ	100% in 30 min	Catalyst = 0.25 g L ⁻¹ PMS = 0.76 mM CBZ = 2 mg L ⁻¹ $\lambda > 420 \text{ nm}$ Potential = 1 V	SO ₄ ²⁻ , •OH, O ₂ • and ¹ O ₂ accounted for CBZ oxidation	[173]
MoS ₂ nanosheets (photothermal)	Hydrothermal	CBZ	81.5% in 60 min	PDS = 8.4 mM CBZ = 10 mg L ⁻¹ $\lambda = 808 \text{ nm}$	SO ₄ ²⁻ and •OH accounted for CBZ oxidation	[56]
g-C ₃ N ₄ /MoS ₂ (photothermal)	Hydrothermal followed by ultrasonication	NB	98% in 240 min	Catalyst = 10 mg PDS = 4.2 mM NB = 0.5 mg L ⁻¹ Simulated sunlight	SO ₄ ²⁻ accounted for NB oxidation	[183]
Co-MoS ₂ /CNT/ PTFE membrane (photothermal)	Hydrothermal method	RhB	~99% in 8 h	Area = 25 cm ² PDS = 5 mM RhB = 20 mg L ⁻¹ Simulated sunlight	SO ₄ ²⁻ , •OH and ¹ O ₂ accounted for RhB oxidation	[184]
MoS ₂ NFs (piezocatalyst)	Hydrothermal	Phenol	95% in 180 min	Catalyst = 0.3 g L ⁻¹ PMS = 3.25 mM Phenol = 10 mg L ⁻¹ US power = 300 W	SO ₄ ²⁻ and •OH were generated while •OH dominated phenol oxidation	[57]
MoS ₂ NFs (piezocatalyst)	Hydrothermal	Benzotriazole (BTR)	91.1% in 5 min	Catalyst = 0.5 g L ⁻¹ PMS = 0.81 mM BTR = 5 mg L ⁻¹ Water vortex	SO ₄ ²⁻ , •OH, O ₂ • and ¹ O ₂ were generated while ¹ O ₂ accounted for BTR oxidation	[196]
BaTiO ₃ /MoS ₂ (piezocatalyst)	Hydrothermal followed by physically mixing	Ornidazole (ORZ)	90.9% in 40 min	Catalyst = 0.1 g L ⁻¹ PMS = 0.41 mM ORZ = 50 mg L ⁻¹ US power = 100 W	SO ₄ ²⁻ , •OH, O ₂ • and ¹ O ₂ were generated while •OH and ¹ O ₂ accounted for ORZ oxidation	[187]
Fe ₁ -MoS ₂ (piezocatalyst)	Dipping-calcination	MTZ	96.5% in 72 s	Catalyst = 0.5 g L ⁻¹ PMS = 0.81 mM MTZ = 10 mg L ⁻¹ 10°spiral tube with 0.5 m height	SO ₄ ²⁻ , •OH, O ₂ • and ¹ O ₂ were generated while ¹ O ₂ and O ₂ • accounted for MTZ oxidation	[58]
1 T/2 H MoS ₂ + Fe ⁰ (piezocatalyst)	Hydrothermal	NB	99.8% in 80 min	Catalyst = 0.6 g L ⁻¹ PMS = 2.28 mM NB = 20 mg L ⁻¹ US power = 300 W	SO ₄ ²⁻ , O ₂ • and ¹ O ₂ accounted for NB oxidation	[201]
Co ₃ S ₄ /MoS ₂ (piezocatalyst)	Two-step hydrothermal	Phenol	99.9% in 240 min	Catalyst = 0.6 g L ⁻¹ PMS = 4.88 mM Phenol = 10 mg L ⁻¹ US power = 300 W	SO ₄ ²⁻ and •OH accounted for phenol oxidation	[200]
Helical Fe@MoS ₂ /CFC cathode (piezo-photocatalyst)	Hydrothermal	Berberine (Bb)	92.8% in 60 min	Area = 4 * 9 cm ² PMS = 0.5 mM Bb = 10 mg L ⁻¹ $\lambda > 420 \text{ nm}$	SO ₄ ²⁻ , •OH, O ₂ • and h ⁺ accounted for Bb oxidation	[202]

of modified MoS₂. For example, the chemical activity of 2 H/1 T MoS₂ towards PMS activation is linearly increased with the atomic ratio of 1 T phase in the heterostructure, but its photocatalytic activity towards PMS activation shows a volcano relationship with 1 T phase content (Fig. 16a) [73]. Therefore, further research on the structure-activity relationship of modified 2 H-MoS₂ towards persulfate activation is necessary to assist the rational design of high-performance 2 H-MoS₂-based photocatalysts for PS-AOPs.

3.3. 2 H-MoS₂-based nanomaterials as photothermal agents for persulfate activation

For the semiconducting 2 H-MoS₂ nanomaterial, its good absorbance of visible and NIR light can trigger not only a photocatalytic process but also a photothermal process wherein the light especially NIR light is directly converted into heat energy mediated by the photothermal material [182]. It is well established that thermal heating is also an effective physical approach to activate persulfate to generate free radicals [105]. In this respect, 2 H-MoS₂ nanomaterial can also serve as a good

photothermal agent for persulfate activation to degrade organic pollutants. Particularly, compared to photocatalytic technology which still shows a limited utilization of solar energy and low apparent quantum efficiency, a much higher energy conversion efficiency can be attained in photothermal process due to the maximally achievable utilization of visible and NIR region of sunlight [182]. Therefore, vast efforts have been devoted to realize photothermal industrialization during the past few years [182]. On the other hand, harnessing the photothermal process to activate persulfate is a promising solution to overcome the problem of high energy consumption encountered by the heat-activated PS-AOPs system. It is worth mentioning that 1 T-MoS₂ displays better photothermal performance than 2 H-MoS₂ while application of the former as a photothermal agent in PS-AOPs is not documented in the literature. Hence, we only discuss the reactions during photothermal persulfate activation process mediated by 2 H-MoS₂-based nanomaterials in the following parts.

In the photothermally-activated PS-AOPs system mediated by 2 H-MoS₂-based nanomaterials, the solution temperature is elevated to higher than 40 °C under solar light irradiation through the function of

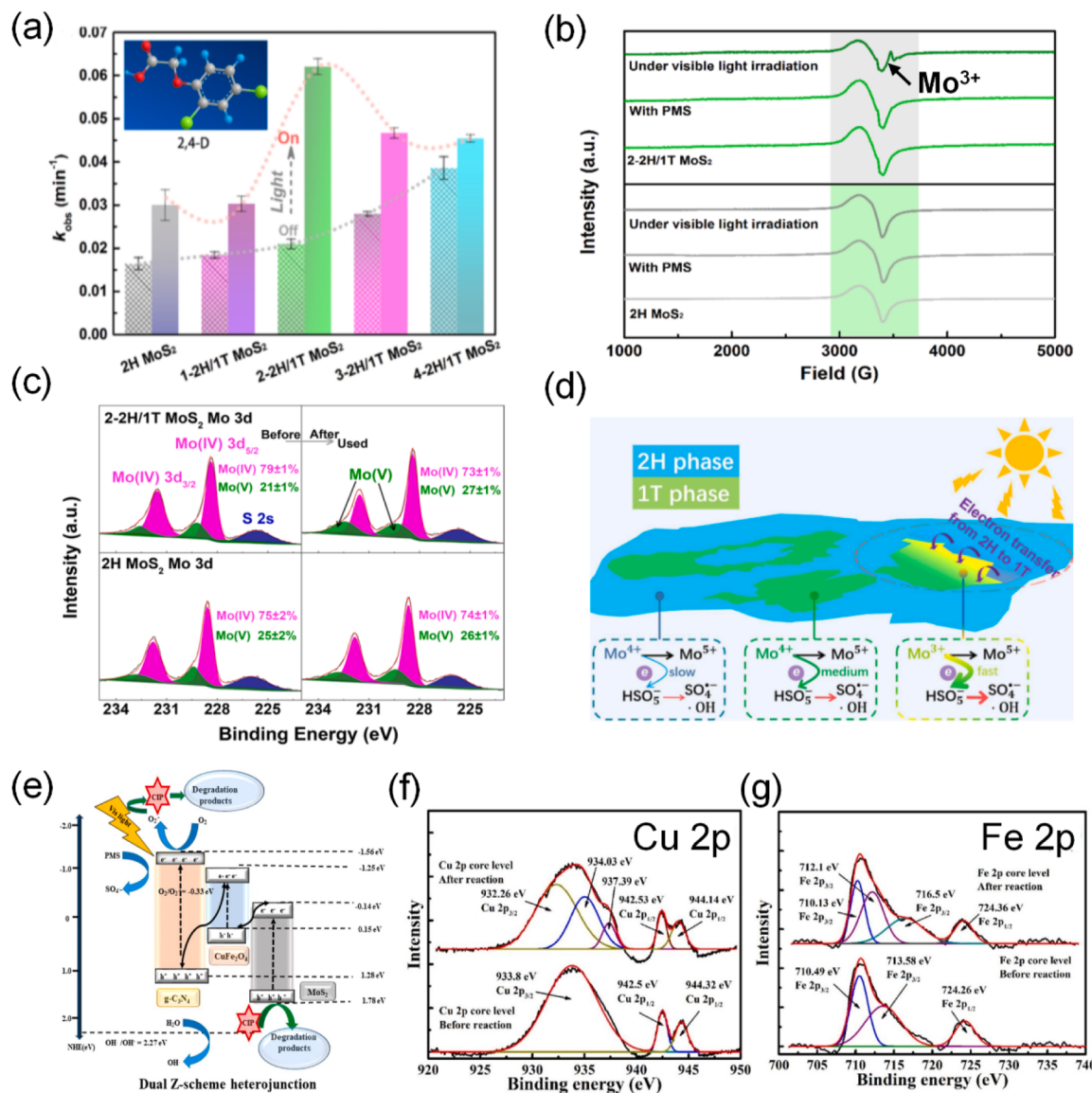


Fig. 16. (a) Rate constants of 2,4-D degradation via activating PMS by nanostructured multiphasic 1 T/2 H-MoS₂ samples containing different level of 1 T phase with (red dashed line) and without (gray dashed line) light irradiation. Inset is the molecular structure of 2,4-D, wherein red, blue, gray and yellow balls are O, H, C and Cl atoms, respectively. (b) In situ EPR spectra at 70 K in the PMS activation process with different nanostructured 2 H-MoS₂ samples under visible light irradiation. (c) High-resolution XPS spectra of Mo 3d for 2 H and 1 T/2 H-MoS₂ photocatalyst before and after five runs of PMS activation under visible light irradiation. (d) Schematic illustration of the mechanism for stable PMS activation using the 1 T/2 H MoS₂ heterojunction under visible light irradiation. (e) Schematic representation of the possible charge separation and transfer pathways in the dual Z-scheme heterojunction formed between g-C₃N₄, CuFe₂O₄ and MoS₂ under visible light for PMS activation and CIP degradation. High-resolution XPS spectra of (f) Cu 2p and (g) Fe 2p for g-CN/CuFe₂O₄/MoS₂ photocatalyst before and after PMS activation under visible light irradiation.

(a-d) Reproduced with permission from ref. [73]. Copyright 2019, American Chemical Society. (e-g) Reproduced with permission from ref. [169]. Copyright 2022, Elsevier.

photothermal agent, and the high temperature is sufficient to trigger the breakdown of O-O bond in persulfate molecules [103], giving rise to the generation of free radicals. Meanwhile, the photocatalytic reactions depicted in Fig. 15b also take place in the photothermally-activated PS-AOP system (if the system is only under NIR irradiation, the photocatalytic reactions would not occur). Thereby, 2 H-MoS₂-based nanomaterials can play a dual role (photocatalyst and photothermal agent) or even triple role (cocatalyst/catalyst, photocatalyst and photothermal agent) during the photothermal persulfate activation process. Notably, the current studies only reported the photothermal activation of PDS, probably because the dissociation energy of O-O bond in PDS is lower than that in PMS [105].

Apparently, those 2 H-MoS₂-based nanomaterial photocatalysts

mentioned in Section 3.2 can also serve as photothermal agents for persulfate activation, while only three examples demonstrating the applications of photothermally-activated PS-AOPs systems with 2 H-MoS₂-based nanomaterials in organic pollutant removal can be found in the literature. Yin et al. employed 2 H-MoS₂ nanosheets to stimulate PDS activation under NIR irradiation for degrading CBZ (Fig. 17 a and b) [56]. Ye's group fabricated a floating solar still based on g-C₃N₄/MoS₂ composite (CM-FSS) to activate PDS under solar irradiance for degrading nitrobenzene (NZ) (Fig. 17 c and d) [183]. In addition, Yan et al. prepared Co-MoS₂/CNT composite photothermal material to activate PDS for degrading RhB under solar irradiance. Furthermore, the authors utilized the as-prepared Co-MoS₂/CNT to modify polytetrafluoroethylene (PTFE) membrane for treating wastewater containing RhB and

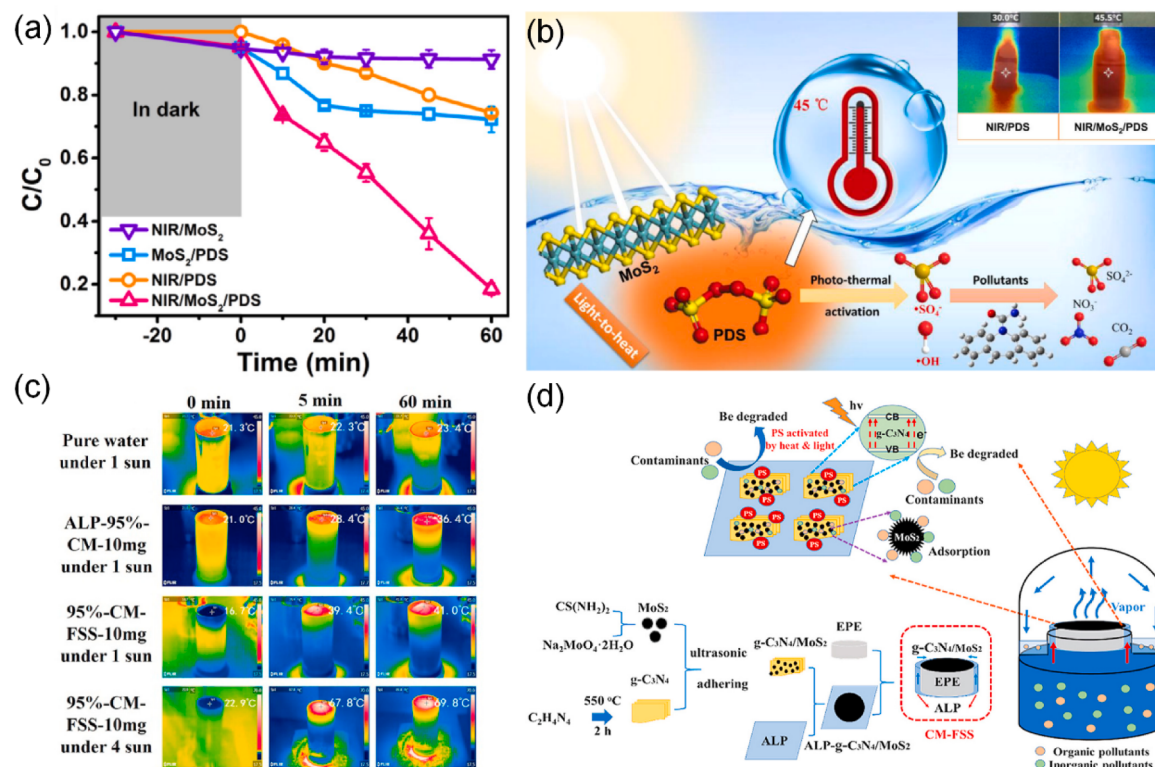


Fig. 17. (a) Photothermal activation of PDS over MoS₂ nanosheets under NIR irradiation for CBZ degradation and the comparison with controlled systems. (b) Proposed mechanism of the light-to-heat conversion to enhance PDS activation by NIR irradiation for pollutant removal. The top right inset is the IR photo of the oxidation processes. (c) IR photos of water covered by CM-FSS under 1 and 4 sun irradiation. (d) Schematic illustration of the organic pollutant degradation in condensed freshwater by a CM-FSS/PDS system under sunlight irradiation.

(a-b) Reproduced with permission from ref. [56]. Copyright 2021, Elsevier. (c-d) Reproduced with permission of ref. [183] Copyright 2021, Elsevier.

found that the Co-MoS₂/CNT/PTFE membrane showed good self-cleaning performance through coupling the photothermal PDS activation into membrane process [184]. Interestingly, a simultaneous production of freshwater and removal of organic pollutants could be attained in Ye's and Yan's works since the surface temperature of CM-FSS/modifed PTFE membrane increased to > 64 °C arising from the air-water interfacial solar heating effect and water molecules were evaporated under such high temperature [183]. It should be pointed out that simulated sunlight source with stable input of light energy was utilized in the above studies and the high temperature was held steady. Nevertheless, under the natural sunlight irradiation, the temperature would fluctuate in photothermal systems due to the unstable solar light intensity and whether the temperature fluctuation would have an effect on the persulfate activation process remains to be ascertained.

3.4. 2 H-MoS₂-based nanomaterials as piezocatalysts for persulfate activation

3.4.1. Principle of piezocatalysis

The catalytic activity of nanostructured 2 H-MoS₂ can also be improved by exerting mechanical stress on the material because it possesses good piezoelectric property. As introduced in Section 2.5, the mechanical deformation of a piezoelectric material induces the change of its band structure and formation of a built-in electric field (piezopotential). Owing to the peculiar properties of piezopotential, it is also utilized to manipulate the charge carriers transportation process in the surface/subsurface area and bulk phase of piezoelectric crystals, thus promoting the catalytic activity [185,186]. Piezoelectric effect has been exploited to catalyze various reactions like water splitting, oxidation of organic contaminants and organic synthesis, as well as persulfate activation, which is termed as piezocatalysis [57,58,187–193]. At the

current stage, the mechanism of piezocatalysis is still debatable and two popular theories are proposed to explain the mechanism: energy band theory and screening charge effect (Fig. 18a) [185].

In the energy band theory, electrons are excited from the VB to the CB by the mechanical force and produced reactive piezo-induced e⁻ and h⁺ on a piezocatalyst, resembling photocatalysis. Meanwhile, due to the formation of piezopotential, the band levels are tilted, and the mobility and separation efficiency of charge carriers in the piezocatalyst are improved, facilitating the catalytic reactions. For the mechanism of screening charge effect, dynamic adsorption and desorption cycles of screening charges occur at the polarized surface of a periodically deformed piezocatalyst, and the screening charges participate in the redox reactions during the dynamic cycle. The prerequisite for the screening charges to trigger a specific chemical reaction is the full match between the magnitude of piezopotential and the demanded redox level, being consistent with electrocatalysis. Regarding the mechanism of piezocatalytic activation of persulfate, few investigations have been conducted and the current studies tend to use the energy band theory to explain the intrinsic mechanism involved in piezo-activated PS-AOPs systems.

3.4.2. Applications of 2 H-MoS₂-based nanomaterial piezocatalysts in PS-AOPs and the involved persulfate activation mechanism

The piezocatalytic activation of persulfate for degrading organic micropollutants is of current interest because it can harvest the natural mechanical energies (e.g., water flow, wind, footsteps, etc.) and thus offers an economical and sustainable approach for water remediation. Due to the excellent piezoelectric property of MoS₂, it has been widely applied as a piezocatalyst for persulfate activation [57,194]. Although 3R-MoS₂ manifests a better piezoelectric response than the 2 H phase, the current studies are mainly focused on the nanostructured 2 H-MoS₂

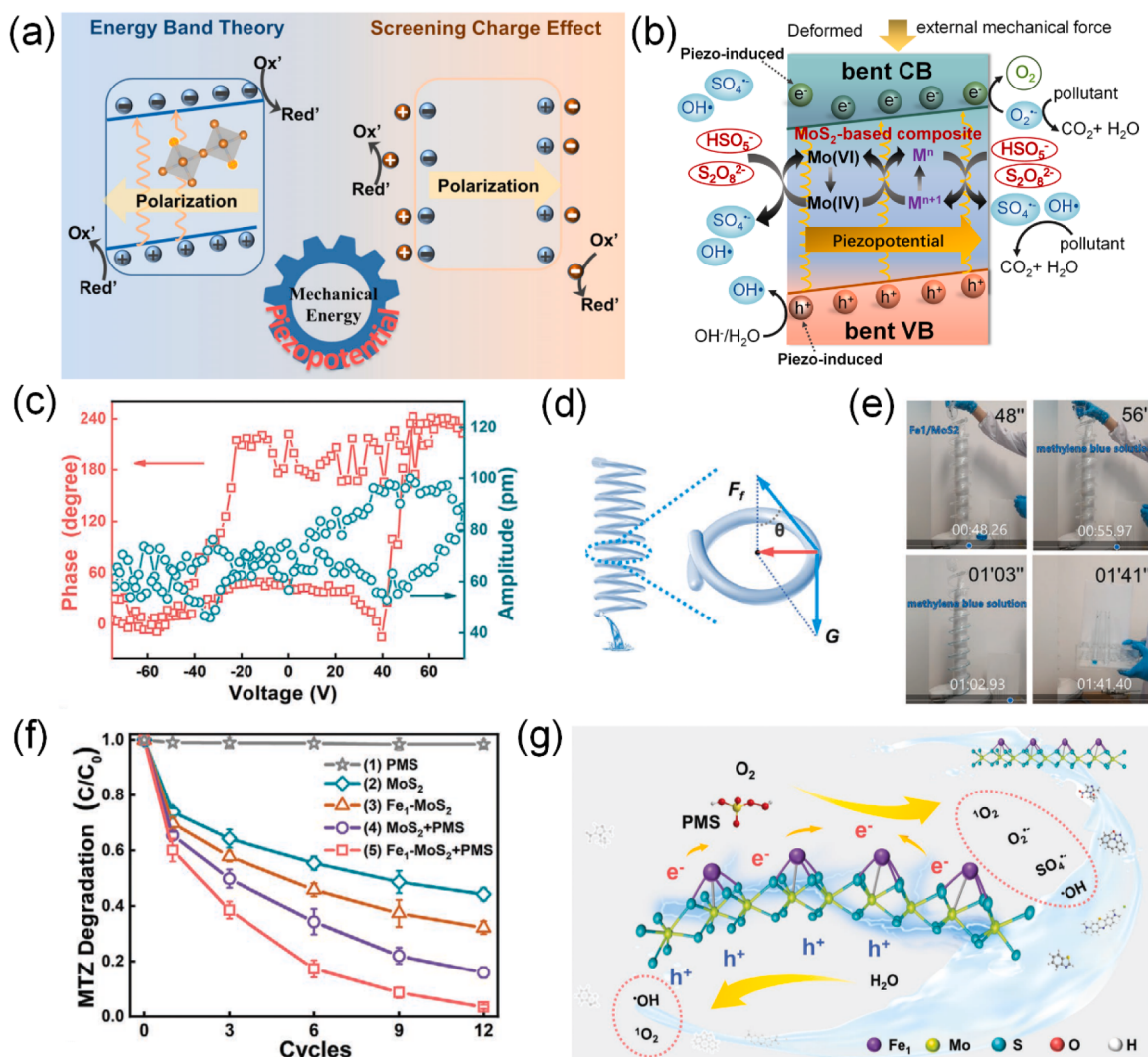


Fig. 18. (a) Schematic summary of piezocatalysis mechanisms: energy band theory (left) and screening charge effect (right). (b) Conceptual illustration of the mechanism in a piezo-activated PS-AOP system mediated by the MoS₂-based piezocatalyst. (c) PFM phase hysteresis loop and amplitude butterfly loop of Fe₁-MoS₂. (d) Scheme of the spiral reactor. (e) Screenshots in different time points for methylene blue degradation during the piezo-activated PMS process mediated by Fe₁-MoS₂. (f) MTZ degradation via Fe₁-MoS₂ piezo-activated PMS process and the comparative processes in the spiral reactor. (g) The principal scheme of Fe₁-MoS₂ for water flow-driven self-powered piezo-activated PMS for water purification.

(a) Reproduced with permission from ref. [185]. Copyright 2021, Wiley-VCH Verlag GmbH & Co. KGaA, Weinheim. (c-g) Reproduced with permission from ref. [58]. Copyright 2021, Wiley-VCH Verlag GmbH & Co. KGaA, Weinheim.

piezocatalyst due to its easy availability. Single-/few-layer 2 H-MoS₂ NFs/nanosheets have been commonly reported to exhibit good piezocatalytic performance in oxidizing organic pollutants [190,192,195, 196]. For instance, Ao's group applied 2 H-MoS₂ NFs as the piezocatalyst to activate PMS under ultrasonic wave (US) which serves as the mechanical force for degrading phenol [57]. The US/MoS₂ NFs/PMS system was observed to achieve a phenol removal efficiency of ~95%, much higher than the controlled systems including MoS₂ NFs/PMS system without US vibration, US/PMS and US/MoS₂ NFs. Particularly, contrast to the low stability of MoS₂ as the catalyst for persulfate activation, the phenol removal efficiency by MoS₂ NFs piezocatalyst barely declined after three consecutive cycles, suggesting the superiority of piezocatalysis in persulfate activation.

To elevate the piezocatalytic activity of 2 H-MoS₂, various modifications have been attempted. Defect and phase (1 T/2 H) engineering are popular approaches to improve the activity of piezocatalyst because they can increase the mobility and concentration of free charge carriers [74,194]. In addition, doping with oxygen/transition metal atom, compounding with a conductor are also effective strategies to improve

charge carrier mobility and separation efficiency of piezo-induced e⁻/h⁺ pairs in 2 H-MoS₂, thus boosting the piezocatalytic reaction [94,197, 198]. Meanwhile, the two chemical modifications can reduce the agglomeration of MoS₂ nanosheets and regulate the layers of MoS₂, which directly impact the corresponding piezopotential. Particularly, doping an alien element into the MoS₂ lattice is able to break the inversion symmetry of 2 H-MoS₂ structure, which is conducive to the piezoelectricity. Coupling with other semiconductor is also efficient to promote the piezocatalytic activity of 2 H-MoS₂ because the construction of heterojunction interfaces can extend the width of the space-charge region in semiconductors and increase the interfacial piezopotential which plays a crucial role in piezocatalysis [199]. So far, 1 T/2 H-MoS₂ NFs, BaTiO₃/MoS₂, Fe atom-doped 2 H-MoS₂ NFs (Fe₁-MoS₂), Co₃S₄/MoS₂, Fe atom-doped MoS₂ nanosheets-carbon fiber cloth (Fe@MoS₂/CFC (h)) have been developed for piezocatalytic activation of persulfate to eliminate organic pollutants (Table 3) [58,187, 200–202].

2 H-MoS₂-based nanomaterial also plays multiple roles including cocatalyst/catalyst and piezocatalyst in the piezocatalytic persulfate

activation processes wherein a cascade of reactions can occur (Fig. 18b): (i) the intrinsic free charges of MoS₂/MoS₂-based composite react with persulfate to produce ROS for oxidizing organic pollutants; (ii) piezo-induced e⁻ reacts with persulfate to evolve free radicals for oxidizing organic pollutants; (iii) piezo-induced e⁻ reacts with oxygen molecules and piezo-induced h⁺ reacts with water molecules (due to the tilt of band levels) to evolve reactive species; (iv) piezo-induced e⁻ and/or MoS₂ as the cocatalyst facilitate the regeneration of metallic active sites in MoS₂-based composite piezocatalyst.

For instance, Zhu's group reported the excellent performance of a Fe₁-MoS₂ piezocatalyst in activating PMS to eliminate metronidazole (MTZ) and several other types of organic contaminants like BTB, CBZ and dyes (Fig. 18 d-i) [58]. It is worth noting that the authors designed a spiral reactor which mimics the urban drainage to launch the piezo-catalytic activation of PMS and degradation of pollutants. The water flow inside the spiral reactor can serve as the mechanical force to induce a considerable degree of deformation of the piezo-catalyst, subsequently triggering PMS activation. The sole piezo-catalytic degradation efficiency of MTZ after 12 cycles of water flow from inlet to outlet by Fe₁-MoS₂ (67.9%) was higher than that by MoS₂ (55.8%), consolidating the improved piezoelectricity in Fe₁-MoS₂. Meanwhile, a MTZ degradation efficiency of 96.5% was achieved by adding both Fe₁-MoS₂ and PMS into the spiral reactor. Due to the continuous regeneration of active sites during the piezocatalytic activation process, Fe₁-MoS₂ also exhibited good stability. By integrating the experimental results and DFT calculations on the adsorption configurations of PMS molecules onto pristine and deformed Fe₁-MoS₂, the authors proposed that the interacting of piezo-induced e⁻ and Fe atomic sites on the piezocatalyst with PMS and dissolved oxygen produced SO₄²⁻, •OH and O₂[•]. At the same time, H₂O molecules were oxidized by the piezo-induced h⁺ to form •OH. Finally, the produced OH and O₂[•] were transformed into ¹O₂ through a cascade of reactions, making ¹O₂ play a lead role in oxidation of organic pollutants.

Very recently, simultaneous organic pollutant degradation and energy/fuel production by the piezo-activated PS-AOPs system have been achieved [200–202]. For instance, Xu et al. reported that a novel piezo-photocatalytic fuel cell based on the helical Fe@MoS₂/CFC (h) anode and PMS activation exhibited excellent berberine removal efficiency and remarkable power generation [202]. Xing's group found that the interactions between H⁺/carbonate and piezo-induced e⁻ generated a considerable amount of H₂/CO during the treatment of practical wastewater by a piezocatalytic MoS₂/Fe⁰/PMS ternary system and a Co₃S₄/MoS₂/PMS system, respectively [200,201]. These exciting results suggest that the utilization of piezo-activated PS-AOPs in wastewater treatment also provides a possible way for helping the sewage treatment plant to realize low-carbon economy, which is of great significance in reality.

3.5. Comparison of different activation approaches based on MoS₂-based materials

Owing to the diverse physicochemical properties of MoS₂, they can activate persulfate by several ways including catalytic, photocatalytic, photothermal and piezocatalytic activation. Among them, catalytic activation is the simplest method, while the stability of MoS₂-based catalyst remains to be a challenge. For photocatalytic, photothermal and piezocatalytic activation method, multiple activation processes can occur simultaneously when a versatile MoS₂-based material is utilized, which significantly enhance the removal of organic pollutant, and the stability of catalyst can be improved compared to the case of catalytic activation. Moreover, generation of value-added products can also be attained beside the elimination of organic pollutants by the above three activation methods. Nevertheless, external energy input is still required for photocatalytic, photothermal and piezocatalytic activation method at the moment. In further work, more efforts on efficient utilization of natural energy to drive PS-AOPs system towards high-efficiency water

treatment should be devoted.

4. Potential risks of MoS₂

Due to the increasing applications of MoS₂-based materials in various areas, the assessments of their potential risks on biological environment and human health are becoming an urgent issue to deal with. MoS₂-based materials would be released into the environment in the course of manufacture, transportation, application or disposal [59]. Once entering into waters, sediments, and soils, MoS₂-based materials might interact with different physicochemical and biological factors, thus possibly exerting negative effects on the aquatic and terrestrial environment [203]. In particular, MoS₂-based nanomaterials can invade into living organisms by different means due to the small size, which might finally cause threats to the health of human beings. Therefore, the cytotoxicity of MoS₂-based materials has been studied via using several *in vitro* and *in vivo* models based on different toxicological endpoints [59,204].

Overall, the toxicity of MoS₂ is strongly dependent on its intrinsic and extrinsic properties including lateral size, crystal structure (1 T, 2 H and 3 R), layer number, surface area and chemistry, aggregation [25]. In addition, the assessment models and methods and exposure conditions also affect the toxicity assessment results [59]. Consequently, it is hard to reach a conclusion about the exact implications of MoS₂ toxicity at the current stage. For example, Bulk MoS₂ is suggested to have low toxicity because it is relatively difficult to degrade and insoluble in body fluids [205]. Exfoliated 1 T/2 H-MoS₂ nanosheets were reported to have lower cytotoxicity in mammalian fibroblast cells than 2 H-MoS₂ nanosheets in Fan's study [206], while Zou et al. suggested that the phytotoxicity of single-layer 1 T-MoS₂ is higher than the single-layer 2 H-MoS₂ [207]. In addition, several researches discovered that MoS₂ nanosheets have no significant toxicology and their biocompatibility can be further improved by proper modifications [59,208–210]. Compared to other popularly used nanomaterials (e.g., titanium dioxide nanoparticles, copper nanoparticles, graphene, etc.), the studies on the potential risks of MoS₂-based materials are relatively limited, which urgently require further investigations.

5. Conclusions and future outlook

MoS₂ mainly exists as 1 T, 2 H and 3 R polytypes and the three polytypes possess different physical and chemical properties. 1 T-MoS₂ is metallic and possesses good electrical conductivity and NIR absorption. 2 H-MoS₂ and 3R-MoS₂ are both semiconductors, and they present peculiar optical, photothermal and piezoelectric properties. Moreover, the electronic structure, optical, photothermal and piezoelectric properties of 2 H/3R-MoS₂ vary with the thickness of the materials, and a 2D form manifests more intriguing properties than the bulk counterpart. Due to the versatile properties of 1 T-MoS₂ and 2 H-MoS₂, they have been widely used in PS-AOPs for degrading organic pollutants. With the exposure of reducing Mo(IV) site at the edges of MoS₂, it can cocatalyze/catalyze the persulfate activation to evolve various ROS, while 1 T-MoS₂ shows higher catalytic activity than 2 H-MoS₂ due to the metallic character. The persulfate activation efficiency of nanostructured 2 H-MoS₂ can be boosted by using external physical stimulations including light irradiation and mechanical force because the peculiar optical, photothermal and piezoelectric properties of nanostructured 2 H-MoS₂ enables it to convert light/mechanical energy into chemical and/or heat energy to activate persulfate. Meanwhile, the chemical, photocatalytic, photothermal and piezocatalytic activities of nanostructured 2 H-MoS₂ towards persulfate activation can be improved via chemical modifications including phase engineering, defect engineering, doping and combining with other functional materials. Overall, different persulfate activation processes can occur simultaneously in an AOPs system driven by multifunctional MoS₂-based materials under the specific condition, attaining enhanced abatement of organic pollutants.

To promote the practical applications of PS-AOPs driven by MoS₂,

based material, we would like to address several existing drawbacks and future challenges here:

- (i) Contrast to the extensively studied 1 T and 2 H-MoS₂ morphology, research on 3R-MoS₂ is in its infancy. Considering the differences in the crystal structure, electronic and optical properties between 3R-MoS₂ and 2 H-MoS₂, 3R-MoS₂ might show distinct catalytic and photocatalytic performances in persulfate activation. However, the catalytic and photocatalytic activities of 3R-MoS₂ are rarely investigated. In addition, 3R-MoS₂ is anticipated to show better piezocatalytic performance in persulfate activation than 2 H-MoS₂ because of its larger piezoelectric coefficient, while relevant studies are absent in the literature. More critically, methods for mass production of high-purity bulk and nanostructured 3R-MoS₂ are still unavailable, which perhaps represents the biggest challenge before realizing the potentially wide use of this MoS₂ polytype.
- (ii) Phase engineering is a popular technique to manipulate the properties and persulfate activation performance of MoS₂, while applications of multiphasic MoS₂ nanomaterials in PS-AOPs are rather limited. Meanwhile, the composition-performance relationship for multiphasic MoS₂-driven PS-AOPs remains to be ascertained yet, especially when various activation processes occur in the system. The balance among the different activity of MoS₂ (catalytic, photocatalytic, photothermal, piezocatalytic) should be considered. In this regard, machine learning is a useful tool to provide a technical guide for delicate phase engineering of MoS₂ towards high-performance water decontamination, and relevant research should be necessitated.
- (iii) The exact implications of MoS₂ toxicity are still debatable. With the wide applications of MoS₂-based materials in different areas involving energy production and storage, environmental protection and biomedicine, various MoS₂ nanomaterials and modifications on MoS₂ are developed and those materials perhaps display distinct environmental fates and toxicities. Hence, extensive research is required to explore the effects of MoS₂-based materials on ecological environment and the underlying mechanism.
- (iv) In the coming carbon-neutral era, source recovery from wastewater rather than simple water purification would be the research focus. In this respect, PS-AOPs show advantages over the traditional Fenton reaction because they can be coupled with other techniques like solar photothermal evaporation, photocatalysis and piezocatalysis to achieve simultaneous water decontamination and production of clean water or chemical fuels like H₂ and CO. As a multifunctional material, fabricating high-performance MoS₂-based composites for coupled PS-AOPs to reduce indirect carbon emissions of the sewage treatment plants is very meaningful in further work.
- (v) Finally, further efforts on obtaining self-powered water treatment systems with generation of value-added products through making full use of the multiple functionalities of MoS₂-based materials simultaneously should be devoted, which is helpful to achieve the goal of zero-emission in sewage treatment industry.

In summary, PS-AOP technique has become a research hotspot in the environmental area over the last decades, but the pilot field studies and full-scale field projects of PS-AOPs in real environment have been rarely reported. Hence, there is still a long way ahead before the large-scale applications of PS-AOPs in practical water treatment. With the multiple functionalities of MoS₂, we hope that the rational design of high-performance MoS₂-based activators could offer opportunities to promote the practical application of PS-AOPs and realize the green and low-carbon development of sewage treatment industry.

Declaration of Competing Interest

The authors declare that they have no known competing financial interests or personal relationships that could have appeared to influence the work reported in this paper.

Data Availability

Data will be made available on request.

Acknowledgement

This work was supported by the National Natural Science Foundation of China (grant nos. 22166025, 21806024 and 22176041), and National Key R&D Program of China (no. 2022YFC3901800).

References

- [1] W.W.A.P. UNESCO, The United Nations world water development report 2021: valuing water, UNESCO, WWDR, 2021.
- [2] X. Lin, J. Xu, A.A. Keller, L. He, Y. Gu, W. Zheng, D. Sun, Z. Lu, J. Huang, X. Huang, G. Li, Occurrence and risk assessment of emerging contaminants in a water reclamation and ecological reuse project, *Sci. Total Environ.* 744 (2020), 140977.
- [3] J. Wang, S. Wang, Reactive species in advanced oxidation processes: formation, identification and reaction mechanism, *Chem. Eng. J.* 401 (2020), 126158.
- [4] J. Du, B. Zhang, J. Li, B. Lai, Decontamination of heavy metal complexes by advanced oxidation processes: a review, *Chin. Chem. Lett.* 31 (2020) 2575–2582.
- [5] Y. Jiang, Z. Xiong, J. Huang, F. Yan, G. Yao, B. Lai, Effective E. coli inactivation of core-shell ZnO@ZIF-8 photocatalysis under visible light synergize with peroxymonosulfate: efficiency and mechanism, *Chin. Chem. Lett.* 33 (2022) 415–423.
- [6] B. Shao, L. Shen, Z. Liu, L. Tang, X. Tan, D. Wang, W. Zeng, T. Wu, Y. Pan, X. Zhang, L. Ge, M. He, Disinfection byproducts formation from emerging organic micropollutants during chlorine-based disinfection processes, *Chem. Eng. J.* 455 (2023), 140476.
- [7] I.A. Ike, K.G. Linden, J.D. Orbell, M. Duke, Critical review of the science and sustainability of persulfate advanced oxidation processes, *Chem. Eng. J.* 338 (2018) 651–669.
- [8] C. Nie, Z. Dai, W. Liu, X. Duan, C. Wang, B. Lai, Z. Ao, S. Wang, T. An, Criteria of active sites in nonradical persulfate activation process from integrated experimental and theoretical investigations: boron–nitrogen-co-doped nanocarbon-mediated peroxydisulfate activation as an example, *Environ. Sci.: Nano* 7 (2020) 1899–1911.
- [9] W. Ren, C. Cheng, P. Shao, X. Luo, H. Zhang, S. Wang, X. Duan, Origins of electron-transfer regime in persulfate-based nonradical oxidation processes, *Environ. Sci. Technol.* 56 (2022) 78–97.
- [10] H. Meng, C. Nie, W. Li, X. Duan, B. Lai, Z. Ao, S. Wang, T. An, Insight into the effect of lignocellulosic biomass source on the performance of biochar as persulfate activator for aqueous organic pollutants remediation: epicarp and mesocarp of citrus peels as examples, *J. Hazard. Mater.* 399 (2020), 123043.
- [11] C. Nie, Z. Ao, X. Duan, C. Wang, S. Wang, T. An, Degradation of aniline by electrochemical activation of peroxydisulfate at MWCNT cathode: The proofed concept of nonradical oxidation process, *Chemosphere* 206 (2018) 432–438.
- [12] C. Nie, Z. Dai, H. Meng, X. Duan, Y. Qin, Y. Zhou, Z. Ao, S. Wang, T. An, Peroxydisulfate activation by positively polarized carbocatalyst for enhanced removal of aqueous organic pollutants, *Water Res.* 166 (2019), 115043.
- [13] J. Lee, U. von Gunten, J.-H. Kim, Persulfate-based advanced oxidation: critical assessment of opportunities and roadblocks, *Environ. Sci. Technol.* 54 (2020) 3064–3081.
- [14] P. Ding, J. Niu, F. Chang, Z. He, T. Wågberg, Z. Li, G. Hu, NiCo2O4 hollow microsphere-mediated ultrafast peroxymonosulfate activation for dye degradation, *Chin. Chem. Lett.* 32 (2021) 2495–2498.
- [15] D. Guo, S. You, F. Li, Y. Liu, Engineering carbon nanocatalysts towards efficient degradation of emerging organic contaminants via persulfate activation: A review, *Chin. Chem. Lett.* 33 (2022) 1–10.
- [16] S. Nimai, H. Zhang, Z. Wu, N. Li, B. Lai, Efficient degradation of sulfamethoxazole by acetylene black activated peroxydisulfate, *Chin. Chem. Lett.* 31 (2020) 2657–2660.
- [17] J. Qi, J. Liu, F. Sun, T. Huang, J. Duan, W. Liu, High active amorphous Co(OH)₂ nanocages as peroxymonosulfate activator for boosting acetaminophen degradation and DFT calculation, *Chin. Chem. Lett.* 32 (2021) 1814–1818.
- [18] Q. He, C. Zhao, L. Tang, Z. Liu, B. Shao, Q. Liang, T. Wu, Y. Pan, J. Wang, Y. Liu, S. Tong, T. Hu, Peroxymonosulfate and peroxydisulfate activation by fish scales biochar for antibiotics removal: synergism of N, P-codoped biochar, *Chemosphere* 326 (2023), 138326.
- [19] Z. Liu, M. He, L. Tang, B. Shao, Q. Liang, T. Wu, Y. Pan, X. Zhang, S. Luo, Q. He, L. Ge, Dual redox cycles of Mn(II)/Mn(III) and Mn(III)/Mn(IV) on porous Mn/N co-doped biochar surfaces for promoting peroxymonosulfate activation and ciprofloxacin degradation, *J. Colloid Interface Sci.* 634 (2023) 255–267.

[20] W. Xiao, M. Cheng, Y. Liu, J. Wang, G. Zhang, Z. Wei, L. Li, L. Du, G. Wang, H. Liu, Functional metal/carbon composites derived from metal–organic frameworks: insight into structures, properties, performances, and mechanisms, *ACS Catal.* 13 (2023) 1759–1790.

[21] C. Guo, M. Cheng, G. Zhang, W. Xiong, C. Zhou, B. Song, L. Du, L. Li, C. Tang, G. Wang, H. Liu, Degradation of organic contaminants by peroxyomonosulfate activated with zeolitic imidazolate framework-based catalysts: performances, mechanisms and stability, *Environ. Sci.: Nano* 10 (2023) 1528–1552.

[22] H. Peng, W. Xiong, Z. Yang, J. Tong, M. Jia, Y. Xiang, S. Sun, Z. Xu, Fe3O4-supported N-doped carbon channels in wood carbon form etching and carbonization: Boosting performance for persulfate activating, *Chem. Eng. J.* 457 (2023), 141317.

[23] Q. Shi, S. Deng, Y. Zheng, Y. Du, L. Li, S. Yang, G. Zhang, L. Du, G. Wang, M. Cheng, Y. Liu, The application of transition metal-modified biochar in sulfate radical based advanced oxidation processes, *Environ. Res.* 212 (2022), 113340.

[24] C. Tang, M. Cheng, C. Lai, L. Li, Z. Wei, D. Ma, L. Du, G. Wang, L. Yang, L. Tang, Multiple path-dominated activation of peroxyomonosulfate by MOF-derived Fe2O3/Mn3O4 for catalytic degradation of tetracycline, *J. Environ. Chem. Eng.* 11 (2023), 110395.

[25] Y. Yu, L. Lu, Q. Yang, A. Zupanic, Q. Xu, L. Jiang, Using MoS2 nanomaterials to generate or remove reactive oxygen species: a review, *ACS Appl. Nano Mater.* 4 (2021) 7523–7537.

[26] L. Zhu, J. Ji, J. Liu, S. Mine, M. Matsuoka, J. Zhang, M. Xing, Designing 3D-MoS2 sponge as excellent cocatalysts in advanced oxidation processes for pollutant control, *Angew. Chem. Int. Ed.* 59 (2020) 13968–13976.

[27] M.I.A. Abdelsoud, A.G. Bedir, M. Bekhit, M.M. Abouelela, R.A. Fahim, A. S. Awed, S.Y. Attia, S.M. Kassem, M.A. Elkodous, G.S. El-Sayyad, S.G. Mohamed, A.I. Osman, D.W. A.a.H. Al-Muhtaseb, Rooney, MoS2-based nanocomposites: synthesis, structure, and applications in water remediation and energy storage: a review, *Environ. Chem. Lett.* 19 (2021) 3645–3681.

[28] Z. Li, X. Meng, Z. Zhang, Recent development on MoS2-based photocatalysis: a review, *J. Photochem. Photobiol. C: Photochem. Rev.* 35 (2018) 39–55.

[29] M.R. Vazirisereshk, A. Martini, D.A. Strubbe, M.Z. Baykara, Solid lubrication with MoS2: a review, *Lubricants* 7 (2019) 57.

[30] G. Zhang, H. Liu, J. Qu, J. Li, Two-dimensional layered MoS2: rational design, properties and electrochemical applications, *Energy Environ. Sci.* 9 (2016) 1190–1209.

[31] A. Gupta, T. Sakthivel, S. Seal, Recent development in 2D materials beyond graphene, *Prog. Mater. Sci.* 73 (2015) 44–126.

[32] Y.P. Venkata Subbaiah, K.J. Saji, A. Tiwari, Atomically thin MoS2: a versatile nongraphene 2D material, *Adv. Funct. Mater.* 26 (2016) 2046–2069.

[33] A. Hirsch, F. Hauke, Post-graphene 2D chemistry: the emerging field of molybdenum disulfide and black phosphorus functionalization, *Angew. Chem. Int. Ed.* 57 (2018) 4338–4354.

[34] Z. Wang, B. Mi, Environmental applications of 2D molybdenum disulfide (MoS2) nanosheets, *Environ. Sci. Technol.* 51 (2017) 8229–8244.

[35] R. Hinchet, U. Khan, C. Falconi, S.-W. Kim, Piezoelectric properties in two-dimensional materials: simulations and experiments, *Mater. Today* 21 (2018) 611–630.

[36] T. Dan, M. Willatzen, Z.L. Wang, Prediction of strong piezoelectricity in 3R-MoS2 multilayer structures, *Nano Energy* 56 (2019) 512–515.

[37] S.S. Chou, B. Kaehr, J. Kim, B.M. Foley, M. De, P.E. Hopkins, J. Huang, C. J. Brinker, V.P. Dravid, Chemically exfoliated MoS2 as near-infrared photothermal agents, *Angew. Chem. Int. Ed.* 52 (2013) 4160–4164.

[38] L. Lei, D. Huang, G. Zeng, M. Cheng, D. Jiang, C. Zhou, S. Chen, W. Wang, A fantastic two-dimensional MoS2 material based on the inert basal planes activation: Electronic structure, synthesis strategies, catalytic active sites, catalytic and electronics properties, *Coord. Chem. Rev.* 399 (2019), 213020.

[39] W. Wu, L. Wang, Y. Li, F. Zhang, L. Lin, S. Niu, D. Chenet, X. Zhang, Y. Hao, T. F. Heinz, J. Hone, Z.L. Wang, Piezoelectricity of single-atomic-layer MoS2 for energy conversion and piezotronics, *Nature* 514 (2014) 470–474.

[40] F.K. Perkins, A.L. Friedman, E. Cobas, P.M. Campbell, G.G. Jernigan, B.T. Jonker, Chemical vapor sensing with monolayer MoS2, *Nano Lett.* 13 (2013) 668–673.

[41] Y.-W. Lu, C. Wang, N. Joshi, H. Liu, MoS2 nanoflowers-activated peroxydisulfate oxidation for rapid and efficient water disinfection, *Water Cycle* 3 (2022) 44–49.

[42] M. Xing, W. Xu, C. Dong, Y. Bai, J. Zeng, Y. Zhou, J. Zhang, Y. Yin, Metal sulfides as excellent co-catalysts for H2O2 decomposition in advanced oxidation processes, *Chem* 4 (2018) 1359–1372.

[43] B. Sheng, F. Yang, Y. Wang, Z. Wang, Q. Li, Y. Guo, X. Lou, J. Liu, Pivotal roles of MoS2 in boosting catalytic degradation of aqueous organic pollutants by Fe(II)/PMS, *Chem. Eng. J.* 375 (2019), 121989.

[44] D. He, Y. Cheng, Y. Zeng, H. Luo, K. Luo, J. Li, X. Pan, D. Barceló, J.C. Crittenden, Synergistic activation of peroxyomonosulfate and persulfate by ferrous ion and molybdenum disulfide for pollutant degradation: Theoretical and experimental studies, *Chemosphere* 240 (2020), 124979.

[45] H. Kuang, Z. He, M. Li, R. Huang, Y. Zhang, X. Xu, L. Wang, Y. Chen, S. Zhao, Enhancing co-catalysis of MoS2 for persulfate activation in Fe3+-based advanced oxidation processes via defect engineering, *Chem. Eng. J.* 417 (2021), 127987.

[46] H. Luo, Y. Cheng, Y. Zeng, K. Luo, D. He, X. Pan, Rapid removal of organic micropollutants by heterogeneous peroxyomonosulfate catalysis over a wide pH range: Performance, mechanism and economic analysis, *Sep. Purif. Technol.* 248 (2020), 117023.

[47] G.-E. Yuan, Y. Qin, M. Feng, X. Ru, X. Zhang, Activation of peroxyomonosulfate by natural molybdenite for dye degradation: Identification of reactive species and catalytic mechanism, *Environ. Technol. Innov.* 22 (2021), 101403.

[48] Y. Chen, G. Zhang, H. Liu, J. Qu, Confining free radicals in close vicinity to contaminants enables ultrafast fenton-like processes in the interspacing of MoS2 membranes, *Angew. Chem. Int. Ed.* 58 (2019) 8134–8138.

[49] H. Zhou, L. Lai, Y. Wan, Y. He, G. Yao, B. Lai, Molybdenum disulfide (MoS2): a versatile activator of both peroxyomonosulfate and persulfate for the degradation of carbamazepine, *Chem. Eng. J.* 384 (2020), 123264.

[50] X. Wang, Z. Chen, Y. He, X. Yi, C. Zhang, Q. Zhou, X. Xiang, Y. Gao, M. Huang, Activation of persulfate-based advanced oxidation processes by 1T-MoS2 for the degradation of imidacloprid: performance and mechanism, *Chem. Eng. J.* 451 (2023), 138575.

[51] J.-C.E. Yang, M.-P. Zhu, X. Duan, S. Wang, B. Yuan, M.-L. Fu, The mechanistic difference of 1T–2H MoS2 homojunctions in persulfates activation: Structure-dependent oxidation pathways, *Appl. Catal. B: Environ.* 297 (2021), 120460.

[52] J. Zhou, X. Guo, X. Zhou, J. Yang, S. Yu, X. Niu, Q. Chen, F. Li, Y. Liu, Boosting the efficiency of Fe-MoS2/peroxyomonosulfate catalytic systems for organic pollutants remediation: Insights into edge-site atomic coordination, *Chem. Eng. J.* 433 (2022), 134511.

[53] J. Lu, Y. Zhou, Y. Zhou, Efficiently activate peroxyomonosulfate by Fe3O4@MoS2 for rapid degradation of sulfonamides, *Chem. Eng. J.* 422 (2021), 130126.

[54] Z. Wu, W. Song, X. Xu, J. Yuan, W. Lv, Y. Yao, High 1T phase and sulfur vacancies in C-MoS2@Fe induced by ascorbic acid for synergistically enhanced contaminants degradation, *Sep. Purif. Technol.* 286 (2022), 120511.

[55] X. Su, Y. Guo, L. Yan, Q. Wang, W. Zhang, X. Li, W. Song, Y. Li, G. Liu, MoS2 nanosheets vertically aligned on biochar as a robust peroxyomonosulfate activator for removal of tetracycline, *Sep. Purif. Technol.* 282 (2022), 120118.

[56] R. Yin, B. Jing, S. He, J. Hu, G. Lu, Z. Ao, C. Wang, M. Zhu, Near-infrared light to heat conversion in peroxydisulfide activation with MoS2: A new photo-activation process for water treatment, *Water Res.* 190 (2021), 116720.

[57] S. Liu, B. Jing, C. Nie, Z. Ao, X. Duan, B. Lai, Y. Shao, S. Wang, T. An, Piezoelectric activation of peroxyomonosulfate by MoS2 nanoflowers for the enhanced degradation of aqueous organic pollutants, *Environ. Sci.: Nano* 8 (2021) 784–794.

[58] S. Lan, B. Jing, C. Yu, D. Yan, Z. Li, Z. Ao, M. Zhu, Protruding iron single-atom accelerated interfacial piezoelectric polarization for self-powered water motion triggered fenton-like reaction, *Small, N/a* (2021) 2105279.

[59] Z. Xu, J. Lu, X. Zheng, B. Chen, Y. Luo, M.N. Tahir, B. Huang, X. Xia, X. Pan, A critical review on the applications and potential risks of emerging MoS2 nanomaterials, *J. Hazard. Mater.* 399 (2020), 123057.

[60] H. Zhou, Z. Xie, Y. Liu, B. Lai, W.-J. Ong, S. Wang, X. Duan, Recent advances in molybdenum disulfide-based advanced oxidation processes, *Environ. Funct. Mater.* 1 (2022) 1–9.

[61] L. WU, P. GUO, H. LI, A. LI, MoS2 catalyzed peroxyomonosulfate activation for organic pollutants degradation: a review, *Acta Mater. Compos. Sin.* 38 (2021) 1348.

[62] S. Barua, H.S. Dutta, S. Gogoi, R. Devi, R. Khan, Nanostructured MoS2-based advanced biosensors: a review, *ACS Appl. Nano Mater.* 1 (2018) 2–25.

[63] Y. Yuan, R.-t Guo, L.-f Hong, X.-y Ji, Z.-s Li, Z.-d Lin, W.-g Pan, Recent advances and perspectives of MoS2-based materials for photocatalytic dyes degradation: a review, *Colloids Surf. A: Physicochem. Eng. Asp.* 611 (2021), 125836.

[64] J. Theerthagiri, R.A. Senthil, B. Senthilkumar, A. Reddy Polu, J. Madhavan, M. Ashokkumar, Recent advances in MoS2 nanostructured materials for energy and environmental applications – A review, *J. Solid State Chem.* 252 (2017) 43–71.

[65] S. Banerjee, S. Bairagi, S. Wazed Ali, A critical review on lead-free hybrid materials for next generation piezoelectric energy harvesting and conversion, *Ceram. Int.* 47 (2021) 16402–16421.

[66] J. Strachan, A.F. Masters, T. Maschmeyer, 3R-MoS2 in review: history, status, and outlook, *ACS Appl. Energy Mater.* 4 (2021) 7405–7418.

[67] F. Wypych, C. Solenthaler, R. Prins, T. Weber, Electron diffraction study of intercalation compounds derived from 1T-MoS2, *J. Solid State Chem.* 144 (1999) 430–436.

[68] Y. Fang, J. Pan, J. He, R. Luo, D. Wang, X. Che, K. Bu, W. Zhao, P. Liu, G. Mu, H. Zhang, T. Lin, F. Huang, Structure Re-determination and superconductivity observation of bulk 1T MoS2, *Angew. Chem. Int. Ed.* 57 (2018) 1232–1235.

[69] X.J. Chua, S.M. Tan, X. Chia, Z. Sofer, J. Luxa, M. Pumera, The Origin of MoS2 significantly influences its performance for the hydrogen evolution reaction due to differences in phase purity, *Chem. – A Eur. J.* 23 (2017) 3169–3177.

[70] R. Suzuki, M. Sakano, Y.J. Zhang, R. Akashi, D. Morikawa, A. Harasawa, K. Yaji, K. Kuroda, K. Miyamoto, T. Okuda, K. Ishizaka, R. Arita, Y. Iwasa, Valley-dependent spin polarization in bulk MoS2 with broken inversion symmetry, *Nat. Nanotechnol.* 9 (2014) 611–617.

[71] M. Acerce, D. Voiry, M. Chhowalla, Metallic 1T phase MoS2 nanosheets as supercapacitor electrode materials, *Nat. Nanotechnol.* 10 (2015) 313–318.

[72] L. Wang, X. Zheng, L. Yan, W. Song, Y. Li, B. Wu, X. Li, Multiphasic MoS2 activates peroxyomonosulfate for efficient removal of oxytetracycline: The dominant role of surface reactive species, *Sep. Purif. Technol.* 317 (2023), 123907.

[73] Y. Chen, G. Zhang, Q. Ji, H. Liu, J. Qu, Triggering of low-valence molybdenum in multiphasic MoS2 for effective reactive oxygen species output in catalytic fenton-like reactions, *ACS Appl. Mater. Interfaces* 11 (2019) 26781–26788.

[74] T. Ren, W. Tian, Q. Shen, Z. Yuan, D. Chen, N. Li, J. Lu, Enhanced piezocatalysis of polymorphic few-layered MoS2 nanosheets by phase engineering, *Nano Energy* 90 (2021), 106527.

[75] R.M. Arif Khalil, F. Hussain, A. Manzoor Rana, M. Imran, G. Murtaza, Comparative study of polytype 2H-MoS2 and 3R-MoS2 systems by employing DFT, *Phys. E: Low.-Dimens. Syst. Nanostruct.* 106 (2019) 338–345.

[76] Y. Jiao, A.M. Hafez, D. Cao, A. Mukhopadhyay, Y. Ma, H. Zhu, Metallic MoS₂ for high performance energy storage and energy conversion, *Small* 14 (2018) 1800640.

[77] M. Paillet, R. Parret, J.-L. Sauvajol, P. Colombe, Graphene and related 2D materials: an overview of the Raman studies, *J. Raman Spectrosc.* 49 (2018) 8–12.

[78] S. Jiménez Sandoval, D. Yang, R.F. Frindt, J.C. Irwin, Raman study and lattice dynamics of single molecular layers of $\{\text{MoS}\}_{\{2\}}$, *Phys. Rev. B* 44 (1991) 3955–3962.

[79] C.V. Ramana, U. Becker, V. Shutthanandan, C.M. Julien, Oxidation and metal-insertion in molybdenite surfaces: evaluation of charge-transfer mechanisms and dynamics, *Geochim. Trans.* 9 (2008) 8.

[80] C. Lee, H. Yan, L.E. Brus, T.F. Heinz, J. Hone, S. Ryu, Anomalous lattice vibrations of single- and few-layer MoS₂, *ACS Nano* 4 (2010) 2695–2700.

[81] M. Xia, B. Li, K. Yin, G. Capellini, G. Niu, Y. Gong, W. Zhou, P.M. Ajayan, Y.-H. Xie, Spectroscopic signatures of AA' and AB stacking of chemical vapor deposited bilayer MoS₂, *ACS Nano* 9 (2015) 12246–12254.

[82] J. van Baren, G. Ye, J.-A. Yan, Z. Ye, P. Rezaie, P. Yu, Z. Liu, R. He, C.H. Lui, Stacking-dependent interlayer phonons in 3R and 2H MoS₂, *2D Mater.* 6 (2019), 025022.

[83] C. Mutalik, G. Okoro, H.-L. Chou, I.H. Lin, S. Yougbaré, C.-C. Chang, T.-R. Kuo, Phase-dependent 1T/2H-MoS₂ nanosheets for effective photothermal killing of bacteria, *ACS Sustain. Chem. Eng.* 10 (2022) 8949–8957.

[84] Z. Liang, R. Shen, Y.H. Ng, P. Zhang, Q. Xiang, X. Li, A review on 2D MoS₂ cocatalysts in photocatalytic H₂ production, *J. Mater. Sci. Technol.* 56 (2020) 89–121.

[85] S. Karunakaran, S. Pandit, B. Basu, M. De, Simultaneous exfoliation and functionalization of 2H-MoS₂ by thiolated surfactants: applications in enhanced antibacterial activity, *J. Am. Chem. Soc.* 140 (2018) 12634–12644.

[86] G. Eda, H. Yamaguchi, D. Voiry, T. Fujita, M. Chen, M. Chhowalla, Photoluminescence from chemically exfoliated MoS₂, *Nano Lett.* 11 (2011) 5111–5116.

[87] P. Ci, Y. Chen, J. Kang, R. Suzuki, H.S. Choe, J. Suh, C. Ko, T. Park, K. Shen, Y. Iwasa, S. Tongay, J.W. Ager III, L.-W. Wang, J. Wu, Quantifying van der Waals interactions in layered transition metal dichalcogenides from pressure-enhanced valence band splitting, *Nano Lett.* 17 (2017) 4982–4988.

[88] K.F. Mak, C. Lee, J. Hone, J. Shan, T.F. Heinz, Atomically thin MoS₂: a new direct-gap semiconductor, *Phys. Rev. Lett.* 105 (2010), 136805.

[89] X.-Q. Fang, J.-X. Liu, V. Gupta, Fundamental formulations and recent achievements in piezoelectric nano-structures: a review, *Nanoscale* 5 (2013) 1716–1726.

[90] P. Lin, C. Pan, Z.L. Wang, Two-dimensional nanomaterials for novel piezotronics and piezophotonics, *Mater. Today Nano* 4 (2018) 17–31.

[91] K.-A.N. Duerloo, M.T. Ong, E.J. Reed, Intrinsic piezoelectricity in two-dimensional materials, *J. Phys. Chem. Lett.* 3 (2012) 2871–2876.

[92] H. Zhu, Y. Wang, J. Xiao, M. Liu, S. Xiong, Z.J. Wong, Z. Ye, Y. Ye, X. Yin, X. Zhang, Observation of piezoelectricity in free-standing monolayer MoS₂, *Nat. Nanotechnol.* 10 (2015) 151–155.

[93] S. Konabe, T. Yamamoto, Piezoelectric coefficients of bulk 3R transition metal dichalcogenides, *Jpn. J. Appl. Phys.* 56 (2017), 098002.

[94] R. Lei, F. Gao, J. Yuan, C. Jiang, X. Fu, W. Feng, P. Liu, Free layer-dependent piezoelectricity of oxygen-doped MoS₂ for the enhanced piezocatalytic hydrogen evolution from pure water, *Appl. Surf. Sci.* 576 (2022), 151851.

[95] W. Ma, B. Yao, W. Zhang, Y. He, Y. Yu, J. Niu, C. Wang, A novel multi-flaw MoS₂ nanosheet piezocatalyst with superhigh degradation efficiency for ciprofloxacin, *Environ. Sci.: Nano* 5 (2018) 2876–2887.

[96] G. Li, D. Zhang, Q. Qiao, Y. Yu, D. Peterson, A. Zafar, R. Kumar, S. Curtarolo, F. Hunte, S. Shannon, Y. Zhu, W. Yang, L. Cao, All The Catalytic Active Sites of MoS₂ for Hydrogen Evolution, *J. Am. Chem. Soc.* 138 (2016) 16632–16638.

[97] X. Li, Y. Guo, L. Yan, T. Yan, W. Song, R. Feng, Y. Zhao, Enhanced activation of peroxymonosulfate by ball-milled MoS₂ for degradation of tetracycline: Boosting molybdenum activity by sulfur vacancies, *Chem. Eng. J.* 429 (2022), 132234.

[98] D. Voiry, M. Salehi, R. Silva, T. Fujita, M. Chen, T. Asefa, V.B. Shenoy, G. Eda, M. Chhowalla, Conducting MoS₂ Nanosheets as Catalysts for Hydrogen Evolution Reaction, *Nano Lett.* 13 (2013) 6222–6227.

[99] R.J. Toh, Z. Sofer, J. Luxa, D. Sedmidubský, M. Pumera, 3R phase of MoS₂ and WS₂ outperforms the corresponding 2H phase for hydrogen evolution, *Chem. Commun.* 53 (2017) 3054–3057.

[100] M.R. Saber, G. Khabiri, A.A. Maarouf, M. Ulbricht, A.S.G. Khalil, A comparative study on the photocatalytic degradation of organic dyes using hybridized 1T/2H, 1T/3R and 2H MoS₂ nano-sheets, *RSC Adv.* 8 (2018) 26364–26370.

[101] J. Luxa, L. Spejchalová, I. Jakubec, Z. Sofer, MoS₂ stacking matters: 3R polytype significantly outperforms 2H MoS₂ for the hydrogen evolution reaction, *Nanoscale* 13 (2021) 19391–19398.

[102] R. Bai, W. Yan, Y. Xiao, S. Wang, X. Tian, J. Li, X. Xiao, X. Lu, F. Zhao, Acceleration of peroxymonosulfate decomposition by a magnetic MoS₂/CuFe₂O₄ heterogeneous catalyst for rapid degradation of fluoxetine, *Chem. Eng. J.* 397 (2020), 125501.

[103] F. Ghanbari, M. Moradi, Application of peroxymonosulfate and its activation methods for degradation of environmental organic pollutants: Review, *Chem. Eng. J.* 310 (2017) 41–62.

[104] L. Wang, J. Jiang, J. Ma, S. Pang, T. Zhang, A review on advanced oxidation processes homogeneously initiated by copper(II), *Chem. Eng. J.* 427 (2022), 131721.

[105] S. Wacławek, H.V. Lutze, K. Grübel, V.V.T. Padil, M. Černík, D.D. Dionysiou, Chemistry of persulfates in water and wastewater treatment: A review, *Chem. Eng. J.* 330 (2017) 44–62.

[106] G.P. Anipsitakis, D.D. Dionysiou, Radical Generation by the Interaction of Transition Metals with Common Oxidants, *Environ. Sci. Technol.* 38 (2004) 3705–3712.

[107] Y. Li, Y. Feng, B. Yang, Z. Yang, K. Shih, Activation of peroxymonosulfate by molybdenum disulfide-mediated traces of Fe(III) for sulfadiazine degradation, *Chemosphere* 283 (2021), 131212.

[108] Y. Zhang, J. Niu, J. Xu, Fe(II)-promoted activation of peroxymonosulfate by molybdenum disulfide for effective degradation of acetaminophen, *Chem. Eng. J.* 381 (2020), 122718.

[109] S. Wang, W. Xu, J. Wu, Q. Gong, P. Xie, Improved sulfamethoxazole degradation by the addition of MoS₂ into the Fe²⁺/peroxymonosulfate process, *Sep. Purif. Technol.* 235 (2020), 116170.

[110] M. Huang, X. Wang, C. Liu, G. Fang, J. Gao, Y. Wang, D. Zhou, Mechanism of metal sulfides accelerating Fe(II)/Fe(III) redox cycling to enhance pollutant degradation by persulfate: Metallic active sites vs. reducing sulfur species, *J. Hazard. Mater.* 404 (2021), 124175.

[111] Y.-q. Gao, Y.-y. Rao, H. Ning, D.-q. Yin, N.-y. Gao, MoS₂-assisted Fe²⁺/peroxymonosulfate oxidation for the abatement of phenacetin: efficiency, mechanisms and toxicity evaluation, *RSC Adv.* 11 (2021) 33149–33159.

[112] X. Song, J. Tian, W. Shi, F. Cui, Y. Yuan, Significant acceleration of Fe²⁺/peroxydisulfate oxidation towards sulfisoxazole by addition of MoS₂, *Environ. Res.* 188 (2020), 109692.

[113] C. Pan, L. Fu, Y. Ding, X. Peng, Q. Mao, Homogeneous catalytic activation of peroxymonosulfate and heterogeneous reductive regeneration of Co²⁺ by MoS₂: The pivotal role of pH, *Sci. Total Environ.* 712 (2020), 136447.

[114] J. Ji, R.M. Aleisa, H. Duan, J. Zhang, Y. Yin, M. Xing, Metallic Active Sites on MoO₂(110) Surface to Catalyze Advanced Oxidation Processes for Efficient Pollutant Removal, *iScience* 23 (2020), 100861.

[115] X. Xie, J. Cao, Y. Xiang, R. Xie, Z. Suo, Z. Ao, X. Yang, H. Huang, Accelerated iron cycle inducing molecular oxygen activation for deep oxidation of aromatic VOCs in MoS₂ co-catalytic Fe³⁺/PMS system, *Appl. Catal. B: Environ.* 309 (2022), 121235.

[116] Y. Zhu, F. Wang, B. Zhou, H. Chen, R. Yuan, Y. Zhang, H. Geng, Y. Liu, H. Wang, Photo-assisted Fe²⁺ modified molybdenum disulfide activated potassium persulfate to degrade sulfadiazine: Insights into the degradation pathway and mechanism from density functional theory, *Chem. Eng. J.* 435 (2022), 134904.

[117] G. Liu, Q. Wang, M. Zhang, L. Dong, P. Rao, X. Zhang, N. Gao, J. Deng, High-effective degradation of thiamphenicol with ferrous/ polyaniline encapsulated in molybdenum disulfide activate peroxymonosulfate: Synergism of iron and molybdenum, *Chem. Eng. J.* 459 (2023), 141613.

[118] X. Xie, Y. Xiang, J. Cao, W. Dai, Z. Ao, H. Huang, X. Yang, F. Xiao, X. Ye, High-efficiency destruction of aromatic VOC mixtures in a MoS₂ cocatalytic Fe³⁺/PMS reaction, *Sep. Purif. Technol.* 305 (2023), 122444.

[119] X. Song, J. Ni, D. Liu, W. Shi, Y. Yuan, F. Cui, J. Tian, W. Wang, Molybdenum disulfide as excellent Co-catalyst boosting catalytic degradation of sulfamethoxazole by nZVI/PDS process, *Sep. Purif. Technol.* 285 (2022), 120398.

[120] Z. Yan, F. He, J. Zhang, J. Fang, J. Wang, H. Zhou, Enhanced Fe(III)/PMS system by flower-like MoS₂ nanosheet for rapid degradation of tetracycline, *J. Environ. Chem. Eng.* 10 (2022), 108860.

[121] Y. You, Z. He, Phenol degradation in iron-based advanced oxidation processes through ferric reduction assisted by molybdenum disulfide, *Chemosphere* 312 (2023), 137278.

[122] A. Latif, S. Kai, Y. Si, Catalytic degradation of organic pollutants in Fe(III)/peroxymonosulfate (PMS) system: performance, influencing factors, and pathway, *Environ. Sci. Pollut. Res.* 26 (2019) 36410–36422.

[123] H. Peng, R. Chen, N. Tao, Y. Xiao, C. Li, T. Zhang, M. Ye, MoS₂ boosts the Fe²⁺/PMS process for carbamazepine degradation, *Environ. Sci. Pollut. Res.* 29 (2022) 49267–49278.

[124] D. Zhang, Z. An, Y. Zhang, Y. Hu, J. Zhan, H. Zhou, M. Wu, MoS₂@SiO₂ enhanced persulfate oxidation for the degradation of triazine herbicides in fixed-bed reactor, *J. Water Process Eng.* 52 (2023), 103523.

[125] M. Sun, W. Huang, H. Cheng, J. Ma, Y. Kong, S. Komarneni, Degradation of dye in wastewater by Homogeneous Fe(VI)/NaHSO₃ system, *Chemosphere* 228 (2019) 595–601.

[126] L. Lin, Y. Ge, H. Zhang, M. Wang, D. Xiao, D. Ma, Heterogeneous catalysis in water, *JACS Au* 1 (2021) 1834–1848.

[127] L. Li, Q. Han, L. Wang, B. Liu, K. Wang, Z. Wang, Dual roles of MoS₂ nanosheets in advanced oxidation processes: activating permonosulfate and quenching radicals, *Chem. Eng. J.* 440 (2022), 135866.

[128] M. Du, Q. Yi, J. Ji, Q. Zhu, H. Duan, M. Xing, J. Zhang, Sustainable activation of peroxymonosulfate by the Mo(IV) in MoS₂ for the remediation of aromatic organic pollutants, *Chin. Chem. Lett.* 31 (2020) 2803–2808.

[129] Y. Sun, H. Li, S. Zhang, M. Hua, J. Qian, B. Pan, Revisiting the heterogeneous peroxymonosulfate activation by MoS₂, a Surf. Mo-Peroxymonosulfate Complex Major React. Species, *ACS EST Water* 2 (2022) 376–384.

[130] W. Ren, G. Nie, P. Zhou, H. Zhang, X. Duan, S. Wang, The intrinsic nature of persulfate activation and n-doping in carbocatalysis, *Environ. Sci. Technol.* 54 (2020) 6438–6447.

[131] Y. Gao, Y. Zhu, Z. Chen, Q. Zeng, C. Hu, Insights into the difference in metal-free activation of peroxymonosulfate and peroxydisulfate, *Chem. Eng. J.* 394 (2020), 123936.

[132] H. Zhang, Y. Mei, F. Zhu, F. Yu, S. Komarneni, J. Ma, Efficient activation of persulfate by C@Fe3O4 in visible-light for tetracycline degradation, *Chemosphere* 306 (2022), 135635.

[133] Q. Ji, F. Zhu, Y. Lei, H. Cheng, J. Ma, S. Komarneni, Fe-Co-SBA assisted by visible light can effectively activate NaHSO₃ or H₂O₂ for enhanced degradation of Orange II: Activation of NaHSO₃ versus H₂O₂, *Microporous Mesoporous Mater.* 315 (2021), 110902.

[134] X. Zhang, Y. Mei, H. Cheng, J. Ma, F. Zhu, S. Komarneni, Activation of K₂S₂O₈ by Ni-Ce composite oxides for the degradation of orange II with visible light assistance, *Mater. Chem. Phys.* 270 (2021), 124784.

[135] C. Sun, M. Yu, Y. Li, B. Niu, F. Qin, N. Yan, Y. Xu, Y. Zheng, MoS₂ nanoflowers decorated natural fiber-derived hollow carbon microtubes for boosting perfluorooctanoic acid degradation, *Colloids Surf. A: Physicochem. Eng. Asp.* 642 (2022), 128670.

[136] C. Yi, Z. He, Y. Hu, D. Liang, Y. Zhang, Y. Chen, FeOOH@MoS₂ as a highly effective and stable activator of peroxymonosulfate-based advanced oxidation processes for pollutant degradation, *Surf. Interfaces* 27 (2021), 101465.

[137] J. Ye, J. Dai, D. Yang, C. Li, Y. Yan, Y. Wang, Interfacial engineering of vacancy-rich nitrogen-doped Fe_xO_y@MoS₂ Co-catalytic carbonaceous beads mediated non-radicals for fast catalytic oxidation, *J. Hazard. Mater.* 421 (2022), 126715.

[138] Y. Sun, R. Li, C. Song, H. Zhang, Y. Cheng, A. Nie, H. Li, D.D. Dionysiou, J. Qian, B. Pan, Origin of the improved reactivity of MoS₂ single crystal by confining lattice Fe atom in peroxymonosulfate-based Fenton-like reaction, *Appl. Catal. B: Environ.* 298 (2021), 120537.

[139] L.-Z. Huang, C. Zhou, M. Shen, E. Gao, C. Zhang, X.-M. Hu, Y. Chen, Y. Xue, Z. Liu, Persulfate activation by two-dimensional MoS₂ confining single Fe atoms: Performance, mechanism and DFT calculations, *J. Hazard. Mater.* 389 (2020), 122137.

[140] X. Li, L. Wang, Y. Guo, W. Song, Y. Li, L. Yan, Goethite-MoS₂ hybrid with dual active sites boosted peroxymonosulfate activation for removal of tetracycline: The vital roles of hydroxyl radicals and singlet oxygen, *Chem. Eng. J.* 450 (2022), 138104.

[141] X. Peng, Z. Yang, F. Hu, C. Tan, Q. Pan, H. Dai, Mechanistic investigation of rapid catalytic degradation of tetracycline using CoFe2O4@MoS₂ by activation of peroxymonosulfate, *Sep. Purif. Technol.* 287 (2022), 120525.

[142] W. Wang, Y. Xu, D. Zhong, N. Zhong, Rapid Treatment and Reaction Mechanism of Complexation Plating Effluents by Molybdenum Disulfide/Copper Sulfide+Peroxosulfate Process, *ChemistrySelect* 6 (2021) 11002–11011.

[143] F. Yu, F. Zhu, H. Zhang, S. Komarneni, J. Ma, Efficient activation of K₂S₂O₈ by MoS₂-ZnFe₂O₄ composite for the rapid degradation of tetracycline, *Mater. Lett.* 318 (2022), 132204.

[144] S. Sheng, J. Fu, S. Song, Y. He, J. Qian, Z. Yi, Enhanced electron transfer for activation of peroxymonosulfate via MoS₂ modified iron-based perovskite, *Environ. Technol.* (2022) 1–17.

[145] J. Deng, H. Li, J. Xiao, Y. Tu, D. Deng, H. Yang, H. Tian, J. Li, P. Ren, X. Bao, Triggering the electrocatalytic hydrogen evolution activity of the inert two-dimensional MoS₂ surface via single-atom metal doping, *Energy Environ. Sci.* 8 (2015) 1594–1601.

[146] X. Chen, S. Li, P. Yang, Y. Chen, C. Xue, Y. Long, J. Han, J. Su, W. Huang, D. Liu, N-doped carbon intercalated Fe-doped MoS₂ nanosheets with widened interlayer spacing: An efficient peroxymonosulfate activator for high-salinity organic wastewater treatment, *J. Colloid Interface Sci.* 628 (2022) 318–330.

[147] W. Zhang, X. Wang, D. Wang, J. Shu, Z. Ye, X. Zhang, L. Ran, Q. Zhao, B. Zou, L. Zhou, MoS₂ and Fe3O4 modified spongy wood with micro-reaction cellulose channels and natural water transfer to enhance tetracycline removal, *Cellulose* 29 (2022) 5079–5101.

[148] H. Liu, Z. Tian, C. Huang, P. Wang, S. Huang, X. Yang, H. Cheng, X. Zheng, H. Tian, Z. Liu, A novel 3D Co/Mo co-catalyzed graphene sponge-mediated peroxymonosulfate activation for the highly efficient pollutants degradation, *Sep. Purif. Technol.* 301 (2022), 122035.

[149] H. Liu, C. Huang, P. Wang, S. Huang, X. Yang, H. Xu, J. Zhu, D. Ling, C. Feng, Z. Liu, A novel Fe/Mo co-catalyzed graphene-based nanocomposite to activate peroxymonosulfate for highly efficient degradation of organic pollutants, *Environ. Res.* 215 (2022), 114233.

[150] C. Huang, H. Liu, C. Sun, P. Wang, Z. Tian, H. Cheng, S. Huang, X. Yang, M. Wang, Z. Liu, Peroxymonosulfate activation by graphene oxide-supported 3D-MoS₂/FeCo2O4 sponge for highly efficient organic pollutants degradation, *Environ. Pollut.* 325 (2023), 121391.

[151] X. Duan, H. Sun, S. Wang, Metal-free carbocatalysis in advanced oxidation reactions, *Acc. Chem. Res.* 51 (2018) 678–687.

[152] T. Wu, Z. Liu, B. Shao, Q. Liang, Q. He, Y. Pan, X. Zhang, Y. Liu, J. Sun, S. Gong, Hydrogen peroxide-impregnated supramolecular precursors synthesize mesoporous-rich ant nest-like filled tubular g-C3N4 for effective photocatalytic removal of pollutants, *Chem. Eng. J.* 447 (2022), 137332.

[153] T. Wu, Q. He, Z. Liu, B. Shao, Q. Liang, Y. Pan, J. Huang, Z. Peng, Y. Liu, C. Zhao, X. Yuan, L. Tang, S. Gong, Tube wall delamination engineering induces photogenerated carrier separation to achieve photocatalytic performance improvement of tubular g-C3N4, *J. Hazard. Mater.* 424 (2022), 127177.

[154] X. Zhang, S. Tong, D. Huang, Z. Liu, B. Shao, Q. Liang, T. Wu, Y. Pan, J. Huang, Y. Liu, M. Cheng, M. Chen, Recent advances of Zr based metal organic frameworks photocatalysis: Energy production and environmental remediation, *Coord. Chem. Rev.* 448 (2021), 214177.

[155] D. Tian, H. Zhou, H. Zhang, P. Zhou, J. You, G. Yao, Z. Pan, Y. Liu, B. Lai, Heterogeneous photocatalyst-driven persulfate activation process under visible light irradiation: From basic catalyst design principles to novel enhancement strategies, *Chem. Eng. J.* 428 (2022), 131166.

[156] T. Wang, J. Zhou, W. Wang, Y. Zhu, J. Niu, Ag-single atoms modified S1.66-N1.91/TiO₂-x for photocatalytic activation of peroxymonosulfate for bisphenol A degradation, *Chin. Chem. Lett.* 33 (2022) 2121–2124.

[157] M. Zhang, J. He, Y. Chen, P.-Y. Liao, Z.-Q. Liu, M. Zhu, Visible light-assisted peroxydisulfate activation via hollow copper tungstate spheres for removal of antibiotic sulfamethoxazole, *Chin. Chem. Lett.* 31 (2020) 2721–2724.

[158] M. Wang, B. Guo, J. Zhan, Y. Zhuang, S. Komarneni, J. Ma, Mo doping of BiOBr nanoflowers for the degradation of tetracycline by heterogeneous activation of persulfate under visible light, *Chem. Phys. Lett.* 807 (2022), 140093.

[159] Q. Zhang, H. Zhao, Y. Dong, X. Zhu, X. Liu, H. Li, A novel ternary MQDs/NCds/TiO₂ nanocomposite that collaborates with activated persulfate for efficient RhB degradation under visible light irradiation, *N. J. Chem.* 45 (2021) 1327–1338.

[160] H.S. Lee, S.-W. Min, Y.-G. Chang, M.K. Park, T. Nam, H. Kim, J.H. Kim, S. Ryu, S. Im, MoS₂ Nanosheet Phototransistors with Thickness-Modulated Optical Energy Gap, *Nano Lett.* 12 (2012) 3695–3700.

[161] Q. Liang, X. Liu, B. Shao, L. Tang, Z. Liu, W. Zhang, S. Gong, Y. Liu, Q. He, T. Wu, Y. Pan, S. Tong, Construction of fish-scale tubular carbon nitride-based heterojunction with boosting charge separation in photocatalytic tetracycline degradation and H₂O₂ production, *Chem. Eng. J.* 426 (2021), 130831.

[162] Z. Liu, J. Huang, B. Shao, H. Zhong, Q. Liang, Q. He, T. Wu, Y. Pan, Z. Peng, X. Yuan, Y. Liu, C. Zhao, In-situ construction of 2D/1D Bi₂O₂CO₃ nanoflake/S-doped g-C3N4 hollow tube hierarchical heterostructure with enhanced visible-light photocatalytic activity, *Chem. Eng. J.* 426 (2021), 130767.

[163] S. Wang, M.-r Chen, S.-b Shen, C.-h Cheng, A.-j Cai, A.-j Song, X.-l Lu, G.-s Gao, M.-z Ma, Z.-w Zhang, X.-y Xu, Bifunctionalized Fe7S8@MoS₂-O core-shell with efficient photocatalytic activity based on internal electric field, *J. Clean. Prod.* 335 (2022), 130375.

[164] B. Zhang, M. Zhang, L. Zhang, P.A. Bingham, M. Tanaka, W. Li, S. Kubuki, BiOBr/MoS₂ catalyst as heterogenous peroxymonosulfate activator toward organic pollutant removal: energy band alignment and mechanism insight, *J. Colloid Interface Sci.* 594 (2021) 635–649.

[165] J. Cui, Y. Zhang, Y. Zheng, Y. Pei, X. He, B. Xi, Catalytic degradation of carbamazepine by a novel granular visible-light-driven photocatalyst activating the peroxydisulfate system, *Chem. Eng. J.* 421 (2021), 127867.

[166] Y. Zeng, N. Guo, X. Xu, Y. Yu, Q. Wang, N. Wang, X. Han, H. Yu, Degradation of bisphenol a using peroxymonosulfate activated by WO₃@MoS₂/Ag hollow nanotubes photocatalyst, *Chemosphere* 227 (2019) 589–597.

[167] X. Zheng, X. Zhang, Y. Cai, S. Zhao, S. Wang, Efficient degradation of bisphenol A with MoS₂/BiVO₄ hetero-nanoflower as a heterogenous peroxymonosulfate activator under visible-light irradiation, *Chemosphere* 289 (2022), 133158.

[168] P. Chen, Y. Gou, J. Ni, Y. Liang, B. Yang, F. Jia, S. Song, Efficient Ofloxacin degradation with Co(II)-doped MoS₂ nano-flowers as PMS activator under visible-light irradiation, *Chem. Eng. J.* 401 (2020), 125978.

[169] P. Sarkar, D. Roy, B. Bera, S. De, S. Neogi, Efficient photocatalytic degradation of ciprofloxacin using novel dual Z-scheme gCN/CuFe2O4/MoS₂ mediated peroxymonosulphate activation, *Chem. Eng. J.* 430 (2022), 132834.

[170] C. Jin, J. Kang, Z. Li, M. Wang, Z. Wu, Y. Xie, Enhanced visible light photocatalytic degradation of tetracycline by MoS₂/Ag/g-C3N4 Z-scheme composites with peroxymonosulfate, *Appl. Surf. Sci.* 514 (2020), 146076.

[171] N. Ma, P. Xue, R. Li, L. Ma, K. Shi, Flower-like hybrid composite MoS₂/NH₂-MIL-101(Cr): A highly efficient photocatalyst for degrading indole under visible light, *J. Mater. Res.* 36 (2021) 4460–4474.

[172] D. Roy, S. Neogi, S. De, Mechanistic investigation of photocatalytic degradation of Bisphenol-A using MIL-88A(Fe)/MoS₂ Z-scheme heterojunction composite assisted peroxymonosulfate activation, *Chem. Eng. J.* 428 (2022), 131028.

[173] C. Dong, Z. Zheng, M.A.H. Badsha, J. He, I.M.C. Lo, Visible-light-driven peroxymonosulfate activation in photo-electrocatalytic system using hollow-structured Pt@CeO₂@MoS₂ photoanode for the degradation of pharmaceuticals and personal care products, *Environ. Int.* 154 (2021), 106572.

[174] L. Zeng, S. Li, X. Li, J. Li, S. Fan, X. Chen, Z. Yin, M. Tadé, S. Liu, Visible-light-driven sonophotocatalysis and peroxymonosulfate activation over 3D urchin-like MoS₂/C nanopartiles for accelerating levofloxacin elimination: Optimization and kinetic study, *Chem. Eng. J.* 378 (2019), 122039.

[175] Y. He, J. Qian, P. Wang, J. Wu, B. Lu, S. Tang, P. Gao, Acceleration of levofloxacin degradation by combination of multiple free radicals via MoS₂ anchored in manganese ferrite doped perovskite activated PMS under visible light, *Chem. Eng. J.* 431 (2022), 133933.

[176] L. Zhang, B. Zhang, L. Wang, R. Ge, W. Zhou, S. Kubuki, Ra Wu, J. Wang, Self-assembly of MoS₂ nanosheet adhered on Fe-MOF heterocrystals for peroxymonosulfate activation via interfacial interaction, *J. Colloid Interface Sci.* 608 (2022) 3098–3110.

[177] X. Chen, L. Liu, PMS activation over MoS₂/Co_{0.75}Mo₃S_{3.75} for RhB pollutant oxidation removal in fuel cell system, *J. Environ. Chem. Eng.* 10 (2022), 107449.

[178] J. Li, C. Hu, B. Liu, Z. Liu, Dual pathway reduction of Mo⁴⁺ and photogenerated electrons restore catalytic sites to enhance heterogeneous peroxymonosulfate activation system, *Chem. Eng. J.* 452 (2023), 139246.

[179] Y. Liu, X. Wang, Q. Sun, L. Chen, M. Yuan, Z. Sun, Y. Zhang, S. Xia, J. Zhao, Enhanced activation of peroxymonosulfate by a floating Cu⁰-MoS₂/C3N4 photocatalyst under visible-light assistance for tetracyclines degradation and Escherichia coli inactivation, *Chem. Eng. J.* 457 (2023), 141220.

[180] H. Zhang, Y. Zhou, Y. Zhang, Z. Hu, X. Gao, X. Wang, Z. Wu, Two-dimensional MoS₂ lattice constrained Cu(I) enables high activity and superior stability in visible-light-assisted peroxymonosulfate activation, *Sep. Purif. Technol.* 315 (2023), 123671.

[181] Z. Hu, B. Guo, H. Wu, F. Zhu, S. Komarneni, J. Ma, Activation of Na₂S₂O₈ by MIL-101(Fe)/MoS₂ composite for the degradation of tetracycline with visible light assistance, *Colloids Surf. A: Physicochem. Eng. Asp.* 654 (2022), 130202.

[182] C. Song, Z. Wang, Z. Yin, D. Xiao, D. Ma, Principles and applications of photothermal catalysis, *Chem. Catal.* (2021).

[183] Q. Gan, Y. Xiao, C. Li, H. Peng, T. Zhang, M. Ye, g-C₃N₄/MoS₂ based floating solar still for clean water production by thermal/light activation of persulfate, *Chemosphere* 280 (2021), 130618.

[184] Z. Yan, X. Chen, S. Bao, H. Chang, H. Liu, G. Fan, Q. Wang, X. Fu, F. Qu, H. Liang, Integration of in situ Fenton-like self-cleaning and photothermal membrane distillation for wastewater treatment via Co-MoS₂/CNT catalytic membrane, *Sep. Purif. Technol.* 303 (2022), 122207.

[185] K. Wang, C. Han, J. Li, J. Qiu, J. Sunarso, S. Liu, The mechanism of piezocatalysis: energy band theory or screening charge effect? *Angew. Chem. Int. Ed.* 61 (2022), e202110429.

[186] T. Wu, Q. Liang, L. Tang, J. Tang, J. Wang, B. Shao, S. Gong, Q. He, Y. Pan, Z. Liu, Construction of a novel S-scheme heterojunction piezoelectric photocatalyst V-BiO₃/FTCN and immobilization with floatability for tetracycline degradation, *J. Hazard. Mater.* 443 (2023), 130251.

[187] Y. Chen, S. Lan, M. Zhu, Construction of piezoelectric BaTiO₃/MoS₂ heterojunction for boosting piezo-activation of peroxymonosulfate, *Chin. Chem. Lett.* 32 (2021) 2052–2056.

[188] F. Peng, R. Yin, Y. Liao, X. Xie, J. Sun, D. Xia, C. He, Kinetics and mechanisms of enhanced degradation of ibuprofen by piezo-catalytic activation of persulfate, *Chem. Eng. J.* 392 (2020), 123818.

[189] S. Lan, Y. Chen, L. Zeng, H. Ji, W. Liu, M. Zhu, Piezo-activation of peroxymonosulfate for benzothiazole removal in water, *J. Hazard. Mater.* 393 (2020), 122448.

[190] G. Nie, L. Xiao, J. Bi, S. Wang, X. Duan, New insight to piezocatalytic peroxymonosulfate activation: The critical role of dissolved oxygen in mediating radical and nonradical pathways, *Appl. Catal. B: Environ.* 315 (2022), 121584.

[191] K.-S. Hong, H. Xu, H. Konishi, X. Li, Direct water splitting through vibrating piezoelectric microfibers in water, *J. Phys. Chem. Lett.* 1 (2010) 997–1002.

[192] J.M. Wu, W.E. Chang, Y.T. Chang, C.-K. Chang, Piezo-Catalytic Effect on the Enhancement of the Ultra-High Degradation Activity in the Dark by Single- and Few-Layers MoS₂ Nanoflowers, *Adv. Mater.* 28 (2016) 3718–3725.

[193] K. Kubota, Y. Pang, A. Miura, H. Ito, Redox reactions of small organic molecules using ball milling and piezoelectric materials, *Science* 366 (2019) 1500–1504.

[194] S. Li, X. Ning, P. Hao, Y. Cao, J. Xie, J. Hu, Z. Lu, A. Hao, Defect-rich MoS₂ piezocatalyst: efficient boosting piezocatalytic activation of PMS activity towards degradation organic pollutant, *Dyes Pigments* 206 (2022), 110678.

[195] H.-Y. Lin, K.T. Le, P.-H. Chen, J.M. Wu, Systematic investigation of the piezocatalysis–adsorption duality of polymorphic MoS₂ nanoflowers, *Appl. Catal. B: Environ.* 317 (2022), 121717.

[196] C. Yu, J. He, S. Lan, W. Guo, M. Zhu, Enhanced utilization efficiency of peroxymonosulfate via water vortex-driven piezo-activation for removing organic contaminants from water, *Environ. Sci. Ecotechnology* 10 (2022), 100165.

[197] M. Pan, S. Liu, J.W. Chew, Unlocking the high redox activity of MoS₂ on dual-doped graphene as a superior piezocatalyst, *Nano Energy* 68 (2020), 104366.

[198] W.T. Yein, Q. Wang, Y. Li, X. Wu, Piezoelectric potential induced the improved micro-pollutant dye degradation of Co doped MoS₂ ultrathin nanosheets in dark, *Catal. Commun.* 125 (2019) 61–65.

[199] S. Tu, Y. Guo, Y. Zhang, C. Hu, T. Zhang, T. Ma, H. Huang, Piezocatalysis and piezo-photocatalysis: catalysts classification and modification strategy, reaction mechanism, and practical application, *Adv. Funct. Mater.* 30 (2020) 2005158.

[200] M. Ran, H. Xu, Y. Bao, Y. Zhang, J. Zhang, M. Xing, Selective production of CO from organic pollutants by coupling piezocatalysis and advanced oxidation processes, *Angew. Chem. Int. Ed.* 62 (2023), e202303728.

[201] W. Liu, P. Fu, Y. Zhang, H. Xu, H. Wang, M. Xing, Efficient hydrogen production from wastewater remediation by piezoelectricity coupling advanced oxidation processes, *Proc. Natl. Acad. Sci.* 120 (2023), e2218813120.

[202] L. Xu, L. Liu, Piezo-photocatalytic fuel cell with atomic Fe@MoS₂ on CFC helical electrode has enhanced peroxymonosulfate activation, pollutant degradation and power generation, *Appl. Catal. B: Environ.* (2021), 120953.

[203] W. Zou, Z. Wan, C. Zhao, G. Zhang, X. Zhang, Q. Zhou, Impact of algal extracellular polymeric substances on the environmental fate and risk of molybdenum disulfide in aqueous media, *Water Res.* 205 (2021), 117708.

[204] S. Arefi-Oskouei, A. Khataee, O.K. Ucun, M. Kobya, T.Ö. Hancı, I. Arslan-Alaton, Toxicity evaluation of bulk and nanosheet MoS₂ catalysts using battery bioassays, *Chemosphere* 268 (2021), 128822.

[205] X. Wang, N.D. Mansukhani, L.M. Guiney, Z. Ji, C.H. Chang, M. Wang, Y.-P. Liao, T.-B. Song, B. Sun, R. Li, T. Xia, M.C. Hersam, A.E. Nel, Differences in the toxicological potential of 2D versus aggregated molybdenum disulfide in the lung, *Small* 11 (2015) 5079–5087.

[206] J. Fan, Y. Li, H.N. Nguyen, Y. Yao, D.F. Rodrigues, Toxicity of exfoliated-MoS₂ and annealed exfoliated-MoS₂ towards planktonic cells, biofilms, and mammalian cells in the presence of electron donor, *Environ. Sci.: Nano* 2 (2015) 370–379.

[207] W. Zou, Q. Zhou, X. Zhang, X. Hu, Dissolved oxygen and visible light irradiation drive the structural alterations and phytotoxicity mitigation of single-layer molybdenum disulfide, *Environ. Sci. Technol.* 53 (2019) 7759–7769.

[208] K. Tang, L. Wang, H. Geng, J. Qiu, H. Cao, X. Liu, Molybdenum disulfide (MoS₂) nanosheets vertically coated on titanium for disinfection in the dark, *Arab. J. Chem.* 13 (2020) 1612–1623.

[209] J. Hao, G. Song, T. Liu, X. Yi, K. Yang, L. Cheng, Z. Liu, In vivo long-term biodistribution, excretion, and toxicology of PEGylated transition-metal dichalcogenides MS₂ (M = Mo, W, Ti) nanosheets, *Adv. Sci.* 4 (2017) 1600160.

[210] R. Kurapati, L. Muzi, A.P.R. de Garibay, J. Russier, D. Voiry, I.A. Vacchi, M. Chhowalla, A. Bianco, Enzymatic biodegradability of pristine and functionalized transition metal dichalcogenide MoS₂ nanosheets, *Adv. Funct. Mater.* 27 (2017) 1605176.